PHOTONICS INSIGHTS

Optical quantum states based on hot atomic ensembles and their applications

Kai Zhang,[a] Shengshuai Liu,[a] Yingxuan Chen,[a] Xutong Wang,[a] and Jietai Jing[a,b,c,*]

[a]State Key Laboratory of Precision Spectroscopy, Joint Institute of Advanced Science and Technology, School of Physics and Electronic Science, East China Normal University, Shanghai, China

[b]CAS Center for Excellence in Ultra-intense Laser Science, Shanghai, China

[c]Collaborative Innovation Center of Extreme Optics, Shanxi University, Taiyuan, China

Abstract. The four-wave mixing process in atomic ensembles has many important applications in quantum information. We review recent progress on the generation of optical quantum states from the four-wave mixing process in hot atomic ensembles, including the production of two-beam, multi-beam, and multiplexed quantum correlated or entangled states. We also review the applications of these optical quantum states in implementing quantum information protocols, constructing SU(1,1) quantum interferometers, and realizing quantum plasmonic sensing. These applications indicate that the four-wave mixing process in hot atomic ensembles is a promising platform for quantum information processing, especially for implementing all-optical quantum information protocols, constructing SU(1,1) interferometers, and realizing quantum sensing.

Keywords: optical quantum states; four-wave mixing; atomic ensemble; quantum information protocol.

Received May 1, 2022; revised manuscript received Sep. 23, 2022; accepted Oct. 17, 2022; published online Dec. 24, 2022.

[DOI: 10.3788/PI.2022.R06]

1 Introduction

Optical quantum states, indispensable carriers of optical quantum information, are important non-classical resources for quantum information processing (QIP). There are two kinds of quantum systems for generating optical quantum states, i.e., discrete variable (DV)[1] and continuous variable (CV)[2] systems. The DV system means that the physical quantity for encoding quantum information has a discrete energy spectrum, including a single photon[3–5], quantum bit[6,7], and so on. The CV system refers to the physical quantity for encoding quantum information with a continuous energy spectrum, including the optical mode[8–10], microwave mode[11], and so on. DV and CV quantum systems are two platforms of equal importance for QIP. They have their own advantages. In the DV system, to enhance its scale, increasing the number of entangled photons is a direct way[12–14]. Due to the probabilistic generation of entangled photons, the detection rate of multi-photon entanglement will dramatically decrease with the increase in the number of entangled photons. One solution for solving this issue is increasing the dimensionality of the state, i.e., exploiting the high-dimensional entanglement to increase the scale without significantly reducing the detection rate[15–20]. Photons can be entangled not only in one degree of freedom (DOF), but also in multiple DOFs, producing so-called hyperentanglement. Therefore, another solution is increasing the number of DOFs with which the photons are entangled[21–23]. This can increase the number of qubits, which increases the scale of the system without markedly reducing the detection rate. Because coincidence measurement in a DV system can rule out the unwanted vacuum or background contributions, the introduced losses from the environment and optical devices will not reduce the fidelity of the entangled state. Therefore, the DV system is not very sensitive to losses, and its transmission distance can be increased relatively easily[24,25]. For example, DV-entanglement-based quantum key distribution between two ground stations 1120 km apart has recently been implemented[26]. In the CV system, the entangled optical modes are generated deterministically, and therefore the CV system is not bothered by the detection rate. Consequently, the number of entangled modes can be scaled relatively easily. For example, the number of entangled modes to date has reached the level of 10,000[27,28]. The scale of the CV system can be enhanced by increasing not only the number of entangled modes[27,28] but also the number of multiplexed

*Address all correspondence to Jietai Jing, jtjing@phy.ecnu.edu.cn

channels[29]. However, the CV system is very sensitive to the noise introduced by losses, especially propagation losses, which will introduce unwanted vacuum noise and deteriorate the quality of entanglement. This will finally limit its transmission distance in quantum communication. A recent trend is to combine CV and DV systems to develop a hybrid quantum system by exploiting their respective advantages[30]. Both have made a series of important progress in generating optical quantum states. In this review, we focus on the CV system.

In the CV system, the squeezed state is one of the most crucial optical quantum states. In the early stage, the squeezed state was generated by the group of Slusher in atomic vapor inside an optical cavity[31], the group of Kimble in nonlinear crystal[32], and the group of Walls in optical fiber[33]. However, the squeezing degrees of these squeezed states are relatively low. Therefore, improving the squeezing degree of the squeezed state has become an important research topic for many groups. With the development of experimental technology, the group of Schnabel achieved a 15 dB squeezed state[34]. In addition, the group of Peng successfully achieved the squeezed state with 13.2 dB squeezing[35]. Squeezed states are widely used in quantum metrology due to their noise reductions. One example is that the squeezed state can significantly improve the detection sensitivity of the Laser Interferometric Gravitational Wave Observatory (LIGO)[36–38]. In addition, the squeezed state can also be used for laser beam positioning[39,40], rotation angle measurement[41], and time transfer[42]. Therefore, it is important to realize the squeezed state with a high squeezing degree in various systems.

In the CV system, the entangled state is another important type of optical quantum state. In 1992, the Einstein–Podolsky–Rosen (EPR) entangled state[43] was realized by the group of Kimble in the CV regime[44] based on the theoretical proposal of Reid[45]. In 2000, Duan *et al.* and Simon proposed the entanglement criterion for the CV system[46,47]. After that, the EPR entangled state began to be widely generated experimentally[8,48]. As quantum information has developed, generating multimode entangled states[49,50] has attracted the attention of many groups. In 2003, by using a linear optical beam splitter (BS), the group of Peng realized the tripartite entangled state[9]. After that, the group of Furusawa also realized a tripartite entangled state[51–53]. Then, the group of Peng successfully realized quadripartite[54] and eight-partite[55] cluster states. The group of Nussenzveig and Martinelli realized bipartite[56,57] and hexapartite[58,59] entangled states in optical parametric oscillators (OPOs). In 2013, the group of Furusawa successfully realized the ultra-large-scale entangled state of more than 10,000 modes by introducing time as a new entanglement DOF[60]. This experiment provides a new method for generating ultra-large-scale entangled states. Then, the group of Furusawa[27] and Andersen[28] independently realized the ultra-large-scale two-dimensional cluster state through two-dimensional time-multiplexing technology. In 2012, Armstrong *et al.* realized eight-spatial-mode entangled states[61]. In addition, frequency multiplexing technology is also used to generate large-scale entangled states. In 2014, the group of Pfister successfully realized a 60-mode entangled state through frequency comb technology[62]. Yang *et al.* realized an entangled state with 40 modes on a chip by frequency comb technology[63]. The group of Fabre and Treps realized large-scale quantum networks[64] and structurally reconfigurable multimode entangled states[65] through wavelength multiplexing technology. The entangled states are indispensable resources for QIP because of their nonlocal properties. For example, entangled states can be utilized to implement quantum teleportation[66–69], quantum dense coding (QDC)[70], entanglement swapping[71], and so on.

There are many different ways to generate squeezed and entangled states, most of which rely on nonlinear processes, for example, $\chi^{(2)}$ and $\chi^{(3)}$ nonlinear processes with a nonlinear crystal or an atomic vapor cell. The conventional approach to generate CV quantum states is utilizing OPOs[56] and optical parametric amplifiers (OPAs)[48] from a nonlinear crystal. Compared with them, quantum light sources from atomic ensembles[72] have many advantages. First, the wavelength and bandwidth generated by this system are naturally matched with the atomic transition, and can be used in quantum memory. Second, the atomic coherence property can enhance the nonlinear interaction strength of the system, resulting in quantum states of strong squeezing and entanglement without using an optical cavity. Therefore, this system avoids the spatial mode limitation of the light field caused by the optical cavity and ensures the multi-spatial-mode nature of the system. Compared with the cold atomic ensemble system[18,22], which needs laser cooling and trapping technology to cool the atoms, the hot atomic ensemble system has many applications with its simplicity, stability, and compactness. Because of these advantages, the four-wave mixing (FWM) process in hot atomic ensembles based on double-Λ energy level structure has been proved to be a promising way to generate CV optical quantum states[72–113]. In 2007, the group of Lett generated 3.5 dB squeezing based on the FWM process[72]. In 2008, their group realized entangled images based on the FWM process[93]. This experiment proves that the entangled beams generated by the FWM process have a spatial multimode property[86,88]. In 2009, their group realized the tunable delay of EPR entanglement based on the FWM process[95]. In addition, their group found the slow[96] and fast[97–99] light effects in this FWM process. Such a system can also be used to construct noiseless optical amplifiers[100]. Due to these properties, optical quantum states based on the FWM process can be widely used in QIP.

In this review, we focus on recent progress on the production of optical quantum states from the FWM process in hot atomic ensembles and their applications. Section 2 reviews the generation of optical quantum states from FWM processes in hot atomic ensembles. The applications of optical quantum states in implementing quantum information protocols (quantum metrology) are reviewed in Section 3 (Section 4). Section 5 concludes this review.

2 Optical Quantum States Based on Four-Wave Mixing Process in Hot Atomic Ensembles

Because of the advantages of the FWM process described above, it has been used to generate different types of optical quantum states[101–113]. In this section, optical quantum states based on the FWM process are introduced. The generation of two-beam quantum correlation is described in Subsection 2.1. The quantum correlations from phase-sensitive amplifiers (PSAs) are described in Subsection 2.2. The generation of multi-beam quantum correlations is introduced in Subsection 2.3. To enhance the entanglement capacity of the entangled source, orbital angular momentum (OAM) multiplexed entanglement is introduced in Subsection 2.4.

2.1 Two-Beam Quantum Correlation

Quantum squeezing is an important non-classical effect related to the "uncertainty principle" in quantum physics. Therefore, it has important scientific value for the basic research of quantum physics. At the same time, quantum squeezing can greatly reduce the quantum noise of the system[114], so as to significantly improve the signal-to-noise ratio (SNR) and sensitivity of the system. As a result, it has important value in quantum metrology. For example, quantum squeezing can be used to improve the sensitivity of LIGO[36–38], atomic magnetometers[115], optical-mechanical magnetometers[116], and plasmonic sensors[117–122].

The FWM process in hot atomic ensembles has been demonstrated as an effective method to produce quantum squeezing. The quantum squeezed beams generated from this system have found wide applications in the fields of quantum imaging[85–94,123], quantum entanglement delay[95], and nonlinear interferometers[124–129]. In this subsection, the generation and characterization of quantum correlated twin beams from the FWM process are introduced.

2.1.1 Generation of two-beam quantum correlation

In 1985, the first experimental generation of squeezed light with the FWM process was based on sodium vapor[31]. Since then, the FWM process has been used to generate squeezed light under various conditions. Due to the limitation of spontaneous emission noise, the squeezing level is difficult to improve. In 2007, for the first time, McCormick *et al.* improved the intensity difference squeezing (IDS) in hot rubidium vapor to 3.5 dB[72]. Their scheme uses ground-state coherence-based resonant nonlinearity in a three-level system.

As shown in Fig. 1(a), this FWM process starts with two laser beams. One strong beam—1 GHz blue detuned from the ^{85}Rb D_1 line transition—is used as the pump beam. The other beam serves as the probe beam. The vertically polarized pump beam and horizontally polarized probe beam are focused into a ^{85}Rb vapor cell with a temperature of 125°C. The pump and probe beams intersect at a small angle of about 0.75°, resulting in the production of a conjugate beam. When scanning the frequency of the probe beam, due to the FWM gain, two intensity gain peaks are observed, as shown in Fig. 1(c). Then McCormick *et al.* fixed the probe beam 3.03 GHz red tuned from the pump beam. Under these experimental conditions, the probe beam has an intensity gain of four.

To verify the quantum correlation, the amplified probe beam and newly generated conjugate beam are detected by a balanced photodetector whose output is measured by a spectrum analyzer. To calibrate the standard quantum limit (SQL), or shot noise limit (SNL), of this system, a portion of the probe beam, with power equal to the sum of the probe and conjugate beams, is picked up before the Rb cell and equally split by a BS, and the beams from the output ports of the BS are detected by the photodetector. For a total optical power (probe plus conjugate) of 180 μW, the relative intensity noise between the probe and conjugate beams is 3.5 dB below the SQL, as shown in Fig. 1(d). Their results show that this system holds promise as a considerable source of squeezed light.

By extending the above work on the D_1 line of ^{85}Rb, Pooser *et al.* further demonstrated that quantum correlated beams can also be generated from the FWM process in both the D_1 (795 nm) and D_2 (780 nm) lines of ^{85}Rb and ^{87}Rb and characterized the degree of IDS for each of the four systems. The hyperfine levels of ^{85}Rb and ^{87}Rb are shown in Figs. 2(a) and 2(b), respectively. As shown in Figs. 2(c) and 2(d), they observed quantum correlations generated by all four systems. Despite the similar double-Λ configuration, different level structures of the four systems result in different degrees of IDS. In particular, the optimal squeezing of −8.0 dB and −7.8 dB of D_1 lines in ^{85}Rb and ^{87}Rb is observed. Their results indicate that it is possible to use systems with similar double-Λ configuration to generate squeezed light.

In addition to rubidium vapor, IDS can also be generated from the FWM process in other alkali vapors[74–76]. In 2017, Swaim *et al.* demonstrated the generation of IDS from the FWM process in potassium vapor, which is a strongly absorbing medium for one of the generated twin beams[74]. They showed that quantum correlations can still be generated, albeit with a significantly different absorption between the generated twin beams. Figure 3(a) shows the double-Λ configuration in the D_1 line of ^{39}K, in which one of the generated twin beams is

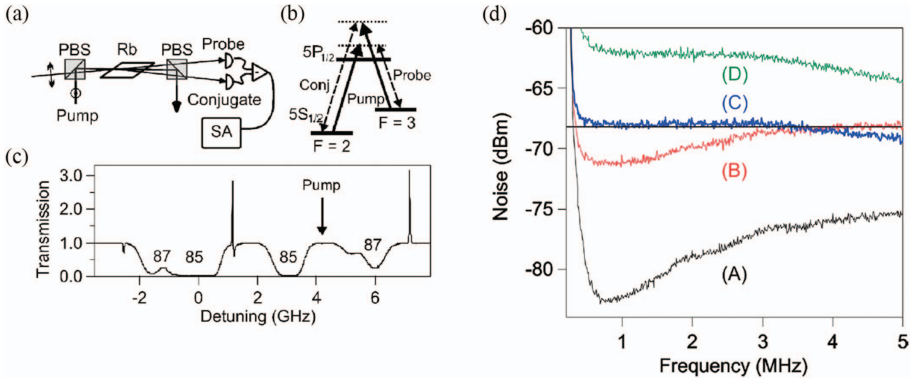

Fig. 1 Strong IDS from the FWM process in rubidium vapor. (a) Experimental schematic. PBS, polarizing beam splitter; SA, spectrum analyzer. (b) Double-Λ energy level diagram. (c) Transmission for the probe beam as a function of the detuning from the ^{85}Rb D_1 line transition. The arrow indicates the pump detuning. (d) Experimentally measured noise power as a function of spectrum analyzer frequency with (A)–(D) electronic noise, squeezed noise between the probe and conjugate, SNL, and probe noise, respectively. Adapted from [72].

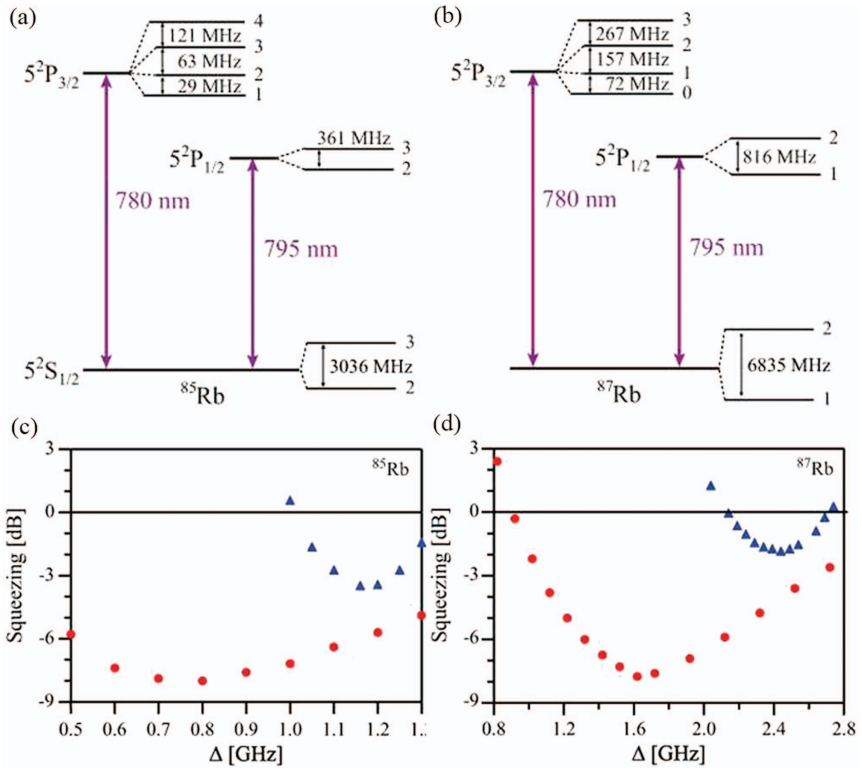

Fig. 2 (a), (b) Hyperfine levels in D_1 and D_2 line transitions of ^{85}Rb (a) and ^{87}Rb (b). (c), (d) Experimentally measured squeezing levels in the D_1 (red circles) and D_2 (blue triangles) lines of ^{85}Rb (c) and ^{87}Rb (d) versus pump detuning. Adapted from [73].

located at the center of a Doppler-broadened absorption profile. Therefore, the absorption for the generated twin beams is significantly different. With a transmission of 17% for the probe beam and detection efficiency of 0.5, they observed an IDS of −1.1 dB, as shown in Fig. 3(b). Their results showed that IDS can be generated even if the losses between generated twin beams are significantly different. In addition, two-beam quantum correlation has been generated in hot cesium vapor[75], and an IDS of 6.5 dB is obtained[76].

2.1.2 Enhancement of quantum correlation

The degree of quantum squeezing directly determines the improvement of the performance of the system. The enhancement of quantum squeezing is important for quantum metrology[34,35,78]. Based on the abovementioned FWM system of ^{85}Rb D_2 line transition, Zhang *et al.* demonstrated the enhancement of IDS through energy-level modulations[79]. An initial IDS of −3.6 dB can be enhanced to −5.0 and −6.1 dB when using two different dressing fields. Moreover, the IDS can reach −9 dB when both dressing fields exist.

The experimental setup is shown in Fig. 4(a), where E_1 and E_2 are the pump beam and probe beam, respectively. Two approachs are used to dress the double-Λ system based on ^{85}Rb D_2 line (780 nm) transition. One is through the E_3 field between levels $|2\rangle$ and $|3\rangle$, and another is through the E_4 field between levels $|0\rangle$ and $|4\rangle$, as shown in Fig. 4(b). When the initial pump E_1 is added with E_4 (795 nm) and E_3 (776 nm), they construct two electromagnetically induced transparency windows and apparently change the original FWM process. Compared with the original FWM case (with −3.6 dB IDS), the degrees of IDS for E_3- and E_4-dressed FWM processes can be enhanced to −5.0 and −6.1 dB, respectively. In particular, with E_3 and E_4 both on simultaneously, the degree of IDS increases to −9.0 dB, as shown in Figs. 4(d) and 4(e). The increase of IDS is due to the increase of the two-beam-dressed FWM gain with coexisting and constructive interference FWM, six-wave mixing (SWM), and eight-wave mixing (EWM) processes in this system, as shown in Figs. 4(c1)–4(c3). In addition to this scheme, it is possible to enhance the quantum correlation using other schemes, which will be discussed in Subsections 2.2.2, 2.3.1, and 2.3.2.

2.1.3 Multi-spatial-mode nature for quantum imaging

Spatially multimode light can be used to probe or carry spatial information, or for bright illumination and quatum imaging applications[85,89–92]. Due to the absence of an optical cavity, there is no mode selection in the FWM process, and thus the generated twin beams are spatially multimode.

In 2008, Boyer *et al.* experimentally verified this characteristic with three different methods[86]. First, the multimode nature of the FWM system can be verified by the fact that quantum correlation can be generated for different angles θ and φ of the probe beam, as shown in Figs. 5(a) and 5(b). It can be found that squeezing exists in the angular bandwidth of $\Delta\theta \approx 8$ mrad. Second, they attenuated (Q_a) or clipped (Q_c) the output probe with only a BS or a centered iris. As expected, the behavior of the Mandel parameter, defined as $Q = (\langle\Delta\hat{N}^2\rangle/\langle\hat{N}\rangle) - 1$, where $\hat{N}$ is the photon number operator, with transmission different for these two methods, as shown on the left of Fig. 5(c). This indicates that the various transverse areas are independent in their intensity noise. Third, the multimode nature can be

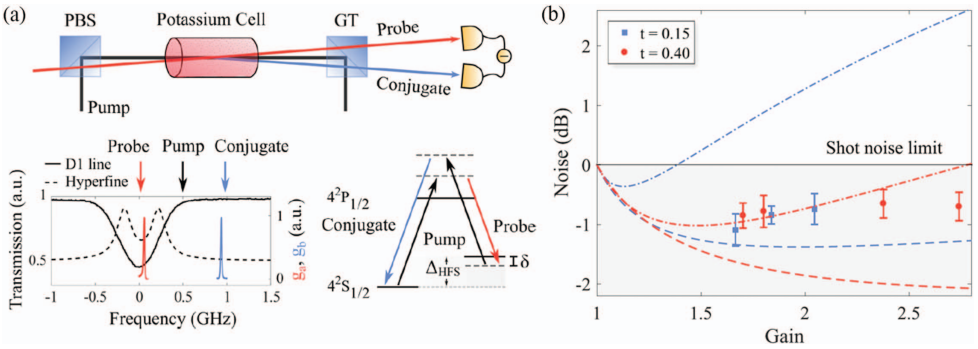

Fig. 3 IDS from the FWM process in potassium vapor, which is a strongly absorbing medium. (a) Experimental setup and double-Λ energy configuration. (b) Experimentally measured IDS with different intensity gain and probe transmissions (t). Adapted from [74].

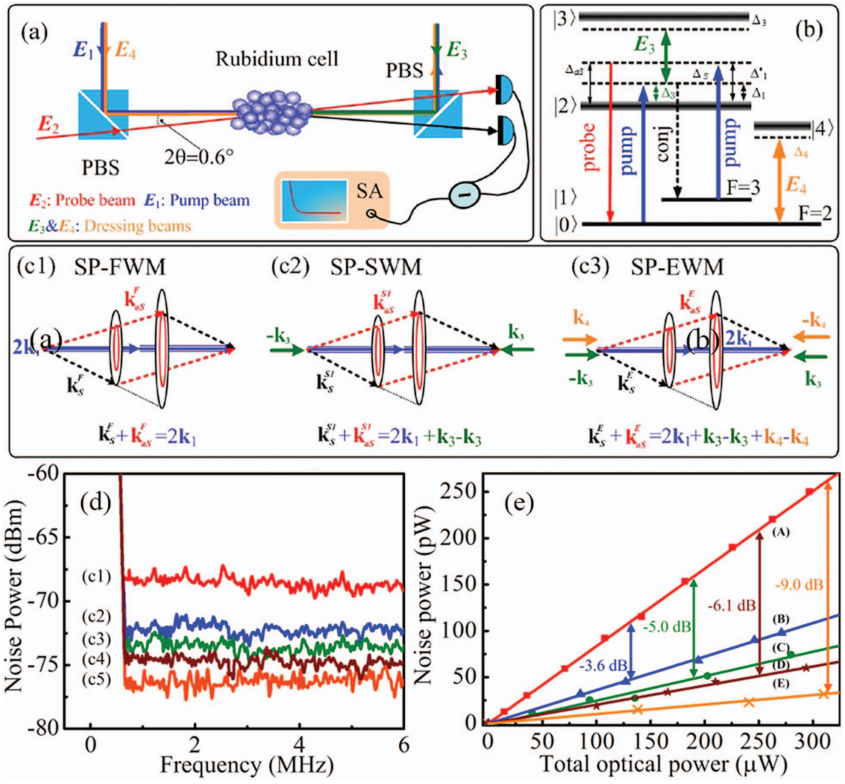

Fig. 4 (a) Experimental details. (b) Energy level diagram of ^{85}Rb D_2 line transition. (c) Phase-matching conditions for the spontaneous FWM (c1), spontaneous SWM (c2), and spontaneous EWM (c3) processes. (d) Noise power as a function of spectrum analyzer frequency for SQL (c1), FWM (c2), E_3-dressed FWM (c3), E_4-dressed FWM (c4), and E_3- and E_4-dressed FWM (c5). (e) Noise power versus total optical power for SQL (A), FWM (B), E_3-dressed FWM (C), E_4-dressed FWM (D), and E_3- and E_4-dressed FWM (E). Adapted from [79].

verified by symmetrically (Q_{cS}) or antisymmetrically (Q_{cA}) clipping the probe and conjugate regarding the pump, as shown on the right of Fig. 5(c). In the second (Q_c) and third (Q_{cS}) methods, the Mandel parameter is not constant and tends to zero when the detection area is small. Such a phenomenon indicates that there exists a coherence area, under which the light field can be seen as a single mode. These results show that the FWM process can generate spatially multimode quantum correlated twin beams.

A natural question is how to increase the mode number generated from the FWM process. This is in fact related to the size of the coherence area. To control the size of the coherence area, Holtfrerich *et al.* studied how the size and spatial profile of the pump beam affect the coherence area of the twin beams generated from the FWM process[87], as shown in Fig. 6(a). They found that the size of the coherence area can be reduced by increasing the size of the pump, and in this way, the mode number of the generated twin beams can be increased. They

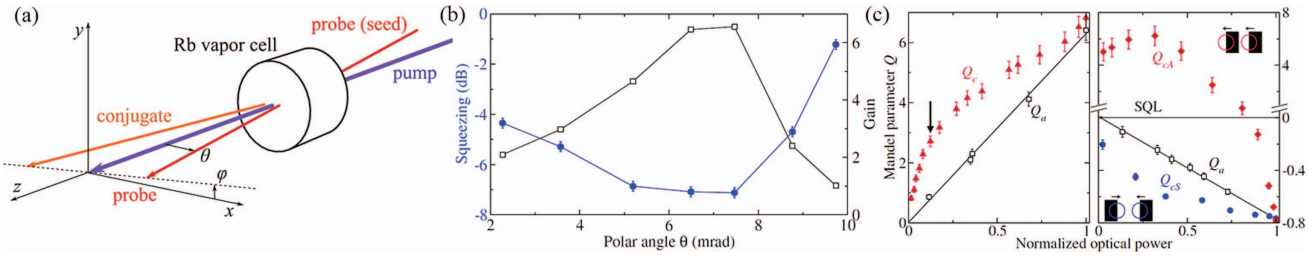

Fig. 5 (a) Setup geometry. (b) Gain and IDS as a function of the angle θ. (c) Mandel parameter for the probe only (left) and for the intensity difference (right) versus the transmission. Adapted from [86].

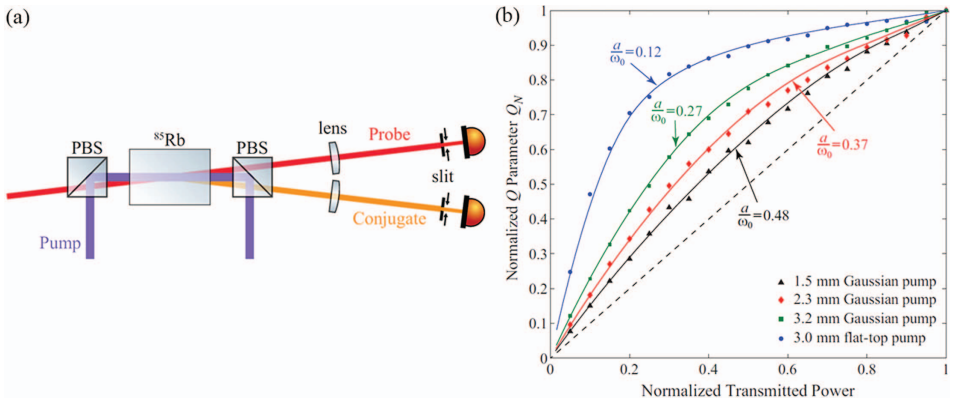

Fig. 6 (a) Experimental setup. (b) Experimental results of the effect of the size and spatial profile of the pump beam on the size of the coherence area and the number of spatial modes. Adapted from [87].

also found that a flattop pump beam of the same size as a Gaussian pump beam can reduce the coherence area by a factor of more than two and therefore increase the number of spatial modes by a factor of more than four, as shown in Fig. 6(b).

The multi-spatial-mode nature of FWM is reflected not only in IDS but also in quadrature squeezing. Embrey *et al.* showed that the quantum correlated twin beams from the FWM process are multi-spatial-mode squeezed and exhibit localized quadrature squeezing using a bichromatic local oscillator (BLO) with two different frequency components[88].

To generate the BLO, the probe and conjugate beams from the FWM process are combined by a BS. Then the BLO is used to measure the quadrature squeezing noise of the signal, as shown in Fig. 7(b). By controlling the relative phase between the signal and BLO fields, the signal quadrature can be obtained. The seed beam is shaped with a slit mask to control the width of the BLO as shown in Fig. 7(a). The impact of the width of the BLO on the squeezing level is shown in Fig. 7(c). It can be found that the local squeezing tends to zero when the width is equal to 0.18 mm, i.e., coherence length. The squeezing level versus the position of the BLO in two directions is shown in Figs. 7(d)–7(i). When the gain is reduced from four (green squares) to two (blue circles), the squeezing can be found for a smaller width of BLO and over a larger range of positions. From Figs. 7(d) and 7(g), the size of the squeezing region l is equal to 3.1 mm in both $x = y$ and $x = -y$ directions. Taking into account the coherence length of w_0, the total number of squeezed modes $l^2/4w_0^2 = 75$ is obtained, showing the multi-spatial-mode nature of quantum correlated beams from the FWM process.

Based on the multi-spatial-mode nature of the FWM process, Boyer *et al.* realized entangled images[93]. The FWM process, which is a spatially multimode amplifier, is utilized to generate twin images, as shown in Fig. 8(a). The images can behave as bright fields exhibiting position-dependent IDS, or vacuum fields that exhibiting quantum entanglement for a number of spatial modes. The vacuum twin beams can be described by the quadrature operators: $\hat{X}_a$ and $\hat{Y}_a$ for the probe field and $\hat{X}_b$ and $\hat{Y}_b$ for the conjugate field. The joint quadrature operators are defined by $\hat{X}_- = (\hat{X}_a - \hat{X}_b)/\sqrt{2}$ and $\hat{Y}_+ = (\hat{Y}_a + \hat{Y}_b)/\sqrt{2}$, which combines the quadrature operators of the twin fields. When the intensity gain of the FWM process is larger than one, the fluctuations $\langle \Delta\hat{X}_-^2 \rangle$ and $\langle \Delta\hat{Y}_+^2 \rangle$ are smaller than the SQL, which is defined by the variance of these operators for vacuum states, i.e., they are squeezed. For measuring the fluctuations of the quadrature operators, two homodyne detectors (HDs) are used. The local oscillators, mode-matched to the detected mode pair, of the HDs are generated by setting a new FWM process in the same vapor cell. For T-shaped modes, the measured fluctuation is −3.6 dB below SQL, which verifies the entanglement between two images, as shown in Fig. 8(b). These three works confirm the potential of the FWM process for practical quantum imaging.

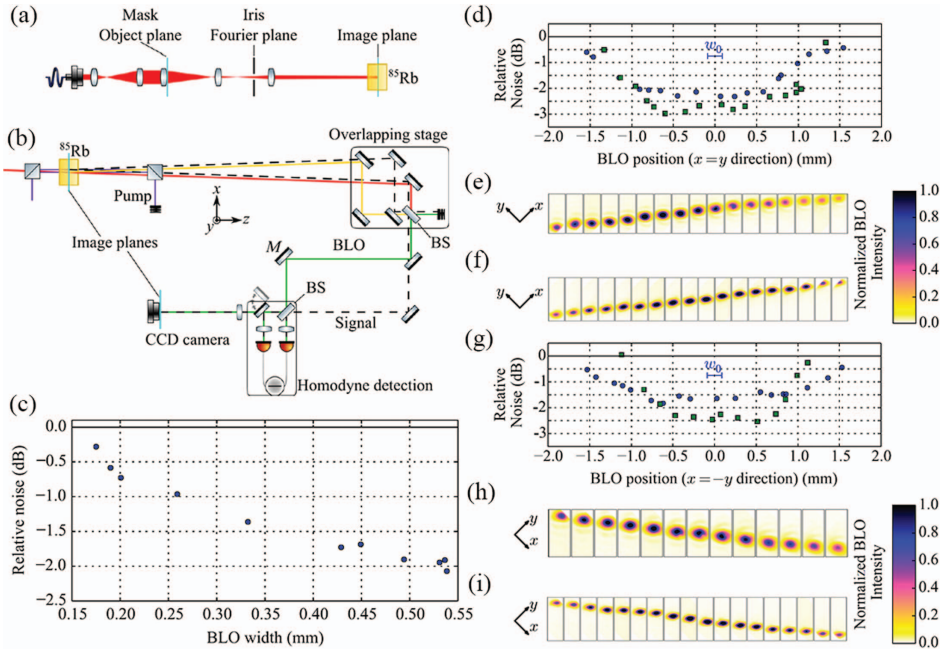

Fig. 7 (a) The masked and filtered probe beam is seeded into the center of the vapor cell. (b) Generation and detection of the squeezed vacuum beam with BLO. (c) Squeezing versus the width of the BLO. (d) Squeezing versus BLO position when it is translated along the $x = y$ direction. The green squares and blue circles show the squeezing in a gain of four and two, respectively. (e), (f) Images of BLO corresponding to the green and blue data, respectively. (g)–(i) Similar to (d)–(f) as the BLO position translates along the $x = -y$ direction. Adapted from [88].

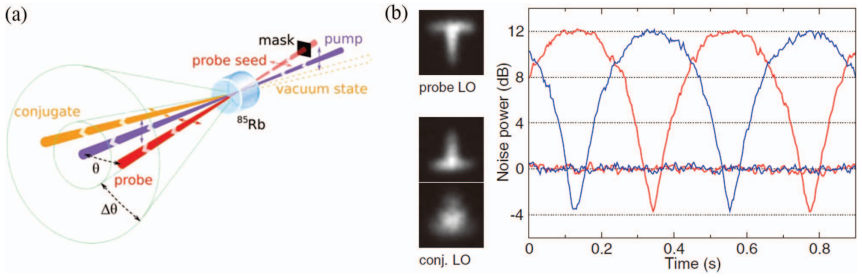

Fig. 8 Entangled images from the FWM process. (a) Geometry of the multi-spatial-mode property of the FWM process. (b) Measured quadrature squeezing for T-shaped modes. Adapted from [93].

2.1.4 Slow-light and fast-light effects

Atomic ensembles can control the dispersive properties that determine the group velocity of light. Under certain conditions, the FWM process has slow-light or fast-light effects.

In 2009, Marino *et al.* realized the tunable delay of entanglement based on the FWM process in hot atomic ensembles[95]. The quantum correlations of the entangled beams can still be preserved despite a significantly large delay between entangled beams. This experiment uses two sets of FWM processes in two rubidium cells, as shown in Fig. 9(a). The first cell is used to generate entangled probe and conjugate beams, while the second cell acts as a slow-light medium and delays the probe beam. This delay can be described by the time shift of the cross-correlation function between the generated twin beams relative to the reference cross-correlation function. Through changing the temperature of the second cell and pump power of the second FWM process, this delay can be controlled. As shown in Fig. 9(b), EPR entanglement, quantified by the EPR criterion, disappears at a delay as large as 27 ns. Based on the spatially multimode property of the FWM process, Marino *et al.* also demonstrated the delay of entangled images. Their results show that it is possible to use the FWM process to store quantum states.

In addition to being used as a slow-light medium[95,96], the hot rubidium atomic ensemble can also serve as a fast-light medium. In 2012, Glasser *et al.* realized the stimulated generation of superluminal pulses via the FWM process, in which both seeded and generated optical pulses possess negative group velocities[97]. The FWM process is used to generate strong

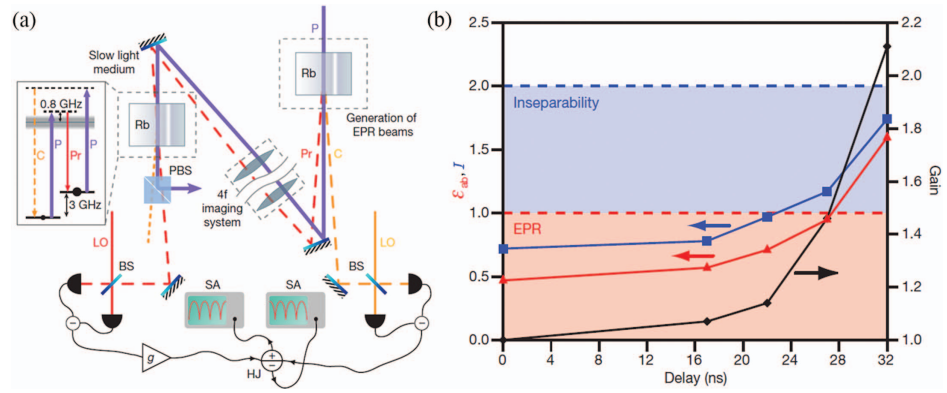

Fig. 9 (a) The probe (Pr) and the conjugate (C) beams are generated from the FWM process in the first rubidium cell. The second cell delays the probe beam. (b) EPR entanglement disappears for a delay of about 27 ns. Adapted from [95].

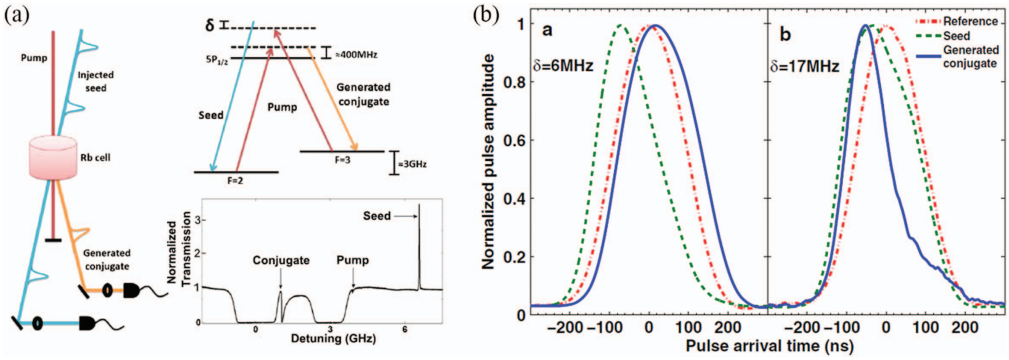

Fig. 10 (a) Experimental setup and double-Λ configuration. (b) Normalized amplitude of the amplified seeded pulse and the newly generated conjugate pulse for two different seeded pulse detunings. Adapted from [97].

anomalous dispersion, as shown in Fig. 10(a). The gain line experienced by the seeded pulse leads to negative dispersion at the gain line edges. In addition, the asymmetric gain and absorption line profile results in a broad region of negative dispersion for the newly generated conjugate pulse. Therefore, the amplified seeded pulse can have negative group velocity, and the newly generated conjugate pulse can propagate faster, as shown in Fig. 10(b). Also, the group velocities can be controlled by detuning the seeded pulse or changing the seeded power, which enables the tunable advancement or delay of the pulse.

Based on the above studies, Vogl *et al.* demonstrated the advancement of intensity-difference squeezed light according to the fast-light effect of the FWM process[98]. As shown in Fig. 11(a), this experiment is based on two FWM processes

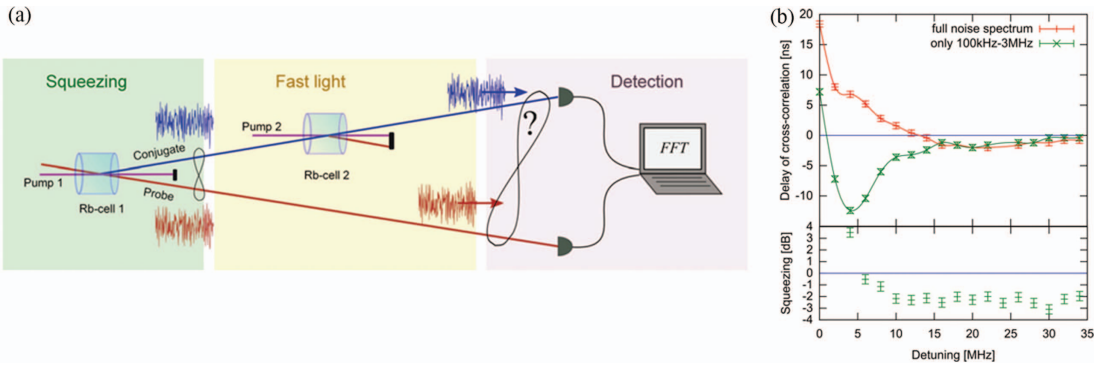

Fig. 11 Advancement of bright intensity-difference squeezed light. (a) Experimental setup. (b) Measured delay of the cross-correlation function versus the detuning of the pump beam of the second FWM process and the observed IDS. Adapted from [98].

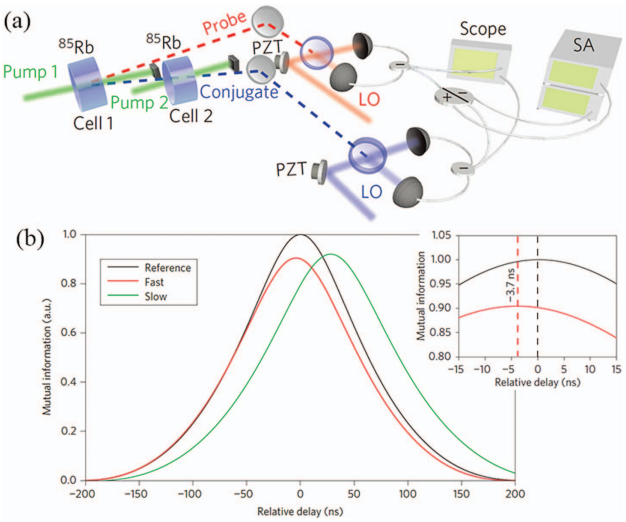

Fig. 12 Quantum mutual information of advanced and delayed entangled states. (a) Experimental setup. (b) Quantum mutual information versus relative delay for fast (red curve) and slow (green curve) light. Adapted from [99].

in rubidium cells. The first FWM process generates bright intensity-difference squeezed light, while the second serves as a fast-light process and enables controllable advancement of a conjugate beam while keeping the IDS present. The experimentally measured delay of the cross-correlation function versus detuning of the pump beam of the second FWM process relative to the pump beam of the first process is shown in Fig. 11(b). The results show that it is possible to advance one of the generated twin beams and still maintain quantum correlation based on the fast-light effect of the FWM process.

Furthermore, Clark *et al.* showed that quantum mutual information can also be advanced through the FWM process based on the fast-light effect[99]. As shown in Fig. 12(a), they used the first FWM process to generate entangled probe and conjugate beams and the second process as a fast-light or slow-light medium by detuning the pump. In this way, they investigated how dispersion related to FWM gain affects quantum correlation. The quantum mutual information between the generated twin beams versus relative delay for fast (red curve) and slow (green curve) light is shown in Fig. 12(b). They found that when one of the entangled beams passes through the fast-light medium, the peak of the quantum mutual information can be advanced, but the arrival of the leading edge cannot be advanced due to the noise introduced by FWM gain, which degrades quantum correlation. In addition, the leading and trailing edges of the mutual information can both be delayed when the second FWM process serves as a slow-light medium. Their results shed light on the function of quantum noise in affecting quantum information transport.

2.2 Quantum Correlation from Phase-Sensitive Amplifiers

The above reviewed works are on phase-insensitive amplifiers (PIAs) based on the FWM process in hot atomic ensembles. Studies of PSAs based on the FWM process are also of importance due to advantages in quantum manipulation and enhancement in quantum correlation.

2.2.1 Noiseless optical amplifier and single-beam squeezing from phase-sensitive amplifiers

Using the PSA based on FWM in hot Rb vapor, Corzo *et al.* found that the noise figure (NF) of the PSA is always better than the PIA with the same gain[100]. In addition, they observe that the amplifier supports hundreds of spatial modes, making it possible to noiselessly amplify complicated two-dimensional images for the first time.

The PSA scheme, inverting the previous double-Λ configuration, is pumped by two strong beams (ν_1 and ν_2) having frequencies and directions of the previous probe and conjugate beams and seeded with a weak beam (ν_p) having the frequency and direction of the previous pump beam as shown in Fig. 13(a). The beams out of two acousto-optic modulators (AOMs) seeding two tapered amplifiers are used to generate strong pump beams. The performance of the amplifier can be characterized by the NF, which is defined as the ratio between the SNR of input and output signals. Using a gain of 3.9, the NFs of an ideal PIA and PSA are 1.6 and 0.93, respectively. Thus, the PSA is close to the quantum limit and outperforms an ideal PIA. The multi-spatial-mode character of this PSA is verified by

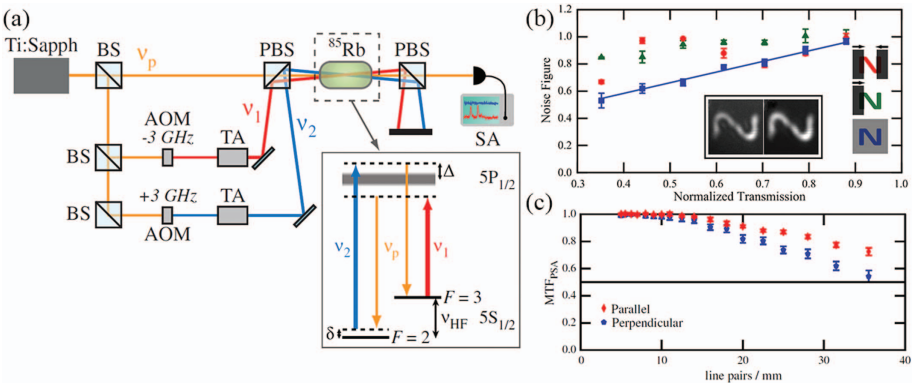

Fig. 13 (a) Experimental details for the FWM-based PSA. TA, tapered amplifier. (b) NF results versus spatially varying losses when cutting by a slit (red circles), cutting by a razor blade (green triangles), or attenuating by a neutral density filter (blue squares). (c) MTF of the PSA (MTF_{PSA}) measured along two directions. Adapted from [100].

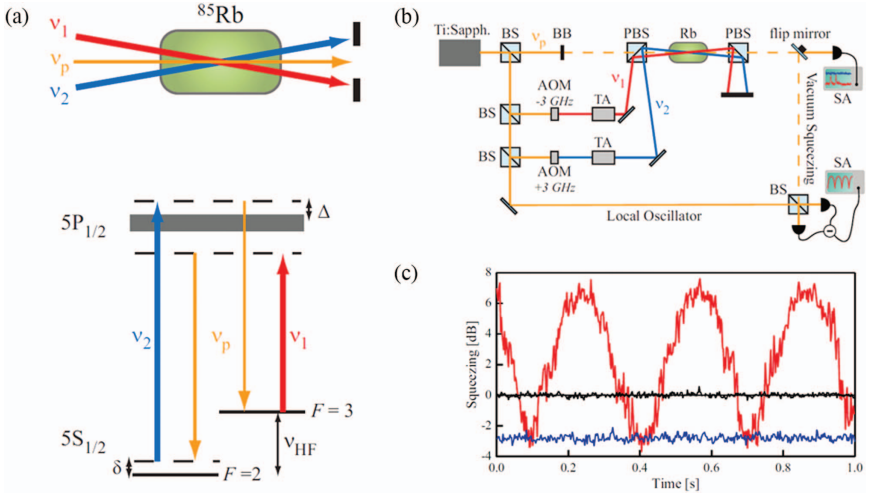

Fig. 14 (a) The top panel shows the schematic of the PSA. The lower panel shows the double-Λ configuration in the D_1 transition of ^{85}Rb. Here ν_1 and ν_2 represent the pump beams, and ν_p represents the probe beam. (b) Experimental setup. (c) Quadrature squeezing measured by HD. Adapted from [101].

examining the influence of spatially varying losses on the NF, as shown in Fig. 13(b). The different behaviors of these three methods exhibit the multimode nature of the PSA. To study the spatial resolution, they also measured the modulation transfer function (MTF) of the system, as shown in Fig. 13(c). It can be seen that spatial frequencies as high as 35 lp/mm (line pairs per millimeter) are supported, showing a spatial bandwidth product of over 2000.

Based on the above PSA scheme, Corzo *et al.* also realized the generation of multi-spatial-mode single-beam quadrature squeezed light, as shown in Figs. 14(a) and 14(b)[101]. This system can generate -3.0 ± 0.3 dB single-beam quadrature squeezing, as shown in Fig. 14(c). In addition, they also verified the multi-spatial-mode nature of the generated squeezed beam by studying the degree of squeezing versus spatially varying loss. Such multi-spatial-mode noiseless optical amplifier and vacuum squeezing source could be applied in quantum imaging techniques.

2.2.2 *Quantum squeezing enhancement in a two-beam phase-sensitive amplifier*

The PSA can also be used to enhance the level of IDS. In a recent work, Liu *et al.* found a different scheme to experimentally enhance two-beam quantum squeezing by utilizing the interference effect in the PSA based on the FWM process in hot atomic ensembles[102].

Different from the abovementioned PSA scheme with two nondegenerate pump beams, the schematic of this PSA is shown in Fig. 15(a). Weak probe and conjugate beams symmetrically intersect with a strong pump beam in the ^{85}Rb vapor cell. When the average input photon numbers of the input fields are much larger than one, i.e., $\langle \hat{N}_{a,\mathrm{in}} \rangle + \langle \hat{N}_{b,\mathrm{in}} \rangle \gg 1$, the IDS of this PSA can be given by

$$\mathrm{IDS} = \frac{1}{(2G-1) + 4\sqrt{G(G-1)}\frac{\sqrt{\eta}}{1+\eta}\cos\phi}, \tag{1}$$

where G is the intensity gain of the PSA, η is the power ratio of two inputs, and ϕ is the phase of the PSA.

With the same gain, the IDS of the PIA is $1/(2G-1)$[83]. Compared with the IDS of the PIA, there is an additional interference term in the denominator of Eq. (1). When the interference term is larger than zero, the IDS between probe and conjugate beams can be improved.

The detailed experimental layout is shown in Fig. 15(b). Liu *et al.* measured the IDS generated by PIA and PSA with identical experimental conditions, which is shown in Fig. 16.

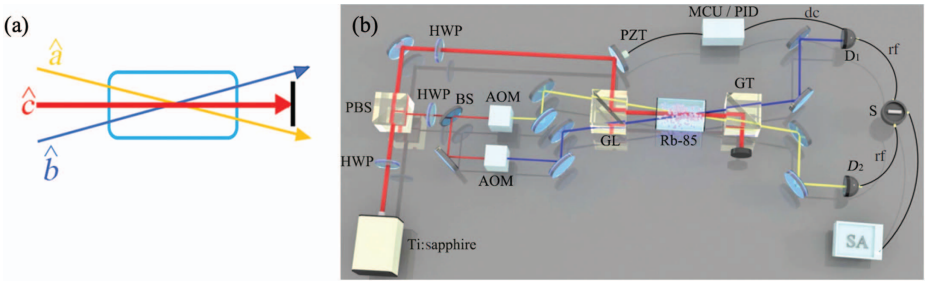

Fig. 15 (a) Configuration of PSA. $\hat{a}$ and $\hat{b}$ are the probe and conjugate beams, respectively. $\hat{c}$ is the pump beam. (b) Detailed experimental setup. HWP, half-wave plate; rf, radio frequency; D_1 (D_2), photodetector; S, subtractor. Adapted from [102].

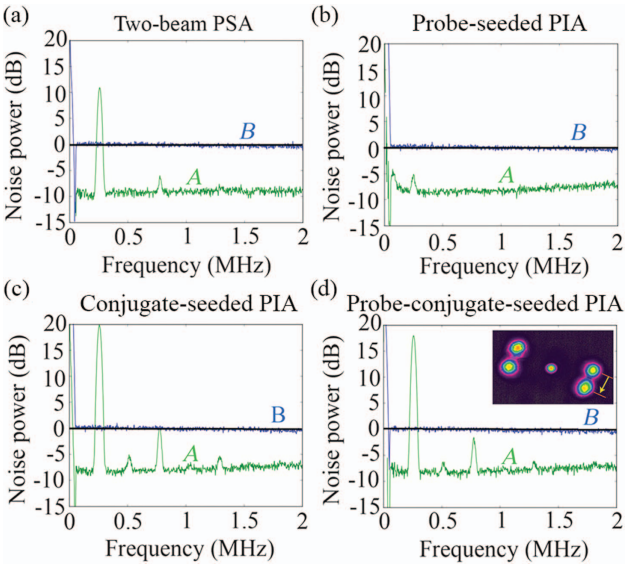

Fig. 16 IDS of two-beam PSA process (a), probe-seeded PIA process (b), conjugate-seeded PIA process (c), and probe-conjugate-seeded PIA process (d) under the same experimental situation. The inset of (d) shows the intensity profile of output fields of probe-conjugate-seeded PIA process. Adapted from [102].

It can be seen that IDS is increased from 8.97 ± 0.24 dB or 8.76 ± 0.26 dB to 10.13 ± 0.21 dB under the same experimental situation, and successfully exceeds 10 dB. This work provides an effective method to increase IDS and may have potential applications in improving the fidelity of QIP.

2.2.3 Phase manipulated two-mode entangled state from a phase-sensitive amplifier

The CV quantum entangled state is a valuable resource for quantum optics. The manipulation of the quantum entangled state is important for QIP. By utilizing a PSA based on the FWM process, Liu *et al.* experimentally implemented the phase manipulation of a quantum entangled state[103], which is shown in Fig. 17.

By manipulating the phase of the PSA, they obtained two different quadrature entanglements. As shown in Figs. 17(a) and 17(b), the amplitude-quadrature-difference and phase-quadrature-sum entanglement can be obtained by locking the phase of the PSA at zero. Differently, the amplitude-quadrature-sum and phase-quadrature-difference entanglement can be obtained by locking the phase of the PSA at π as shown in Figs. 17(c) and 17(d). This work is a new method for entanglement manipulation and may be applied to quantum communication and quantum metrology.

2.3 Multi-Beam Quantum Correlation

In Section 2.1 and Section 2.2, we review the generation of two-beam quantum correlation based on a PIA and a PSA utilizing the FWM process in hot atomic ensembles, respectively. In addition, multi-beam quantum correlation is the cornerstone for constructing quantum networks and finds wide applications in distributed quantum sensing[130,131] and multi-user quantum communication, such as quantum secret sharing[132], teleportation network[52], and controlled dense coding[9]. In this section, the generation of multi-beam quantum correlation from the FWM process is described.

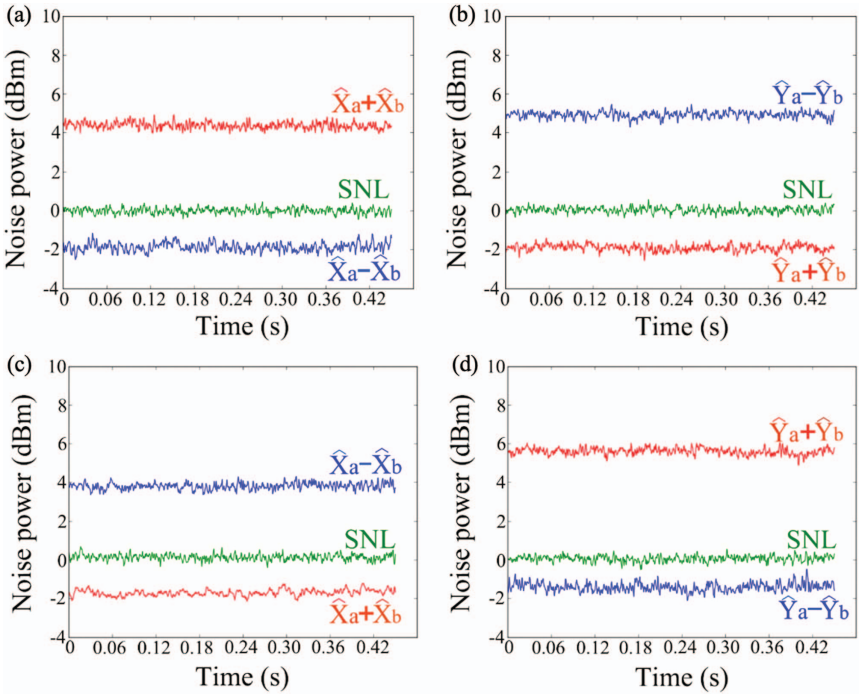

Fig. 17 Experimental results of amplitude-quadrature-difference (a) and phase-quadrature-sum (b) entanglement; experimental results of amplitude-quadrature-sum (c) and phase-quadrature-difference (d) entanglement. Adapted from [103].

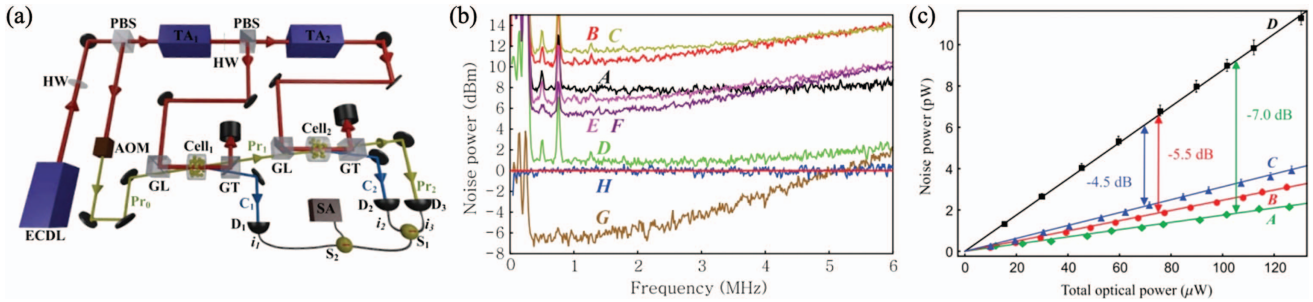

Fig. 18 (a) Experimental layout. (b) Noise powers of beams A–C, and their subtractions D–G. H is SNL of trace A–G. (c) Enhancement of quantum correlation. Adapted from [135].

2.3.1 Cascaded system

The initial triple quantum correlated beams are generated based on nonlinear crystal, such as OPO and linear optics[133] or two cascaded OPOs[134]. Qin *et al.* extended the cascaded system to the hot atomic ensemble and generated three quantum correlated beams[135].

The detailed experimental layout for generating triple quantum correlated beams by cascading two FWM processes is shown in Fig. 18(a). To verify the strong quantum correlation, Qin *et al.* measured the photocurrents of each beam and their subtractions. The results are shown in Fig. 18(b). They found that there is squeezing among the three beams, while there is no squeezing between any two beams, which indicates the triple quantum correlation generated by the cascaded FWM process.

To better illustrate the squeezing enhancement of this cascaded system, Qin *et al.* measured the squeezing of twin beams from a single vapor cell [trace B for cell_1 and trace C for cell_2 in Fig. 18(c)] and triple beams from the cascaded configuration (trace A). Trace D is their corresponding SNL. The ratios of slopes between curves B/C/A and D give the degrees of the IDS, 5.5 ± 0.1 dB, 4.5 ± 0.1 dB, and 7.0 ± 0.1 dB, respectively, showing that the squeezing level can be enhanced by this cascaded system. This scheme is immune to phase instabilities and has potential applications in the production of multiple quantum correlated beams.

In the abovementioned cascaded system, with the increase of the number of generated beams, the number of atomic vapor cells used will dramatically increase. The FWM process does not need an optical cavity due to its strong nonlinearity; therefore, multiple FWM processes can be spatially multiplexed in an atomic vapor cell.

Based on the concept of spatial multiplexing[93], Cao *et al.* proposed a method to generate quadruple quantum correlated beams with only two atomic vapor cells[136]. The detailed experimental layout is shown in Fig. 19(a). The generated twin beams from cell_1 are simultaneously seeded into cell_2 where they cross with pump_2 at the same angle but in a different plane. Under this configuration, two new beams are generated synchronously. The image of the output beams after cell_2 is shown in Fig. 19(b).

Subsequently, they measured the quantum noise of the individual beams and the quantum noise correlations of multiple beams, as shown in Fig. 20(a). It can be seen that the IDS of quadruple quantum-correlated beams is 8.2 ± 0.2 dB at 0.6 MHz below the SNL, showing a strong quadruple quantum correlation. Most importantly, Cao *et al.* show that the quantum correlation of quadruple beams can be enhanced from the quantum correlation generated in a single atomic vapor cell, as shown in Fig. 20(b). This work provides a new way to generate multiple quantum correlated beams with spatial multiplexing, in which the number of quantum correlated beams can be increased exponentially (2^n, where n is the number of atomic vapor cells).

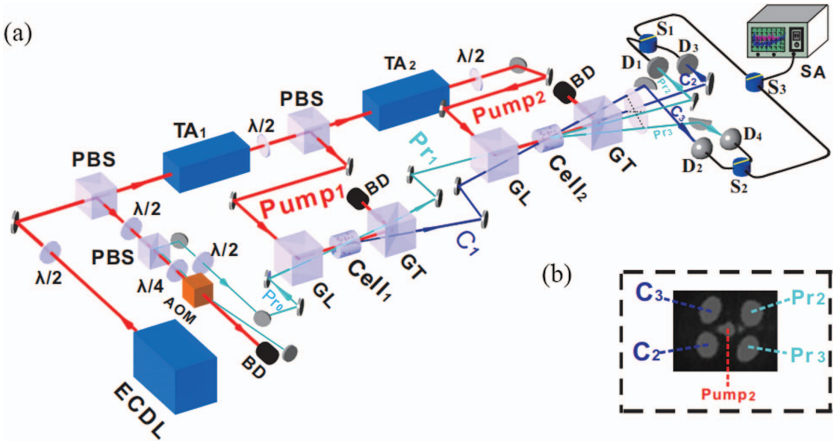

Fig. 19 (a) Experimental setup. $\lambda/2$, half-wave plate. (b) Image of the output beams. Adapted from [136].

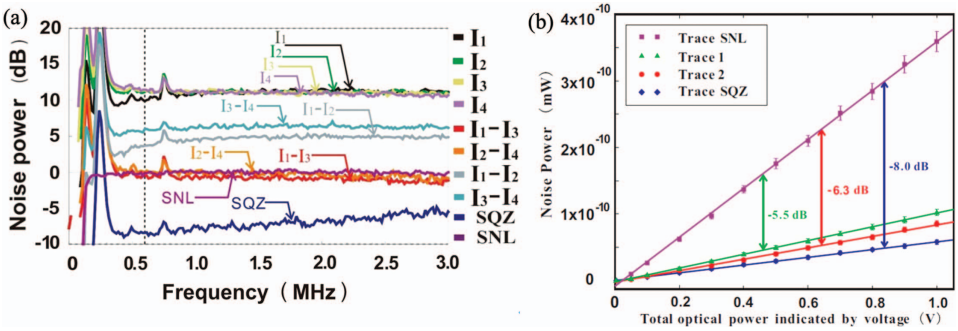

Fig. 20 (a) Noise power of different beams and their subtraction. (b) Enhancement of quantum correlation. Adapted from [136].

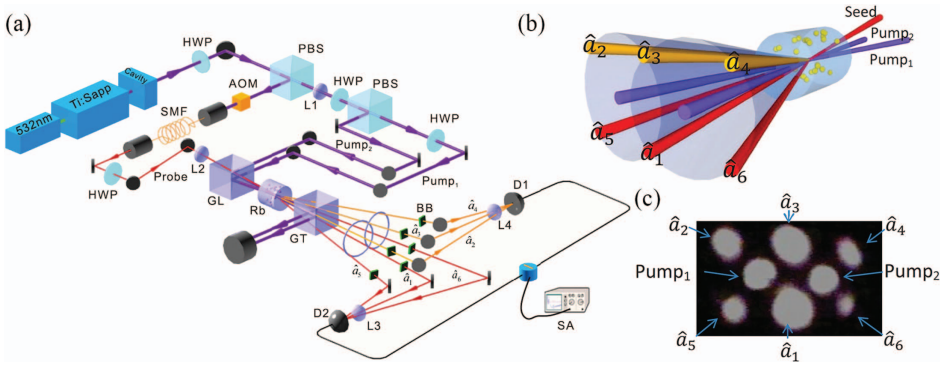

Fig. 21 (a) Detailed experimental layout. (b) Spatial structure of the output beams. (c) Image of the output beams. Adapted from [137].

2.3.2 Spatially structured pump system

The spatial multiplexing based on cascaded FWM in the previous subsection shares one pump beam for generating two independent FWM processes. At the same time, Wang *et al.*[137], Zhang *et al.*[138], Liu *et al.*[139,140], Swaim *et al.*[141], and Knutson *et al.*[142] also demonstrated the spatially multiplexed FWM process in an atomic vapor cell by utilizing a spatially structured pump. This subsection focuses on generating spatially separated six, ten, and fourteen quantum correlated beams, as well as four bright beams in this way.

The experimental setup to generate six quantum correlated beams by a spatially multiplexed FWM process is shown in Fig. 21(a). The two pump beams are crossed with an angle of 11 mrad and form the spatially structured pump, which is crossed with the seed probe beam in the center of the vapor cell. Under this configuration, seven FWM processes can be spatially multiplexed in an atomic vapor cell, accompanied by the generation of six spatially separated beams. The spatial structure of output beams and image are shown in Figs. 21(b) and 21(c), respectively.

The measured quantum correlations of the multiple quantum beams are shown in Fig. 22. It can be found that there is pairwise quantum correlation between $\hat{a}_1$ and $\hat{a}_3$. In addition, the IDS of the generated six beams is 4.2 ± 0.3 dB, indicating that there is quantum correlation among the generated six beams.

After the demonstration of the intensity-difference quantum correlation of six beams generated by a single atomic vapor cell, the question arises as to whether there is entanglement among them. To explore this, Zhang *et al.* employed six HDs to get the fluctuations of amplitude and phase quadratures of the six beams and constructed their covariance matrix[138]. The experimental layout for generating and detecting of hexapartite entanglement is shown in Fig. 23(a). The camera-captured intensity pattern is shown in Fig. 23(b). They found that the 31 symplectic eigenvalues in cases of different balanced pump powers are all smaller than one and decrease with the increase of pump power, showing a clear manifestation of hexapartite entanglement, as shown in Fig. 23(c). Most interestingly, they found that the entanglement structure characterized by subsystem entanglement distribution can be efficiently manipulated by tailoring the pump power ratio, showing the reconfigurability of the system. The results are shown in Fig. 24. This work provides the possibility to target a desired multipartite entanglement for a specific quantum information protocol and provides a new platform to generate large-scale spatially separated reconfigurable multipartite entangled states.

To increase the number of quantum correlated beams from the spatially multiplexed FWM process, Liu *et al.* demonstrated that the number of quantum correlated beams can be increased by changing the angle between the two pump beams[139]. The experimental setup to generate 10 quantum correlated beams is shown in Fig. 25(a). The angle between the two pump beams is changed to 5.3 mrad. Under this configuration, 10 quantum correlated beams can be generated. The output beams are shown in Fig. 25(b). The IDS of the generated 10 beams is 6.7 ± 0.3 dB at the sideband of 2 MHz as shown in

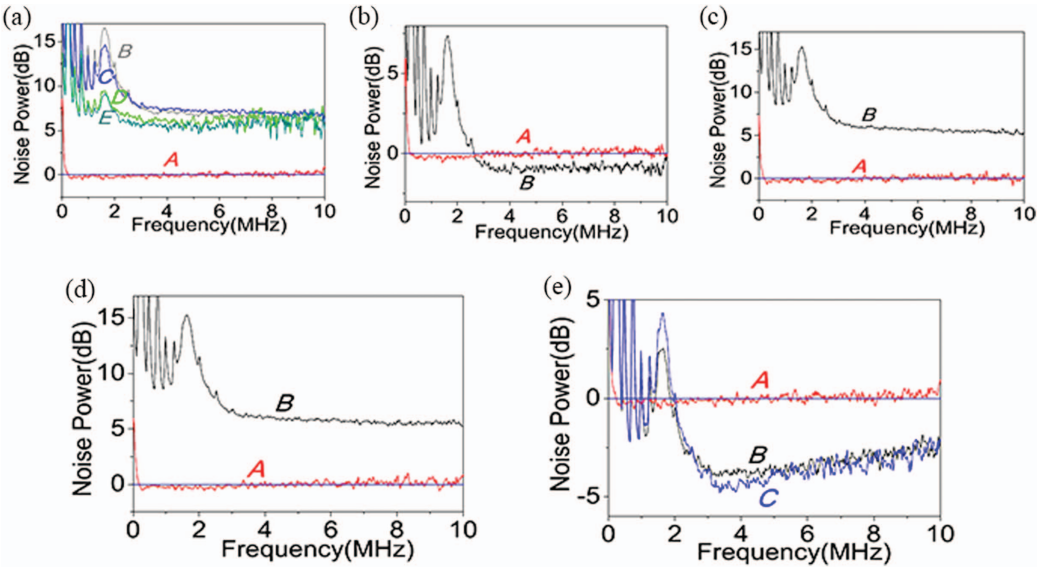

Fig. 22 Measured IDS of the six quantum correlated beams. (a) Noise powers of beams $\hat{a}_1$ (B), $\hat{a}_3$ (C), $\hat{a}_2$ (D), $\hat{a}_4$ (E), and their SNL (A). (b) Noise powers of subtraction $\hat{a}_1 - \hat{a}_3$ (B) and their SNL (A). (c) Noise powers of subtraction $\hat{a}_1 - \hat{a}_2$ (B) and their SNL (A). (d) Noise powers of subtraction $\hat{a}_1 - \hat{a}_4$ (B) and their SNL (A). (e) Noise powers of subtraction $\hat{a}_1 - \hat{a}_2 - \hat{a}_3 - \hat{a}_4$ (B), $\hat{a}_1 - \hat{a}_2 - \hat{a}_3 - \hat{a}_4 + \hat{a}_5 + \hat{a}_6$ (C) and their SNL (A). Adapted from [137].

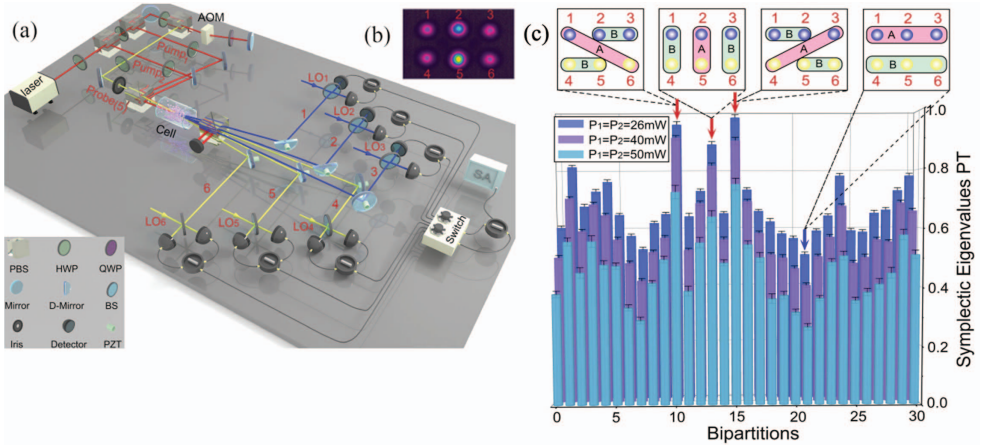

Fig. 23 (a) Detailed experimental layout for generating hexapartite entanglement; (b) output beams; (c) 31 symplectic eigenvalues in the cases of different balanced pump powers. Adapted from [138].

Fig. 25(c), revealing a strong quantum correlation among the 10 beams.

Will the number of generated beams further increase if the angle of the two pump beams is further reduced? Liu *et al.* proposed a method to flexibly change the angle through the spatial light modulator (SLM)[140]. By changing the holograms loaded onto the SLM, the angle of the two pump beams can be adjusted flexibly. The effects of angle, one-photon detuning, and two-photon detuning on the degrees of IDS and the number of beams are shown in Figs. 26(a)–26(c), respectively. They found that 14 quantum correlated beams with an IDS of 6.29 dB can be achieved when the angle between the two pump beams is 3.6 mrad, one-photon detuning is 0.8 GHz, and two-photon detuning is 4 MHz. The generated quantum correlated beams can be increased by shining more pump beams. These spatially separated quantum correlated beams may find applications in building a multi-user quantum network and realizing multi-parameter quantum metrology.

In addition to using a SLM to adjust the angle between two pump beams, Swaim *et al.* also proposed a new FWM geometry with a structured pump, which is generated by using near-field diffraction through a slit[141]. As shown in Fig. 27(a), the spontaneous FWM geometries of the asymmetrically structured pump and circularly symmetric pump are different. When a rectangular slit with a width of 530 μm is placed 76 mm in front of the center of the vapor cell, the experimental and theoretical images

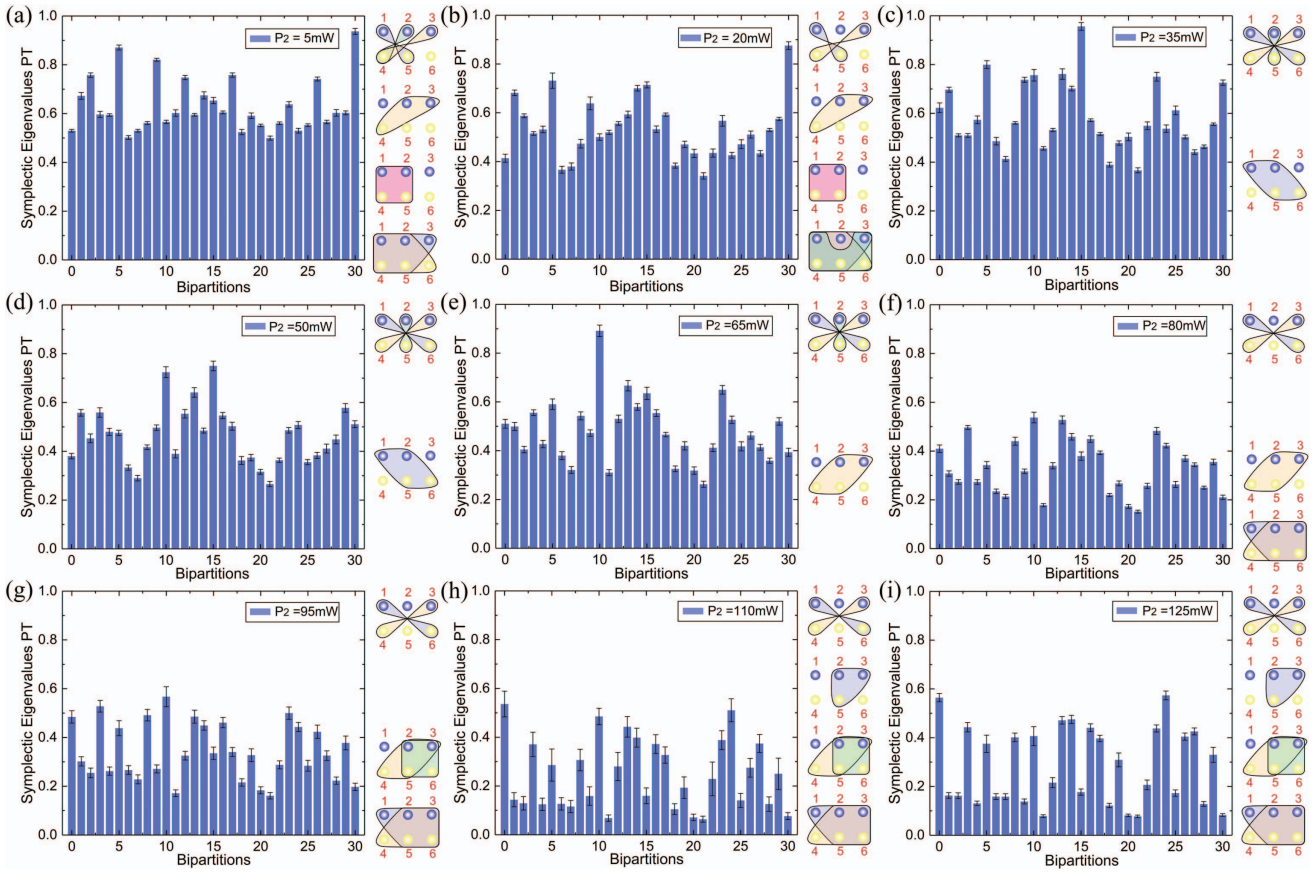

Fig. 24 Reconfigurable hexapartite entanglement by tailoring the power ratio of the two pump beams. Adapted from [138].

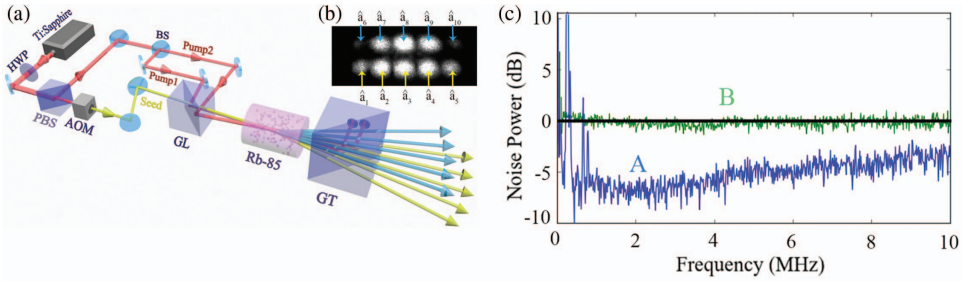

Fig. 25 (a) Experimental layout; (b) output beams; (c) measurement of 10-beam quantum correlation. Adapted from [139].

of the output are shown in Figs. 27(b) and 27(c), respectively. The six-spot geometry is obtained under this diffracting pump, whose intensity profiles along the propagation coordinate are shown in Fig. 27(d). Moreover, the IDS between the probe (2) and conjugate (5) is measured. The maximum squeezing is 1.2 dB around 1 MHz, as shown in Fig. 27(e).

With dual-pump FWM processes, Knutson *et al.* also demonstrated the generation of four bright beams through an unseeded multimode FWM process in a hot ^{85}Rb vapor cell[143]. An experimental diagram for generating four bright beams is shown in Fig. 28(a). Two strong pump beams with a small separation angle cross at a 25.4 mm long ^{85}Rb vapor cell heated at 145°C. As shown at the top of Fig. 28(b), the FWM cones generated from individual pumps become four spatially separated modes when both pumps exist. Total output power is minimum when the power ratio of two pump beams is near one, as shown at bottom of Fig. 28(b).

So far, with the spatially structured pump based FWM process, the maximum six quantum entangled beams and fourteen quantum intensity-difference correlated beams have been demonstrated. Another possible way to increase the number of quantum correlated beams is to introduce more complex pump structures, such as three or more pump beams[137]. With the increase of quantum correlated beams, it is challenging to verify the entangled properties of these beams since more HDs need to be employed. At present, a promising way to increase the scale

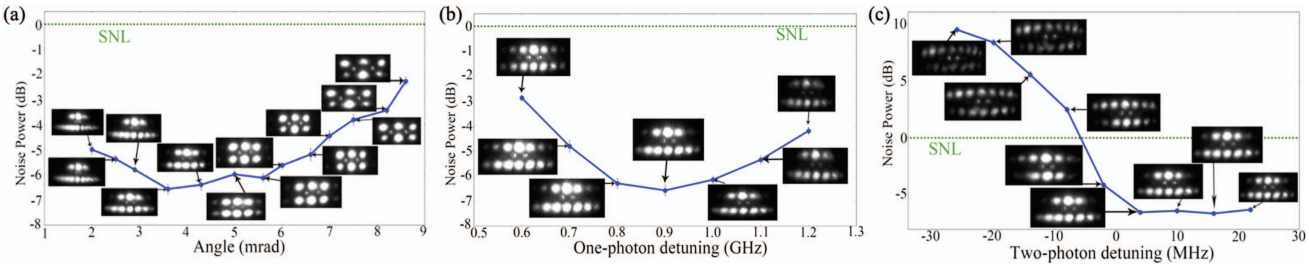

Fig. 26 Effect of the angle between the two pump beams (a), one-photon detuning (b), and two-photon detuning (c) on the number of quantum correlated beams. Adapted from [140].

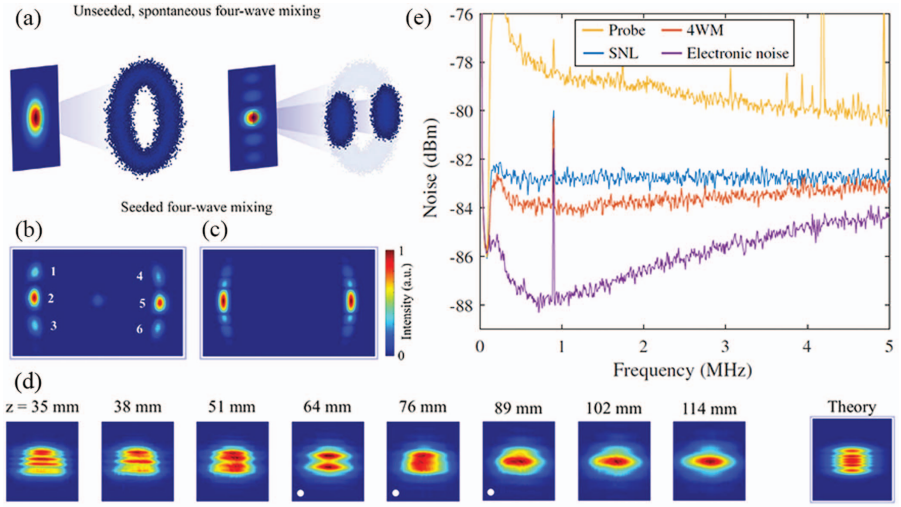

Fig. 27 (a) Unseeded, spontaneous FWM geometries for a circularly symmetric pump (left) and an asymmetrically structured pump (right). (b) Output image of FWM when seeded by a weak probe beam. (c) Output image in theory. (d) Experimental intensity images of the diffracting pump along the propagation direction. The theoretical pump profile in the center of the cell is also shown. (e) Measured IDS between beams 2 and 5. Adapted from [141].

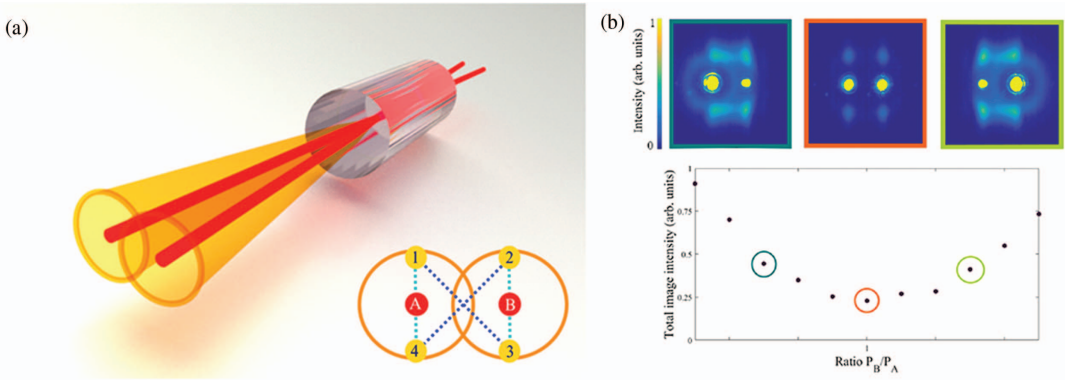

Fig. 28 (a) Experimental diagram. (b) Top: images when the power ratio of P_A to P_B is changed. Bottom: total intensity of output light, excluding pump beams, as a function of ratio P_B/P_A. Adapted from [143].

of quantum correlation is using the multiplexing method, which will be discussed in the next subsection.

2.4 Quantum Correlation between Orbital Angular Momentum Modes

The OAM of light is potentially useful for the manipulation of small objects[144], the encoding of information[145], and the transfer of OAM to atoms[146]. In principle, OAM has an infinite number of modes[147]. All these modes are orthogonal and do not affect each other. Therefore, OAM has attracted a lot of attention in recent years. For quantum information, especially in the field of DV quantum information, OAM has been widely studied, including two-photon[15,148] and multi-photon high-dimensional entanglement[17] based on OAM. In recent years, the applications of OAM in the field of CV quantum information have also developed rapidly.

2.4.1 Two-beam quantum correlation between orbital angular momentum modes

In 2008, Marino *et al.* introduced OAM to the FWM process based on atomic vapor and experimentally implemented the intensity-difference-squeezed twin Laguerre–Gauss beams of light carrying OAM[149]. In addition, they also demonstrated the delocalized spatial correlations between the twin beams.

Two different scenarios are demonstrated with an OAM beam serving as a probe or pump beam as shown in Figs. 29(a) and 29(c), respectively. The IDSs of probe and conjugate beams in these two scenarios are −6.7 dB and −4.4 dB, respectively. To study the spatial distribution of the intensity correlations, they equally attenuated the beams in several different ways. In the spirit of the Mandel Q parameter, as mentioned in Subsection 2.1.3, they plot the quantity Q = (intensity-difference noise)/SQL−1 versus the fractional transmitted intensity, as shown in Figs. 29(b) and 29(d). The probe beam is correlated to a limited area of the conjugate beam. The different behaviors of these four different ways show the multimode nature of OAM modes. This study enables further progress in the direction of CV QIP with OAM beams.

2.4.2 Orbital angular momentum multiplexed two-beam entanglement

Entanglement is a very important quantum resource that can be used to realize CV QIP. Improving the capacity of CV quantum entanglement is important for realizing a large-scale quantum information network. Multiplexing is an important way to improve the information carrying capacity of classical communication systems. For classical communication, OAM can greatly improve the data capacity through multiplexing[150–153]. In previous studies[16,21,22,154–173], OAM greatly increased the information capacity and brought new applications. In this subsection, multiplexing and optical OAM are combined and then applied to CV entangled systems.

Pan *et al.* proposed and generated high-capacity CV entanglement by applying OAM mode multiplexing in the CV system[29]. The detailed experimental layout is shown in Fig. 30. In the experiment, Pan *et al.* used a strong pump beam to seed into the hot ^{85}Rb vapor cell, leading to the generation of multiple pairs of $\mathrm{LG}_{l,\mathrm{pr}}$ and $\mathrm{LG}_{-l,\mathrm{conj}}$ modes in probe and conjugate beams, respectively, where l corresponds to the topological charge of the OAM mode.

They measured the covariance matrix of these optical OAM modes by using the HD technique. The experimental results are illustrated in Fig. 31. It can be found that 13 pairs of entangled Laguerre–Gauss modes are simultaneously generated. They also demonstrated that there is no quantum entanglement between $\mathrm{LG}_{l,\mathrm{pr}}$ and $\mathrm{LG}_{l,\mathrm{conj}}$ ($l \neq 0$) modes in the system, showing that the nonlinear interaction obeys the conservation of OAM. In addition, the quantum entanglement characteristics of three different OAM coherent superposition modes are also studied.

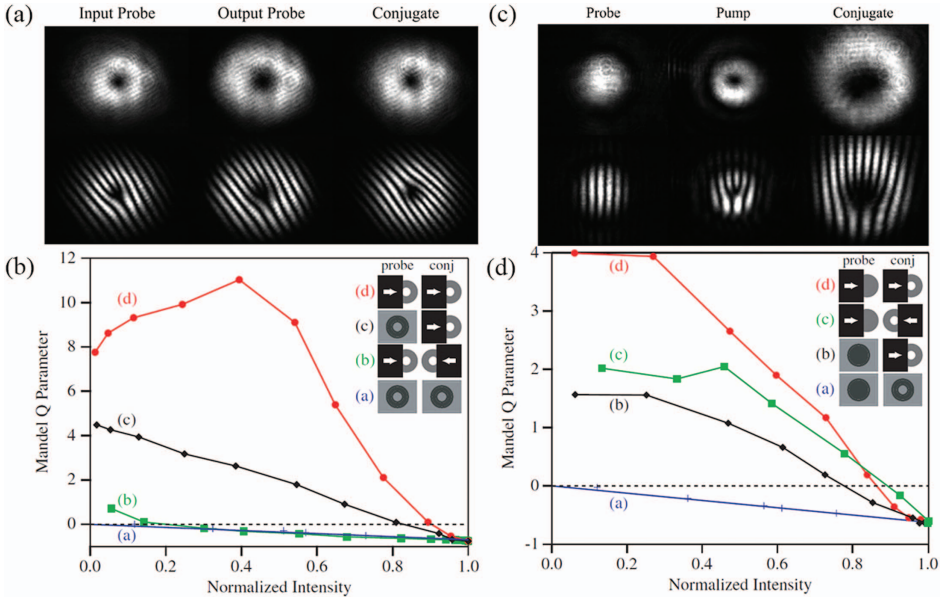

Fig. 29 (a) Intensity distribution (upper) and phase interferogram (lower) when OAM beam serves as probe beam. (b) Mandel Q parameter of the intensity difference versus the transmittance as the two beams are attenuated equally. (c), (d) Similar to (a), (b) as the OAM beam serves as pump beam. Adapted from [149].

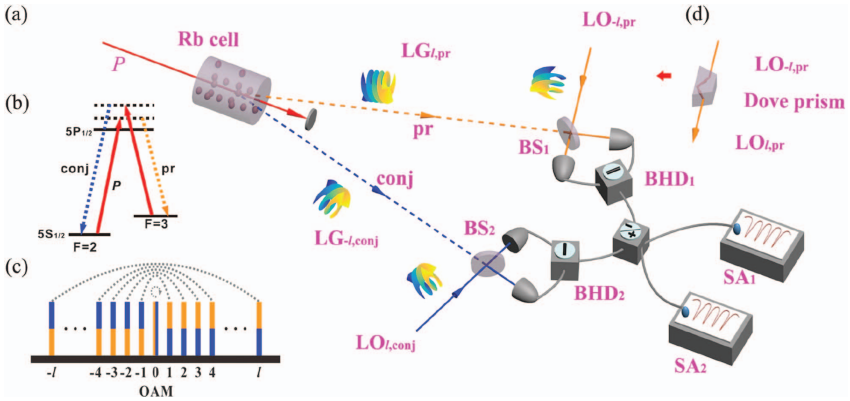

Fig. 30 (a) Detailed experimental setup. (b) Double-Λ energy level diagram of ^{85}Rb D_1 line transition. (c) OAM spectrum from the FWM process. (d) Dove prism is used to transfer $LG_{-l,pr}$ to $LG_{l,pr}$. Adapted from [29].

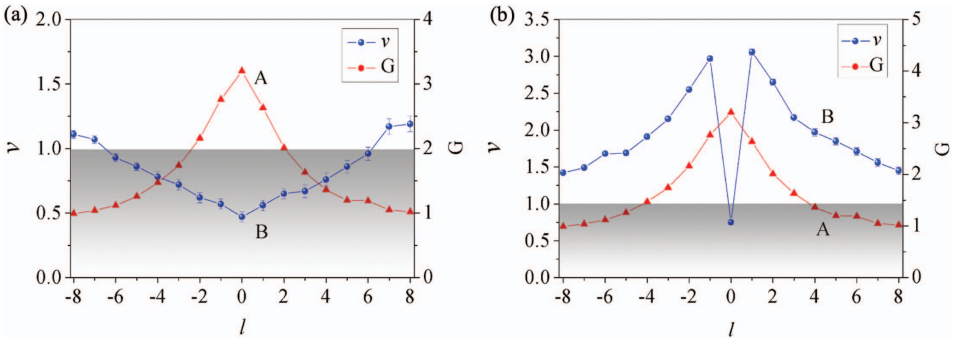

Fig. 31 (a) Entanglement test between $LG_{l,pr}$ and $LG_{-l,conj}$ versus topological charge l. (b) Entanglement test between $LG_{l,pr}$ and $LG_{l,conj}$ versus topological charge l. Trace A is the intensity gain of probe beam and trace B is the symplectic eigenvalue. Adapted from [29].

The results are shown in Fig. 32. Pan *et al.* applied the concept of OAM multiplexing to the CV regime and greatly improved the entanglement capacity of the system. This work provides a new platform to study CV quantum communication.

2.4.3 *Orbital angular momentum multiplexed tripartite entanglement*

The study in the previous subsection is limited to OAM multiplexed bipartite entanglement. Multipartite entanglement[52,174] is a necessary resource to realize quantum networks[2] and quantum computation[175]. OAM multiplexing and multipartite entanglements are combined here for realizing OAM multiplexed tripartite entanglement[176].

Li *et al.* generated OAM multiplexed tripartite entanglement from a cascaded FWM process. Figure 33 shows the experimental layout. The measurement method is the same as that in the previous subsection. The measurement results show that there are both tripartite entanglement and bipartite entanglement in the system. As shown in Fig. 34, the cascaded FWM system can generate nine groups of OAM multiplexed tripartite

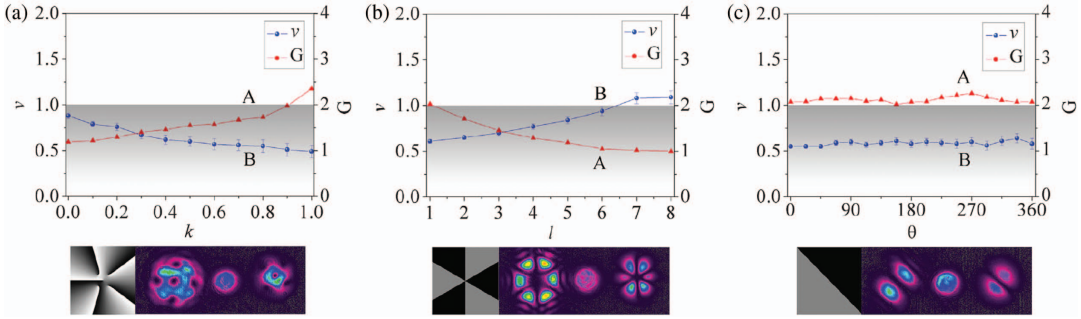

Fig. 32 Entanglement meaurement of (a) $\sqrt{k}LG_{1,pr} + \sqrt{1-k}LG_{5,pr}$, (b) $LG_{l,pr} + LG_{-l,pr}$, and (c) $LG_{1,pr} + e^{2i\theta}LG_{-1,pr}$. Adapted from [29].

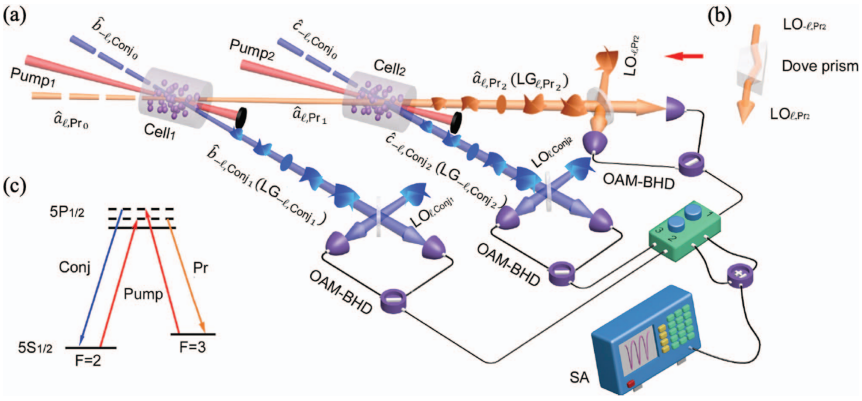

Fig. 33 (a) Detailed experimental setup. (b) Double-Λ energy level diagram. (c) Dove prism is used to transfer $LG_{-l,pr2}$ to $LG_{l,pr2}$. Adapted from [176].

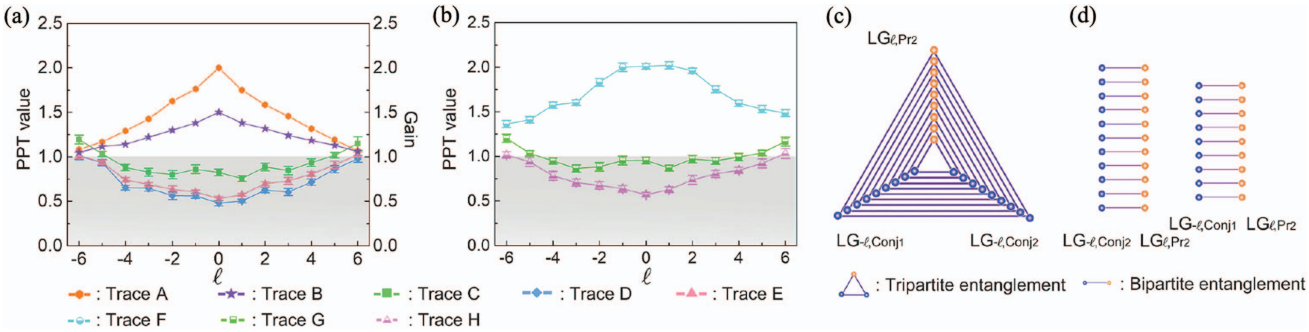

Fig. 34 (a) Witnessing the OAM multiplexed tripartite entanglement. Traces A and B represent the gains of $cell_1$ and $cell_2$, respectively. Traces C, D, and E represent three symplectic eigenvalues. (b) Witnessing the OAM multiplexed bipartite entanglement. Traces F, G, and H represent three symplectic eigenvalues. Diagram of OAM multiplexed (c) tripartite and (d) bipartite entanglement. Adapted from [176].

entanglement [shown in Fig. 34(c)] and twenty groups of OAM multiplexed bipartite entanglement [shown in Fig. 34(d)].

At the same time, they also proved that no tripartite entanglement exists between modes $LG_{-l,pr2}$, $LG_{-l,conj1}$ and $LG_{-l,conj2}$, meaning that OAM conservation in the system is necessary for preparing multipartite entanglement. The experimental results are shown in Fig. 35(a). Finally, they studied the tripartite entanglement for coherent OAM superposition modes. As shown in Figs. 35(b)–35(d), for three different types of OAM superposition modes, tripartite entanglement exists.

2.4.4 *Large-scale quantum network over 66 orbital angular momentum optical modes*

In the previous subsection, tripartite entanglement is realized by the cascaded FWM process. However, the complexity of the experimental layout will increase significantly as the number of entangled beams increases. Wang *et al.* innovatively combined

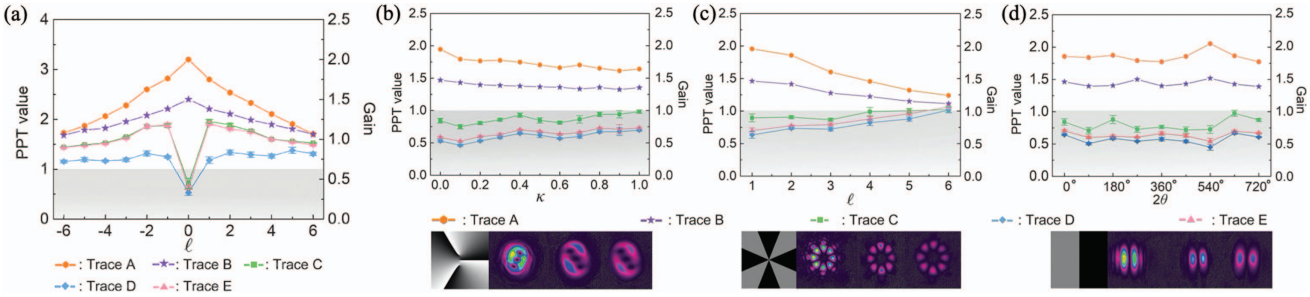

Fig. 35 (a) Measurements of OAM multiplexed tripartite entanglement. (b)–(d) Measurements of the tripartite entanglement for coherent OAM superposition modes. Adapted from [176].

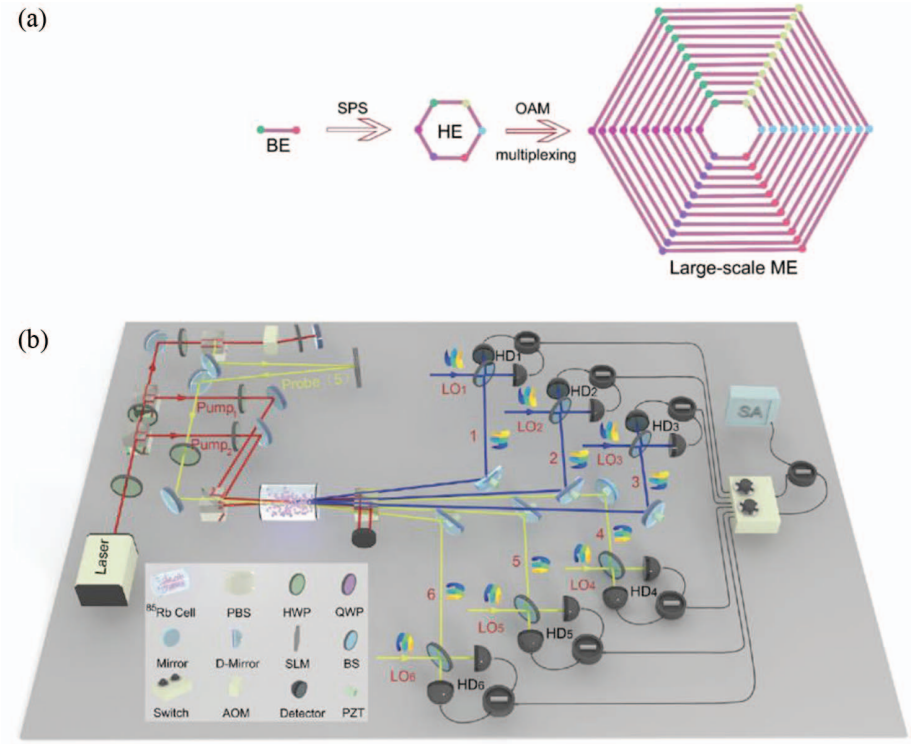

Fig. 36 (a) Principle for generating large-scale multipartite entanglement. (b) Detailed experimental setup. Adapted from [177].

spatial pump shaping technology with OAM multiplexing, and a large-scale multipartite entanglement over 66 OAM modes was deterministically generated[177].

The principle of the scheme is illustrated in Fig. 36(a). By using a pump shaping technique, the number of entangled beams is increased to six (Subsection 2.3.2). Then, by using OAM multiplexing, each node of hexapartite entanglement can possess 11 orthogonal multiplexed channels, resulting in the production of a large-scale quantum network over 66 OAM modes. The experimental setup is shown in Fig. 36(b). The increase of topological charge number is limited by the overlap between six OAM modes of the output light field. Therefore, they measured the covariance matrix of topological charge from −5 to 5. The results show that all 31 symplectic eigenvalues are less than one, which means that 11-OAM multiplexed hexapartite entanglement is generated, as shown in Fig. 37. In recent years, the integrated quantum optical platform has exhibited great potential in QIP because of its compact, scalable, and stable advantages[178–181]. Therefore, it is possible to combine this large-scale quantum network scheme with the

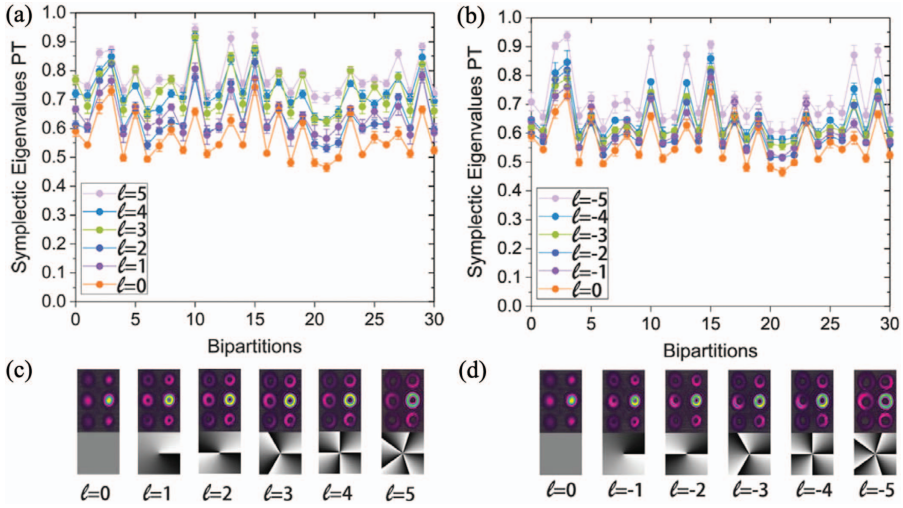

Fig. 37 (a), (b) Measurements of large-scale multipartite entanglement for different topological charges *l*. (c), (d) Holograms loaded on the SLM and the six output LG beams. Adapted from [177].

integrated optical platform for constructing a large-scale on-chip quantum network.

In addition to the OAM of light, the spatial orthogonal Hermite–Gaussian mode can also be utilized to enhance the channel capacity. As discussed in Section 1, the number of entangled modes has been increased with different DOFs of light, such as time[27,28,60], space[61], and frequency[62–65]. It can be supposed that the scale of entanglement can be further increased by enhancing both the channel capacity and the number of entangled modes, which is useful for constructing more complex quantum networks.

3 Applications in Quantum Information Protocols

Quantum information protocols are devoted to achieving high-security, high-fidelity, and high-capacity information transmission and processing methods. Utilizing the optical quantum states introduced above, several high-capacity and high-fidelity quantum information protocols are developed as described in this section. Moreover, the all-optical characteristic of these protocols affords them great potential to largely enhance the bandwidth of QIP.

3.1 Orbital Angular Momentum Multiplexed All-Optical Quantum Teleportation

Quantum teleportation is one of the most important and attractive protocols in quantum information. By utilizing this protocol, the high-fidelity disembodied transportation of unknown quantum states can be realized. Since the concept of quantum teleportation was proposed in 1993[182], it has attracted extensive attention all over the world, and has made great progress in both experiment[67,68,154,183–196] and theory[66,197,198]. In recent years, a series of breakthroughs in long-distance quantum teleportation has been demonstrated[191–193].

In addition to the transmission distance, the information transmission capacity is another important index to measure the performance of quantum teleportation. In classical optical communication, multiplexing can greatly improve the information transmission capacity by combining multiple communication channels into one channel. Therefore, the development of a multiplexed quantum teleportation system will greatly improve its information transmission capacity. In a recent work, Liu *et al.* experimentally constructed nine-channel multiplexed all-optical quantum teleportation (AOQT) by fully utilizing the high-capacity characteristics of a multiplexed quantum entanglement source[199]. More importantly, they experimentally demonstrated the simultaneous teleportation of two independent and orthogonal OAM[147] modes, which ensured the increase of information transmission capacity[150,200].

The configuration of OAM multiplexed AOQT is shown in Fig. 38(a). The CV OAM multiplexed EPR entanglement source is generated based on an OPA with the gain of $G_{1,l}$. Then, it is distributed to Alice and Bob participating in the multiplexed AOQT. Alice utilizes a high-gain OPA with the gain of $G_{2,l}$ to amplify the input state $\hat{a}_{\mathrm{in},l}$ with the help of $\hat{b}_{2,-l}$ (EPR entanglement), and transmits the amplified state $\hat{a}_{\mathrm{c},l}$ to Bob through an all-optical channel without measurement. After receiving the amplified state, to retrieve the input state, Bob uses a linear BS with a transmission of $\varepsilon = 1/G_{2,l}$ to couple $\hat{a}_{\mathrm{c},l}$ and $\hat{b}_{1,l}$. The retrieved state can be expressed as

$$\hat{a}_{\mathrm{out},l} = \hat{a}_{\mathrm{in},l} + \frac{\sqrt{G_{2,l}-1}}{\sqrt{G_{2,l}}}(\hat{b}^{\dagger}_{2,-l} - \hat{b}_{1,l}). \tag{2}$$

When $G_{1,l}$ and $G_{2,l}$ are all much larger than one, the last term of Eq. (2) will vanish. Under this situation, the output state equals the input state $\hat{a}_{\mathrm{in},l}$, i.e., realizing quantum teleportation. The corresponding fidelity can be given as

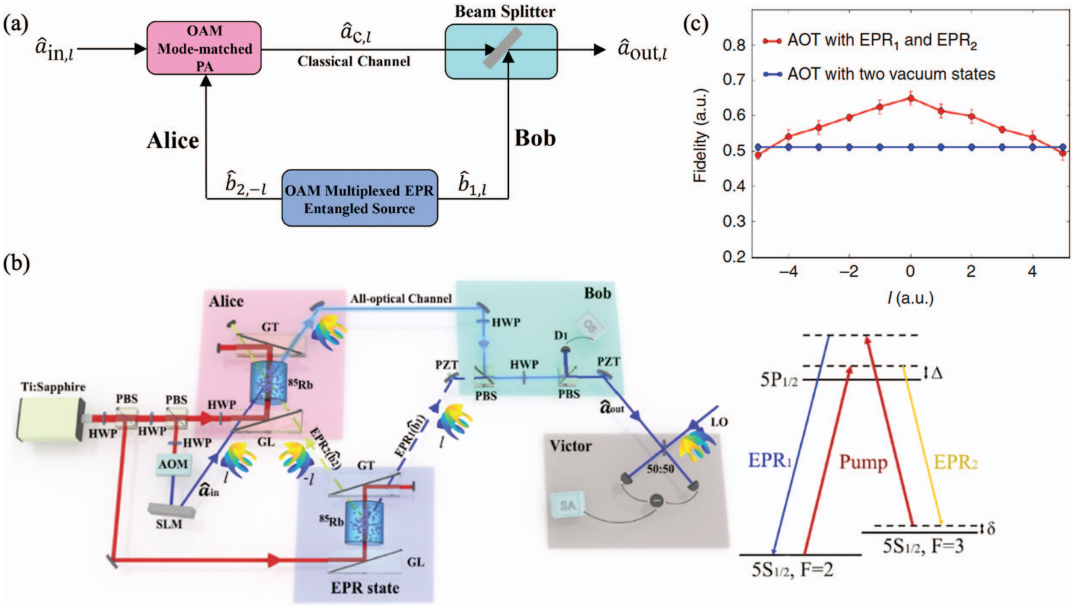

Fig. 38 (a) Configuration of OAM multiplexed AOQT. (b) Detailed experimental setup of OAM multiplexed AOQT. (c) Fidelity of OAM multiplexed all-optical teleportation (AOT) with different OAM channels. Adapted from [199].

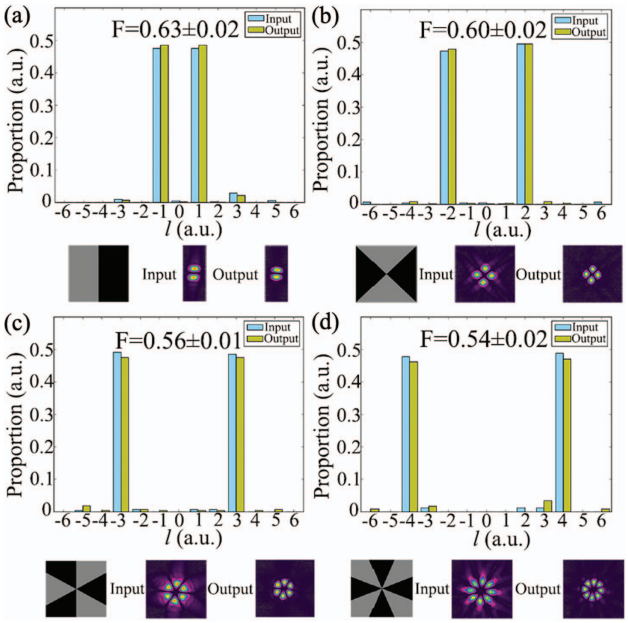

Fig. 39 (a)–(d) Fidelities of simultaneously teleported OAM superposition modes $\hat{a}_{in} = \hat{a}_{in,l} + \hat{a}_{in,-l}$. Adapted from [199].

$$F = \frac{1}{1 + \frac{G_{2,l}-1}{G_{2,l}}\left(\sqrt{G_{1,l}} - \sqrt{G_{1,l}-1}\right)^2}. \quad (3)$$

The detailed experimental layout is shown in Fig. 38(b). Liu *et al.* experimentally constructed nine quantum teleportation channels with fidelity surpassing the corresponding classical limit. The corresponding experimental results are shown in Fig. 38(c).

To demonstrate that OAM multiplexed AOQT has the advantage of enhancing information transmission capacity, Liu *et al.* simultaneously encoded two independent and orthogonal OAM modes into the input state. Using the OAM multiplexed AOQT constructed above, the high-fidelity reconstruction of the input state beyond the classical limit was realized, showing the advantages of this system in improving information capacity. The corresponding experimental results are shown in Fig. 39. This work opens an avenue to the deterministic realization of a multi-channel parallel quantum communication protocol, and provides a platform for the construction of a high-capacity all-optical quantum communication network.

3.2 All-Optical Entanglement Swapping

The entanglement swapping protocol is one of the most crucial protocols in QIP. Because the entanglement swapping protocol can entangle two particles without direct interaction, it is considered to be the core unit of a quantum repeater[201]. Since the entanglement swapping protocol was first proposed in 1993[202], it has attracted great attention in quantum information and has achieved remarkable progress in DV and CV regimes[2,71,156,203–211]. In the CV regime, Bell-state measurement based on optic-electro and electro-optic conversion is needed to realize entanglement swapping, which greatly limits the application of entanglement swapping in constructing broadband quantum networks. To address this issue, Liu *et al.* proposed and experimentally realized an all-optical entanglement swapping (AOES) protocol without measurement[212]. In this protocol, the low-noise OPA based on the FWM process[72,102,199,213] is utilized to amplify the input state with high gain, avoiding the use of optic-electro and electro-optic conversion. Therefore, the function of the Bell-state measurement in the traditional scheme is realized without measurement.

The detailed experimental layout of AOES is shown in Fig. 40. In this experiment, first, two sets of FWM processes are utilized to generate two independent quantum entanglement sources (EPR_1 and EPR_2). Alice (Bob) has one beam of EPR_1 (EPR_2). Then, the remaining two beams of the two independent EPR entanglements are transmitted to Claire through the 4f imaging system. Claire extracts the quantum information of these two beams through a high-gain low-noise OPA based on the FWM process, and then transmits the extracted quantum information to Bob through the all-optical channel. Finally, by utilizing the linear optical BS, Bob transfers the received quantum information to the beam he has, so as to complete AOES. After completion of AOES, two initially independent fields have the characteristics of quantum entanglement without direct interaction.

The experimental results measured by Liu *et al.* are shown in Fig. 41. After completion of AOES, the amplitude-quadrature-difference (phase-quadrature-sum) variance of the two initially

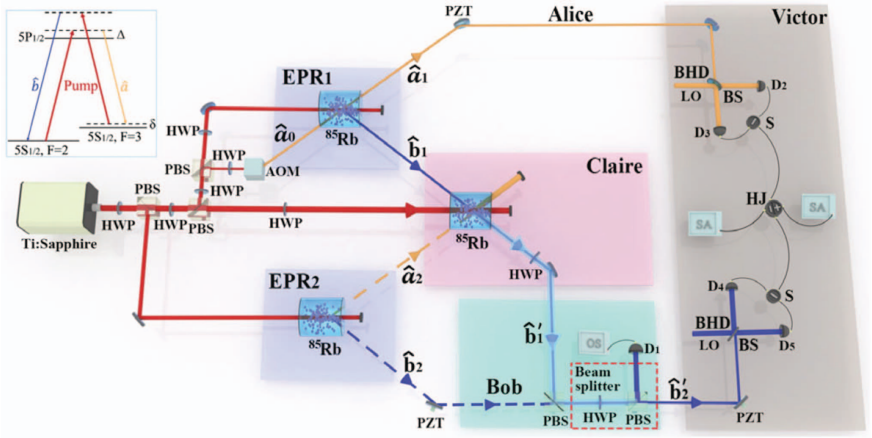

Fig. 40 Detailed experimental setup of AOES. Adapted from [212].

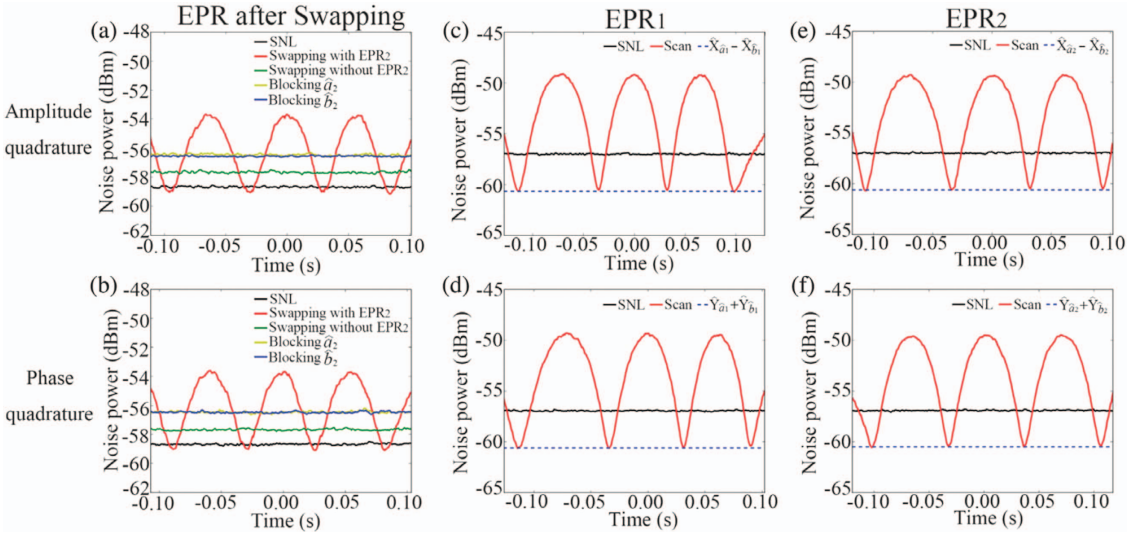

Fig. 41 Experimental results of AOES. Variance of (a) amplitude-quadrature difference and (b) phase-quadrature sum between $\hat{a}_1$ and $\hat{a}'_2$. (c), (e) are similar to (a) and (d), (f) are similar to (b) except that the states are EPR_1 and EPR_2. Adapted from [212].

independent fields is 0.43 ± 0.06 dB (0.42 ± 0.05 dB) below the corresponding SNL, showing significant quantum entanglement characteristics between these two fields.

To demonstrate the broadband characteristics of AOES in the experiment, Liu *et al.* also measured the bandwidth of AOES. The experimental results showed that the AOES can be realized within a certain bandwidth range. In addition, they measured the anti-loss characteristics of the all-optical channel of AOES, which demonstrated that this scheme can still complete AOES when the channel loss is as high as 70%. This work provides an all-optical version for the realization of entanglement swapping and opens an avenue to construct all-optical broadband quantum networks without measurement.

3.3 Low-Noise Amplification of a Quantum State

A PIA for an optical state is important for realizing quantum information tasks, in particular, as part of a quantum cloner to copy a quantum state. Based on the cascaded FWM process, Pooser *et al.* experimentally realized a low-noise and phase-insensitive optical amplifier[213].

The experimental scheme of low-noise amplification is shown in Fig. 42(a). The first cell is used to generate entangled probe and conjugate beams, while the second cell is used to amplify the conjugate beam. A neutral density (ND) filter is used to attenuate the amplified beam to initial power. Entanglement measurements of the initial, amplified, and attenuated states are shown in Fig. 42(b). It can be found that entanglement has an amplifier gain of 1.8. To further analyze the limit of the gain, the degree of entanglement versus gain is shown in Fig. 42(c). Two different entanglement criteria are employed. One is an inseparable criterion: $I = (\Delta\hat{X}_-)^2_N + (\Delta\hat{Y}_+)^2_N < 2$. The other is an EPR criterion: $E_{ij} = V_{X_i|X_j} \cdot V_{Y_i|Y_j} < 1$, where $V_{X(Y)_i|X(Y)_j}$ is the condition variance of system i given system j. The state is inseparable ($I < 2$) for a gain as large as 2.8. In particular, under a gain of two followed by 50% attenuation, it can be seen as a quantum cloner. In contrast, EPR correlations are maintained up to a gain of 1.2, showing that excess noise is introduced to the conjugate by the amplifier, thus unbalancing the variances. Due to multi-spatial modes of correlated

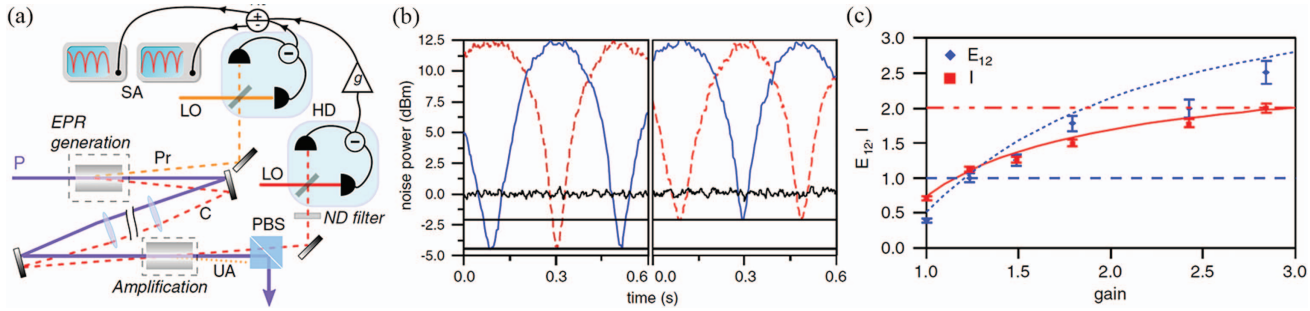

Fig. 42 (a) Experimental setup of low-noise amplification. (b) Squeezing trace at 1 MHz for quadratures at two different amplifier gains. The left traces show the squeezing level with no amplification and no attenuation. The right traces show the squeezing with an amplification of 1.8 and an attenuation of 56%. (c) E_{12} and I versus gain. Adapted from [213].

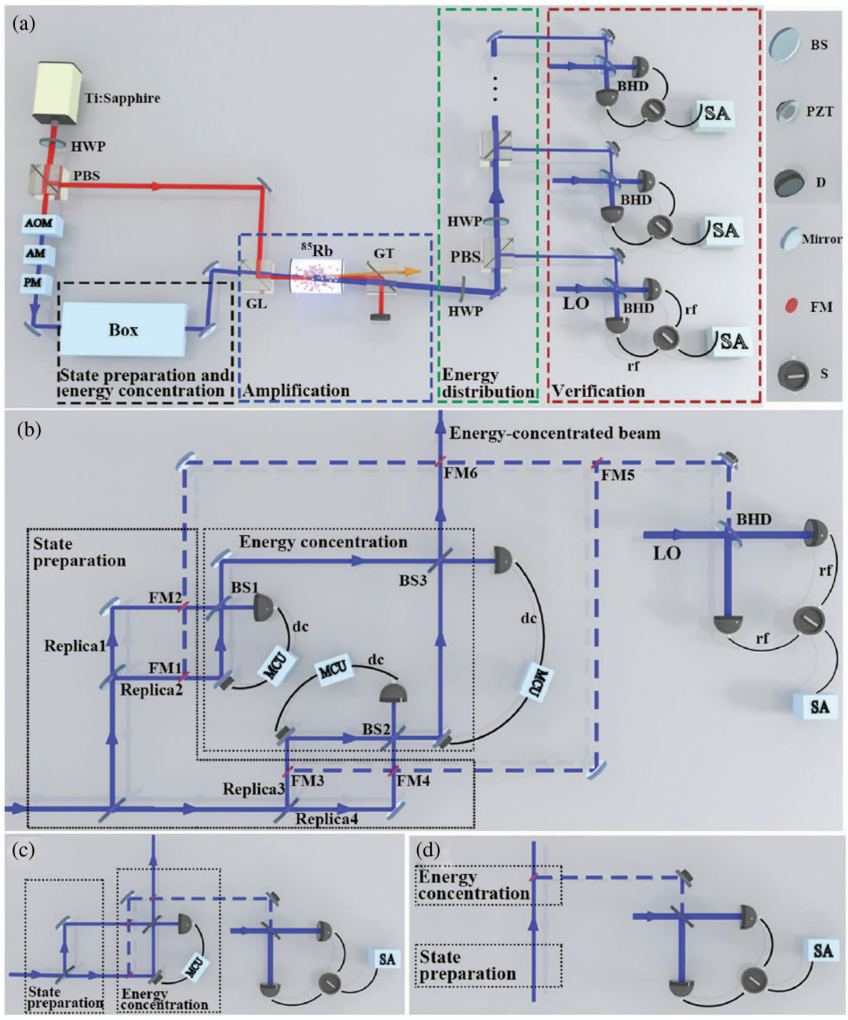

Fig. 43 Detailed experimental setup of all-optical optimal $N \rightarrow M$ quantum cloning. Adapted from [227].

beams, the amplifier can realize the cloning of quantum images.

3.4 All-Optical Optimal N-to-M Quantum Cloning

According to the basic laws of quantum mechanics, it is impossible to clone unknown quantum states perfectly[214,215]. Nevertheless, the basic laws of quantum mechanics do not prohibit the incomplete cloning of unknown quantum states, which makes it possible to perform quantum cloning. Since its proposition in 1996[216], quantum cloning has made much progress in DV and CV regimes[53,170,217–224]. In quantum cloning, fidelity is a significant index to measure the performance of quantum cloning. Therefore, how to effectively improve the fidelity of quantum cloning has become a critical issue to be addressed.

In the CV regime, an all-optical optimal $N \rightarrow M$ quantum cloning protocol based on a low-noise linear amplifier and optical BS was proposed theoretically[225,226]. The all-optical optimal $N \rightarrow M$ quantum cloning protocol can not only avoid the optic-electro and electro-optic conversion required in previous CV quantum cloning, but also significantly improve the fidelity of quantum cloning. Therefore, it is important to experimentally demonstrate all-optical optimal $N \rightarrow M$ quantum cloning. In a recent work, based on the low-noise amplifier in the previous subsection, Liu *et al.*[227] experimentally realized all-optical optimal $N \rightarrow M$ quantum cloning of coherent states by using a low-noise linear amplifier based on the FWM process and optical BS.

The detailed experimental setup is shown in Fig. 43. In the experiment, Liu *et al.* first prepared N original replicas in quantum cloning through the state preparation device (composed of a set of optical BSs). Then, they completed the energy concentration of the N original replicas through the energy concentration device (composed of a set of optical BSs). A low-noise OPA based on an FWM process was used to amplify the energy-concentrated state.

To complete the all-optical optimal $N \rightarrow M$ quantum cloning, the amplified state was equally divided into M clones. To characterize the performance of the quantum cloning machine, a series of HDs was used to measure the fidelity, which is defined as the overlap between the clone and the original replica. The fidelity of $N \rightarrow M$ quantum cloning can be given by

$$F = \frac{MN}{MN + M - N}. \tag{4}$$

To demonstrate the ability of all-optical optimal $N \rightarrow M$ quantum cloning in improving cloning fidelity, Liu *et al.* studied

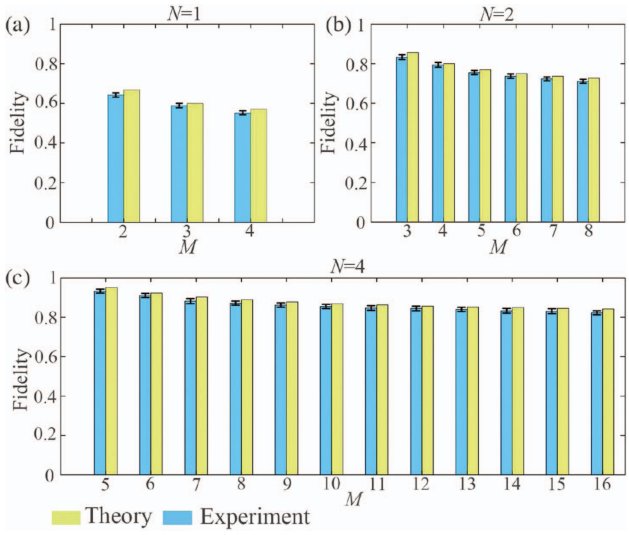

Fig. 44 Fidelities of the quantum cloning machine. Adapted from [227].

the effects of the original replica number N and the clone number M on fidelity in detail. The experimental results are shown in Fig. 44. They demonstrated that the fidelity of all-optical optimal $N \rightarrow M$ quantum cloning increased with the increase of the original replica number N and decrease of the clone number M. By changing the original replica number N and the clone number M, the maximum cloning fidelity achieved by them is about 93.3%. This work proves that the fidelity of quantum cloning can be effectively increased by utilizing all-optical optimal $N \rightarrow M$ quantum cloning.

3.5 All-Optical Quantum State Transfer Machine

The quantum information protocol aims to develop high-security, high-capacity information transmission and processing methods by utilizing the basic principles of quantum physics[1,2,228]. With the development of quantum information science, quantum information protocols with different functions have been proposed and experimentally implemented, such as quantum teleportation[182–199,229,230], QDC[70,231], quantum secret sharing[232], and quantum cloning[216–224]. The functions realized by these protocols cannot be realized in classical information systems.

Generally, a quantum information system can execute only one quantum information protocol. However, the quantum information task cannot remain unchanged. Therefore, the development of a multifunctional platform compatible with diverse quantum information protocols is important for the practical application of QIP. In a recent work, Lou *et al.*[233] realized a multifunctional all-optical quantum state transfer machine, which is composed of a gain adjustable OPA, an optical BS, and an EPR entanglement source. Such a machine can realize three all-optical quantum information protocols with different functions, including the AOQT protocol mentioned in the previous subsection, the partially disembodied quantum state transfer (PDQST) protocol, and the all-optical quantum cloning protocol.

As shown in Fig. 45, in the experiment, Lou *et al.* constructed a multifunctional all-optical quantum state transfer machine by using an adjustable gain OPA based on the FWM

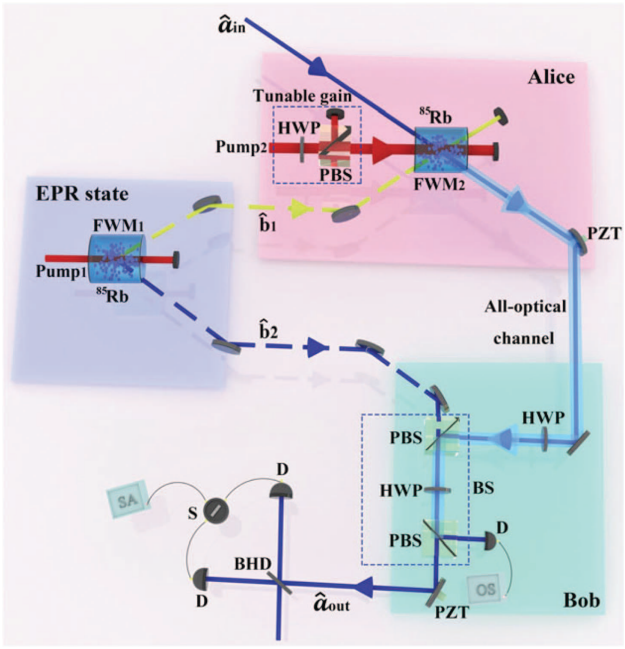

Fig. 45 Experimental layout. Adapted from [233].

process, a BS with an adjustable splitting ratio, and quantum entangled states. When the gain of the OPA is much greater than one, this machine executes the AOQT protocol. The fidelity of the output state is

$$F_{\mathrm{AOQT}} \approx \frac{1}{1+\left(\sqrt{H}-\sqrt{H-1}\right)^2}, \tag{5}$$

where H is the gain of the FWM process for generating EPR entangled beams. When the gain of the OPA does not meet the condition of being much greater than one, this machine executes the PDQST protocol. The fidelity of the corresponding output state is

$$F = \frac{1}{1+\frac{G-1}{G}\left(\sqrt{H}-\sqrt{H-1}\right)^2}, \tag{6}$$

where G is the tunable gain of the OPA. When the quantum entangled state is not used, this machine executes the all-optical quantum cloning protocol. The quantum cloning fidelity can be given by

$$F_{\mathrm{clone}} = \frac{G}{2G-1}. \tag{7}$$

The typical experimental results when $G = 2$ and $G = 16$ are shown in Fig. 46. In addition, Lou *et al.* experimentally proved the broadband characteristics of the multifunctional all-optical quantum state transfer, as shown in Figs. 46(c) and 46(f). It is able to realize quantum state transfer from 1 to 3.8 MHz. More importantly, they proved that under the same entanglement, compared with the AOQT protocol, the PDQST protocol can significantly improve the fidelity of quantum state transfer. As shown in Fig. 46(g), the fidelity of quantum state

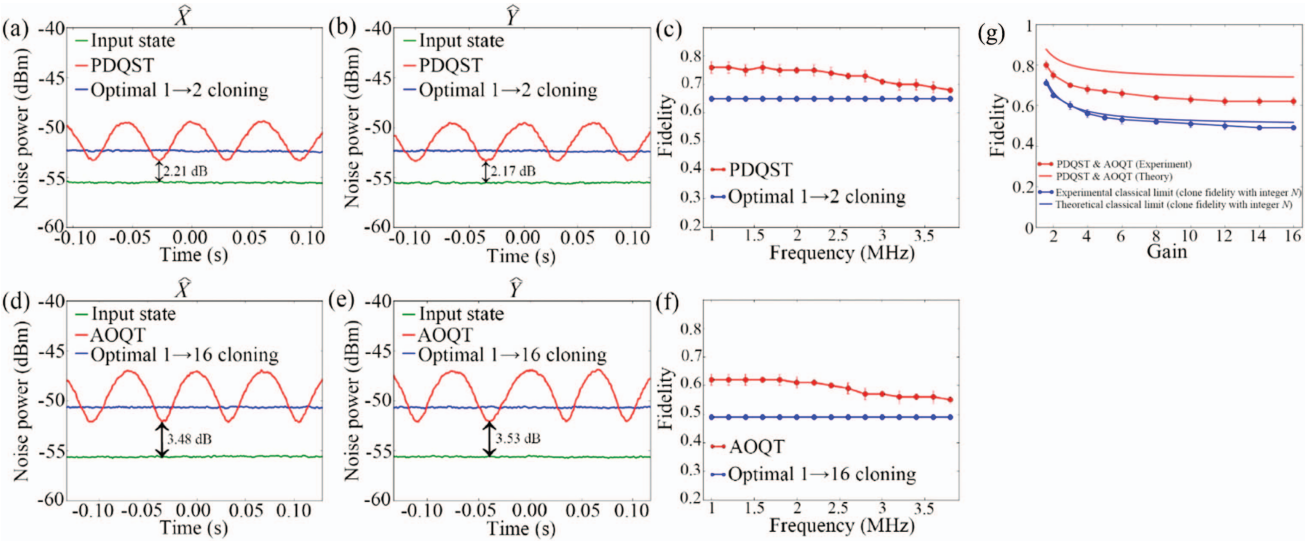

Fig. 46 (a)–(f) Experimental results when $G = 2$ and $G = 16$. (g) Fidelities versus G for all-optical quantum state transfer machine. Adapted from [233].

transfer is enhanced from 0.62 to 0.80. This work opens the way for the construction of a multifunctional CV quantum information system.

3.6 Orbital Angular Momentum Multiplexed Quantum Dense Coding

In the field of quantum information science, QDC is one of the most important protocols, which can double the channel capacity in principle. The QDC protocol was originally proposed and demonstrated in a DV system[231]. In this protocol, with the help of previously shared entangled pairs of qubits, the sender can transmit two bits of classical information to the receiver by sending only one qubit. Then, QDC was introduced in the CV system theoretically[234–237] and demonstrated experimentally using a pair of EPR beams[9,70,238]. Improving the channel capacity of quantum communication protocols has always been important. To make further progress in enhancing the channel capacity of QDC, different entanglement sources are utilized to exceed the channel capacity limit of conventional QDC. In the DV regime, Hu *et al*. implemented a superdense coding protocol by utilizing entangled ququarts, which can surpass the channel capacity limit of the QDC of entangled qubits[239]. In the CV regime, Shi *et al.* used a frequency multiplexed entanglement source to implement channel multiplexing quantum communication[240]. In a recent work, by utilizing OAM multiplexed bipartite entanglement (introduced in Section 2.4.2) as the quantum resource, Chen *et al.* experimentally implemented the OAM multiplexed QDC (MQDC) protocol, which surpasses the channel capacity of conventional QDC with fixed quantum resources[241].

The experimental layout is shown in Fig. 47(a). In this experiment, the injected probe beam is coded on LG_l mode (or $LG_l + LG_{-l}$ superposition mode) by the SLM. The EPR entangled source is generated by an FWM process in hot atomic ensembles, which is described in Subsection 2.4.2. After that, EPR1 is sent to Alice, who modulates classical signals on the amplitude quadrature and phase quadrature of EPR1 via

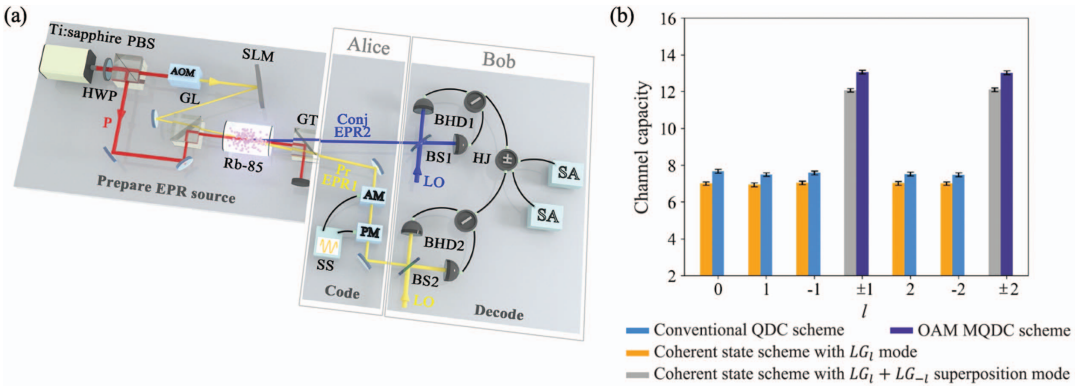

Fig. 47 (a) Experimental layout. OAM multiplexed bipartite entangled beams are utilized to implement the OAM MQDC protocol. Alice encodes classical signals on EPR1, and Bob decodes the signals by HDs. (b) Channel capacities of four schemes versus different topological charges l. Adapted from [241].

an amplitude modulator (AM) and a phase modulator (PM), respectively. After that, EPR1 is sent to Bob, where the classical signals are decoded with the help of EPR2 by HDs. When the pump of the FWM process used for generating an EPR entangled source is blocked, this process with coherent states can be seen as the classical counterpart of conventional QDC (or OAM MQDC).

The channel capacity of Gaussian quantum states can be expressed as[237]

$$C = \frac{1}{2}\log_2\left(1+\frac{S}{N}\right), \tag{8}$$

where S is the power of signal, N is the power of noise (variance), and the SNR $= S/N$. To fairly compare the channel capacities of four schemes, $\overline{n}$ (average photon number per bandwidth per second) in the channel needs to be fixed. $\overline{n}$ will be relevant to modulation power only if the power of modulation signals is much larger than one. Therefore, in the experiment, the power of modulation signals for different schemes is kept to about 21 dB to keep $\overline{n}$ fixed. To obtain the channel capacities of four different schemes (coherent state scheme with LG_l mode, coherent state scheme with $\mathrm{LG}_l + \mathrm{LG}_{-l}$ superposition mode, conventional QDC scheme, and OAM MQDC scheme), the SNRs of these schemes are acquired by the measured noise power spectra. The derived channel capacities of these four schemes are shown in Fig. 47(b).

As can be seen from Fig. 47(b), conventional QDC schemes slightly improve the channel capacities compared with coherent state schemes. OAM MQDC schemes show great improvement on channel capacity. Comparing the OAM MQDC scheme with the conventional coherent state scheme, a 2.7 dB enhancement of channel capacity can be observed, which is extremely difficult to achieve for conventional QDC. To reach such 3 dB level enhancement of channel capacity with the same quantum resource in this experiment, all four Bell states need to be deterministically discriminated for conventional DV QDC, or ultrahigh level squeezing needs to be generated for conventional CV QDC, both of which are very challenging in the experiment. Therefore, the OAM MQDC scheme has a great advantage in substantially improving the channel capacity for quantum information tasks.

In this section, different quantum information protocols are realized based on the FWM process in hot atomic ensembles. Based on these quantum information protocols, it is promising to construct a quantum communication network. In terms of practical applications, long-distance quantum communication in optical fiber or free space is necessary[24–26]. Therefore, applying these quantum information protocols to practical applications is a future research direction.

4 Applications in Quantum Metrology

Quantum metrology, an important field in quantum information, utilizes quantum squeezing to enhance measurement accuracy[242]. As an important quantum interferometer, the SU(1,1) interferometer is used in quantum metrology to surpass the classical limit[243]. Such an interferometer can be implemented by the cascaded FWM process or nonlinear crystal[244–246]. In this section, different properties of the SU(1,1) interferometer and its different applications in quantum metrology are introduced. The configuration of a truncated SU(1,1) interferometer is also introduced in this section. In addition, several works about quantum plasmonic sensing are introduced in the last subsection.

4.1 Quantum Enhancement of Phase Sensitivity and Degree of Entanglement Based on an SU(1,1) Interferometer

As the basis of metrology, optical interferometers have greatly contributed to precise phase measurement. Since the invention of the Michelson interferometer, phase-measurement accuracy has been largely improved[247]. Nevertheless, the phase sensitivity of traditional interferometers has a classical limit, which is called the SNL, $1/\sqrt{N_s}$, where N_s is the average photon number inside the interferometer[114,248].

The interferometer is generally composed of three parts: initial injection state, hardware structure, and detection scheme. Each part has a great influence on the performance of the interferometer. Therefore, based on these three parts, different schemes are proposed to make the measurement accuracy of the interferometer exceed the SNL[36,114,115,249–261]. In hardware structure, the SU(1,1) interferometer is able to be realized by using OPA to take the place of the BS in a Mach–Zehnder interferometer (MZI)[243]. Phase sensitivity estimates the uncertainty of the internal phase of the interferometer and is an important physical quantity to characterize the performance of the interferometer. In principle, the phase sensitivity of an SU(1,1) interferometer can be close to the Heisenberg limit (HL). In recent years, the phase sensitivity of SU(1,1) interferometers has been studied theoretically[262–264] and experimentally[127,265]. In a recent work, Liu *et al.* experimentally demonstrated the quantum enhancement of the phase sensitivity of a bright-seeded SU(1,1) interferometer by using direct intensity detection[266]. It is this direct intensity detection that allows them to measure the enhancement of phase sensitivity of a bright-seeded SU(1,1) interferometer in real time.

The schemes of MZI and the SU(1,1) interferometer are shown in Fig. 48. To compare the phase sensitivity of these two interferometers, N_s should be equal. The phase sensitivity of the interferometer can be given by

$$\Delta\phi^2 = \frac{\langle(\Delta\hat{O})^2\rangle}{|\partial\langle\hat{O}\rangle/\partial\phi|^2}, \tag{9}$$

where $\hat{O}$ consists of some combination of measurements of the output fields, and ϕ is the phase of the interferometer.

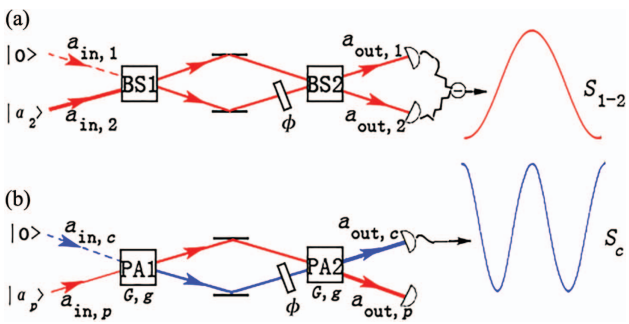

Fig. 48 Structure of MZI (a) and SU(1,1) interferometer (b). Adapted from [266].

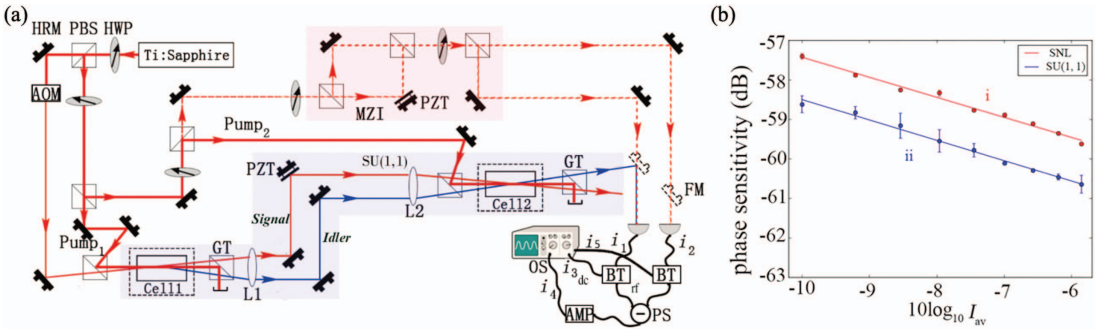

Fig. 49 (a) Detailed experimental setup of MZI and SU(1,1) interferometer. (b) Phase sensitivity of SU(1,1) interferometer and SNL varying with N_s. Adapted from [266].

In this sense, the sensitivity of MZI is given by $\Delta\phi_{\mathrm{MZI}} = 1/(|\sin\phi|\sqrt{N_s})$. The corresponding SNL is the minimum of $\Delta\phi_{\mathrm{MZI}}$, i.e., $\Delta\phi_{\mathrm{SNL}} = 1/\sqrt{N_s}$. Under the same N_s, the optimal phase sensitivity of the SU(1,1) interferometer can be expressed as

$$\Delta\phi_{c,\min} = \sqrt{\frac{G^2+g^2}{4G^2g^2}}\frac{1}{\sqrt{N_s}}, \tag{10}$$

where G^2 is the intensity gain of the parametric amplifier, and $g^2 = G^2 - 1$. It shows that the optimal phase sensitivity of the bright-seeded SU(1,1) interferometer is better than the corresponding SNL when $G^2 > 1.32$.

The detailed experimental layout is shown in Fig. 49(a). Liu *et al.* demonstrated that the phase sensitivity of a bright-seeded SU(1,1) interferometer can surpass its corresponding SNL by 1.15 ± 0.16 dB. The corresponding experimental results are shown in Fig. 49(b). This work made a major advance in the real-time quantum enhancement of bright-seeded SU(1,1) interferometers and may find potential applications in quantum-enhanced real-time phase tracking.

The structure of the SU(1,1) interferometer introduced above is also a cascaded FWM structure, which is a potential method to enhance the degree of entanglement. Entanglement enhancement has been implemented by a cascaded nondegenerate OPA system using nonlinear crystals in the cavities[267,268]. Xin *et al.* experimentally realized entanglement enhancement using the cascaded FWM process[269]. The cascaded FWM scheme is shown in Fig. 50(a).

By controlling the internal phase (ϕ), the noises of joint amplitude-quadrature-difference $\Delta\hat{X}_-^2$ and phase-quadrature-sum $\Delta\hat{Y}_+^2$ of the output fields can be manipulated. When $\phi = 2k\pi$, $\Delta\hat{X}_-^2$ and $\Delta\hat{Y}_+^2$ reach their minima. The typical noise power results of measured joint quadrature squeezing for cascaded FWM and single FWM are shown in Fig. 50(b). The noise power spectra are measured when the intensity gains of both FWM processes are 1.9. One can see that the maximal quadrature squeezing for the cascaded FWM scheme is about 6.6 dB and shows about 2.8 dB squeezing enhancement compared with the squeezing level generated by single FWM.

To obtain the maximal squeezing of the cascaded FWM scheme, they changed the intensity gain of the two FWM processes from 1.1 to 3.1 and made a series of measurements, as

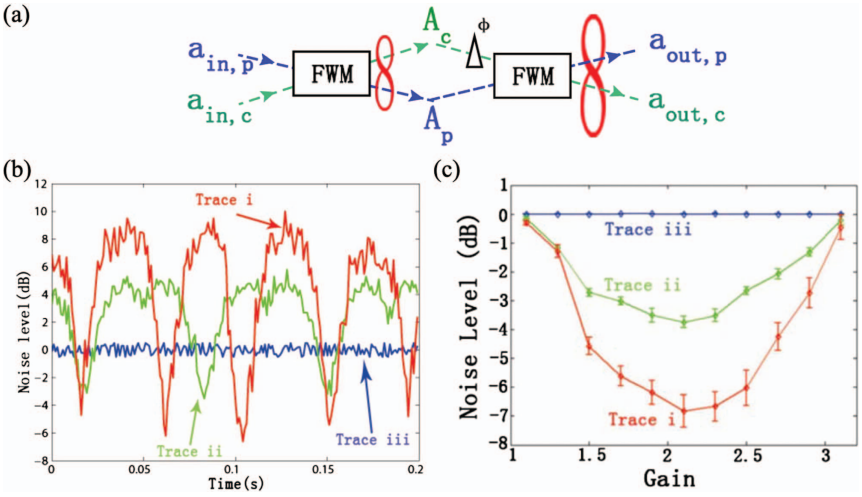

Fig. 50 (a) Cascaded FWM scheme. (b) Typical noise power spectra of measured joint quadrature squeezing. Trace i shows the noise power of $\hat{X}_-$ for cascaded FWM processes; trace ii shows the noise power of $\hat{X}_-$ for single FWM process; trace iii shows the corresponding SNL. (c) Measured quadrature squeezing versus the intensity gain of FWM processes. Adapted from [269].

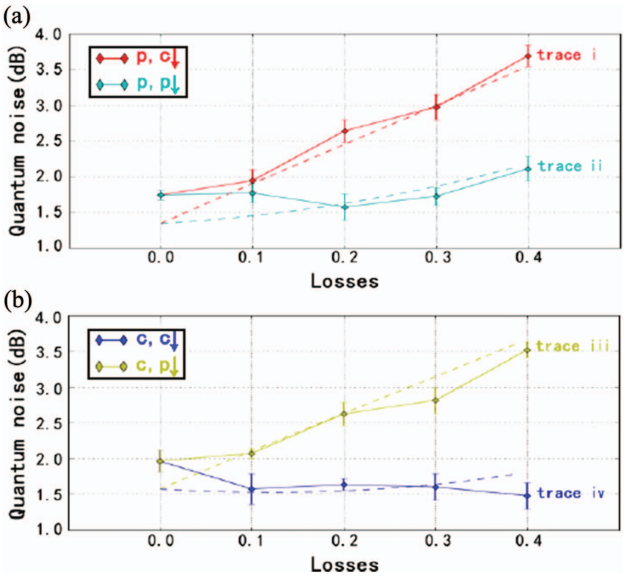

Fig. 51 Effect of losses on the QNC of the SU(1,1) interferometer. *p,c*↓ (*c,p*↓) is the losses case in probe (conjugate) field when attenuation acts on the conjugate (probe) arm of the SU(1,1) interferometer; *p,p*↓ (*c,c*↓) is the losses case in probe (conjugate) field when attenuation acts on the probe (conjugate) arm of the SU(1,1) interferometer. Adapted from [275].

shown in Fig. 50(c). Entanglement enhancement is observed as the intensity gain ranges from 1.1 to 3.1. The highest enhancement (3.1 dB) and the maximal quadrature squeezing (6.8 dB) are obtained with the intensity gain of 2.1. This work shows that the cascaded FWM scheme has the ability of entanglement enhancement.

4.2 Effect of Losses on the Performance of an SU(1,1) Interferometer

Quantum noise, the inherent property of the quantum system, plays an important role in quantum metrology. Therefore, controlling and reducing the quantum noise of the system has always been important. As a valid way to reduce quantum noise, quantum-noise cancellation (QNC) has been widely studied in many systems[36,270–272]. QNC was also observed by utilizing an SU(1,1) interferometer[124,126,273,274]. However, QNC is very sensitive to the internal losses of a quantum system. Xin *et al.* theoretically and experimentally studied how the losses affect QNC in the output fields of SU(1,1) interferometers[275]. They found that losses in different arms of the interferometer lead to a completely different impact on QNC of the output fields, and in some cases, QNC of the output fields can be almost insensitive to loss.

The amplitude-quadrature noises of the output fields of SU(1,1) with vacuum injections can be calculated as $\langle \Delta \hat{X}_p^2 \rangle = \langle \Delta \hat{X}_c^2 \rangle = 1 + 2G^2 g^2 (1 + \cos \phi)$, where G is the amplitude gain of the FWM process ($g^2 = G^2 - 1$), and ϕ is the internal phase shift. $\phi = \pi$, which is associated with destructive interference, results in the minimum noises of the output fields. Then, losses are introduced in different arms of the SU(1,1) interferometer. The experimental and theoretical results for the effect of losses on QNC are shown in Fig. 51.

They found that QNC is less sensitive to losses in conditions of $p, p\downarrow$ and $c, c\downarrow$ than in conditions of $p, c\downarrow$ and $c, p\downarrow$. $p, p\downarrow$ ($c, c\downarrow$) is the loss case in a probe (conjugate) field as attenuation acts on the probe (conjugate) arm of the SU(1,1) interferometer. $p, c\downarrow$ ($c, p\downarrow$) is the loss case in a probe (conjugate) field when attenuation acts on the conjugate (probe) arm of the SU(1,1) interferometer. In the case of $c, c\downarrow$, QNC is almost insensitive to loss. The results in this work are promising for potential applications in quantum metrology.

As mentioned in Subsection 4.1, phase sensitivity is an important physical quantity for characterizing the performance of an SU(1,1) interferometer. Such performance will be affected by the losses of the interferometer. Marino *et al.* made a comprehensive analysis of the effect of losses on the phase sensitivity of an SU(1,1) interferometer[125]. Analyses of the effect of internal losses and external losses of SU(1,1) interferometers with direct detection were both studied in their work.

Although external loss, such as imperfect detection efficiency, can be a problem for the performance of MZI, the SU(1,1) interferometer is robust against such external loss[276,277]. However, its phase sensitivity is sensitive to internal loss. When an SU(1,1) interferometer is injected with two vacuum fields or only one coherent input, a small deviation from $\phi = 0$ creates a large decrease in phase sensitivity for the ideal case, which can be seen in the blue dashed trace in Fig. 52(a). Therefore, any internal loss of the SU(1,1) interferometer will make it impossible for phase sensitivity to reach the HL or even surpass the SQL. When an SU(1,1) interferometer is injected by two coherent states, the effect of internal loss $(1 - \eta_1)$ on the phase sensitivity of the SU(1,1) interferometer is shown in Fig. 52(b). For a small internal loss, the phase uncertainty of the interferometer can still be close to the HL with a limit range of n_i and can still beat the SQL when the internal loss is approaching 50%. Their work provides a comprehensive analysis of the effect of losses on the phase sensitivity of an SU(1,1) interferometer.

4.3 Truncated SU(1,1) Interferometer

In addition to the above studies of conventional SU(1,1) interferometers, a variation of an SU(1,1) interferometer with one nonlinear process is also useful for applications in quantum metrology. Such a truncated SU(1,1) interferometer that can be utilized for phase sensing was theoretically studied and experimentally implemented by Anderson *et al.*[127].

The configurations of a conventional SU(1,1) interferometer with four measurement schemes are shown in Fig. 53(a). Figure 53(b) shows the configuration of a truncated SU(1,1) interferometer. This interferometer is realized by the replacement of the second nonlinear process of an SU(1,1) interferometer with two HDs. Theoretical predictions for the phase sensitivities of a conventional SU(1,1) interferometer and a truncated SU(1,1) interferometer versus intensity gain are shown in Fig. 53(c). These results show that, for a lossless case, the phase sensitivity of a truncated SU(1,1) interferometer is almost equivalent to the conventional SU(1,1) interferometer with measurement scheme (i) shown in Fig. 53(a)[127,263]. For experimental implementation of the truncated interferometer, optimal phase sensing can be obtained when both HDs measure the phase quadrature of the outputs of the FWM process. To evaluate phase sensitivity experimentally, they measured the SNR as shown in Fig. 53(d). Compared with the SNR measured by

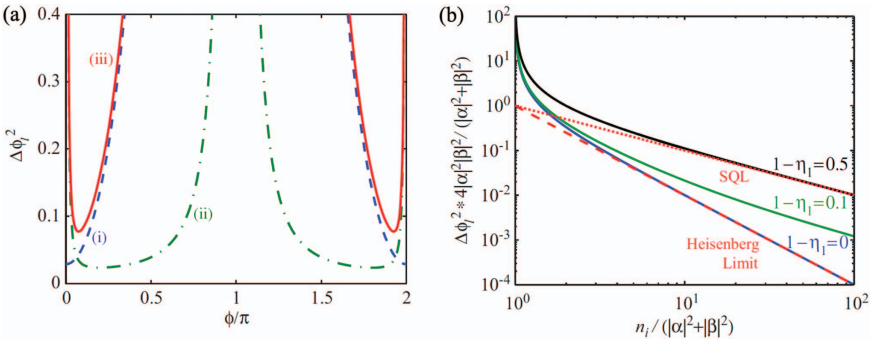

Fig. 52 Uncertainty of the phase estimation with internal loss for the SU(1,1) interferometer injected with vacuum fields (a) and coherent fields (b). Trace (i) shows the uncertainty in the lossless case. Trace (ii) shows the contribution from the internal losses. Trace (iii) shows the uncertainty with internal losses ($1 - \eta_1 = 0.1$). Adapted from [125].

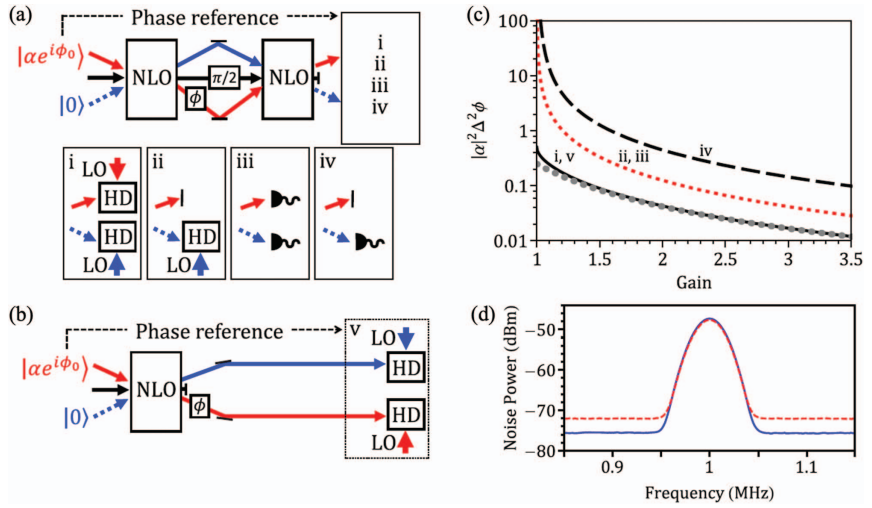

Fig. 53 Configurations of conventional SU(1,1) interferometer and truncated SU(1,1) interferometer are shown in (a) and (b), respectively. i, ii, iii, and iv show different measurement schemes for SU(1,1) interferometer. NLO, nonlinear optical medium; HD, homodyne detector. (c) Theoretical results of the variance of the phase estimation versus gain in lossless case. (d) Measured SNR for truncated SU(1,1) interferometer (blue solid trace) and corresponding coherent scheme (red dashed trace). Adapted from [127].

the corresponding classical scheme where the nonlinear optical medium (NLO) is absent (red dashed trace), the SNR of the truncated SU(1,1) interferometer (blue solid trace) can be increased by 4 dB.

Based on previous work on the truncated SU(1,1) interferometer, Gupta *et al.* took loss into consideration and theoretically analyzed the phase sensitivity of a truncated SU(1,1) interferometer with loss[278]. In addition, they theoretically and experimentally studied the optimized measurement for the truncated SU(1,1) interferometer.

The configuration of the truncated SU(1,1) interferometer's considered loss is shown in Fig. 54. The optimal sensitivity can be obtained with both HDs locked to measure the phase quadrature. The joint phase sum quadrature is given by $\hat{M}_Q = \hat{Y}_p + \hat{Y}_c$, where $\hat{Y}_p$ ($\hat{Y}_c$) is the phase quadrature of the output probe (conjugate) beam. Different from the measurement of balanced observable $\hat{M}_Q$ in previous work, the measurement of weighted observable $\hat{M}_{\lambda Q} = \hat{Y}_p + \lambda \hat{Y}_c$ is able to further enhance the phase sensitivity in this work. $\hat{M}_{\lambda Q}$ can be obtained by electronically attenuating the HD's output in experiment. For a lossless case, the theoretical noise power of $\hat{M}_{\lambda Q}$ versus the attenuation factor λ is shown in Fig. 55(a). The noise of $\hat{M}_{\lambda Q}$ reaches the minimum with an optimal factor λ_{opt}, which also corresponds to optimal phase sensitivity. λ_{opt} increases as the gain increases. For the truncated SU(1,1) interferometer with propagation loss, λ_{opt} can be calculated as $\lambda_{\text{opt}} = (\sqrt{\eta_p}\sqrt{\eta_c}\sinh 2r)/(1 - \eta_c + \eta_c \cosh 2r)$, where η_c (η_p) is the transmission of the conjugate (probe) beam. The effect of the transmission on λ_{opt} is shown in Fig. 55(b). Gupta *et al.* also implemented the truncated SU(1,1) interferometer experimentally based on FWM and demonstrated a noise reduction of $\hat{M}_{\lambda Q}$. The experimental results of the noise power of $\hat{M}_{\lambda Q}$ versus λ are shown in Fig. 55(c). The experimental results of λ_{opt} versus FWM gain are shown in Fig. 55(d). These results, providing an optimized homodyne measurement, are promising to further enhance the measured phase sensitivity.

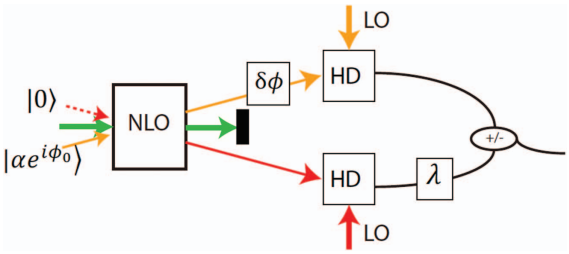

Fig. 54 Schematic for the truncated SU(1,1) interferometer. λ is the attenuation factor. Adapted from [278].

4.4 Ultrasensitive Measurement of Microcantilever Displacement

In addition to improving phase sensitivity, the enhancement of displacement measurement sensitivity is also an important task in quantum metrology. An optical beam is widely used as the readout for displacement measurement in micro-mechanical sensors, nano-mechanical sensors, and force microscopes[279–281]. Displaying quantum-enhanced statistics, squeezed light plays an important role in enhancing the displacement measurement sensitivity beyond the SNL[282]. Pooser *et al.* implemented ultrasensitive measurement of microcantilever displacement below the SNL using a two-mode squeezed state generated by FWM[40]. As shown in Fig. 56, the squeezed light source is generated by FWM in a hot Rb vapor cell, and then the probe beam is focused into the cantilever by a microscope objective. The returned probe beam and the conjugate beam are sent to a split detector, which can subtract the noises between the correlated parts of each beam.

The measurement results for ultrasensitive displacement measurement are shown in Fig. 57. Figure 57(a) shows the measured SNR versus the displacement amplitude. With about a 3 dB squeezing level, the SNR is largely improved compared with the SNR of the coherent state scheme. The noise power for split detector measurements versus optical power is shown in Fig. 57(b). The minimum measurable displacement can be calculated by the measured SNR and noise floor, which is shown in Fig. 57(c). The measured displacement noise is between 2.5 and 2.8 dB below the classical limit. Their work implemented the microcantilever beam deflection below the classical limit based on FWM and may find applications in other cantilever devices.

To enhance displacement measurement sensitivity, Pooser *et al.* also implemented a quantum-enhanced atomic force microscopy (AFM) microcantilever utilizing the truncated nonlinear interferometer introduced above[128,283,284].

As shown in Fig. 58, the correlated beams and their corresponding LO beams are generated by the FWM process. Either the probe beam or its LO beam can be used to implement displacement measurement. Figures 59(a) and 59(b) [Figs. 59(c) and 59(d)] show the measurement results when the probe beam (corresponding LO beam) is reflected from the AFM microcantilever. It can be found that the quantum noise is reduced up to 3 dB, shown in Fig. 59(c), which corresponds to a quantum enhanced displacement measurement of $1.7\,\mathrm{fm}/\sqrt{\mathrm{Hz}}$. Their scheme is a promising candidate for the implementation of broadband and high-speed scanning probe microscopy.

4.5 Quantum Plasmonic Sensing

Quantum plasmonics has received more attention because of the increasing applications in plasmonics from nanoimaging[285] to subwavelength photonic circuits[286]. The sensitivity for plasmonic biosensors based on extraordinary optical transmission (EOT) can be greatly enhanced if squeezed light can be

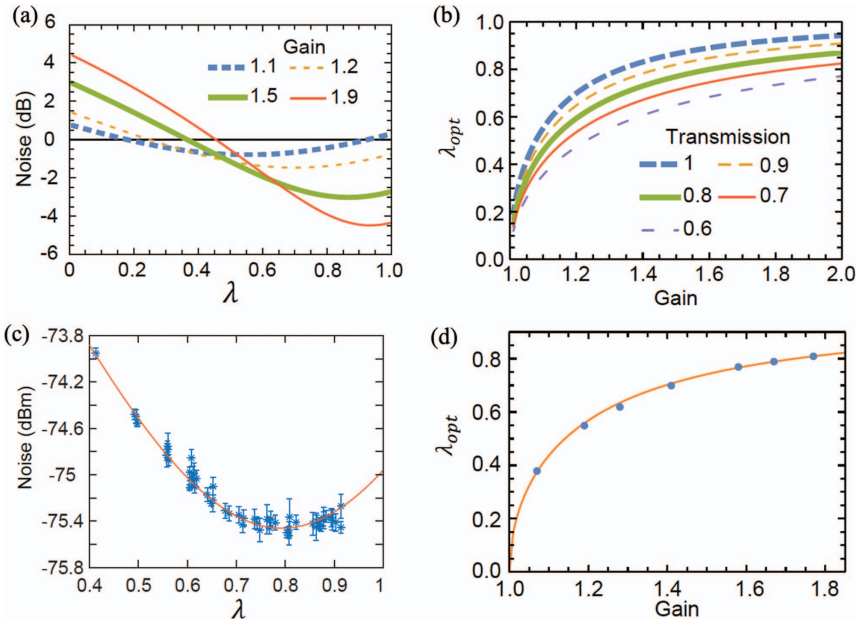

Fig. 55 (a) Theoretical noise power of $\hat{M}_{\lambda Q}$ versus the attenuation factor λ at different gains. (b) λ_{opt} versus the intensity gain of FWM process at different optical transmissions ($\eta_c = \eta_p$). (c) Experimental results of the noise power of $\hat{M}_{\lambda Q}$ versus the attenuation factor λ with an FWM gain of 1.67 in the case of 79% conjugate transmission and 76% probe transmission. (d) Experimental results of λ_{opt} versus FWM gain. Adapted from [278].

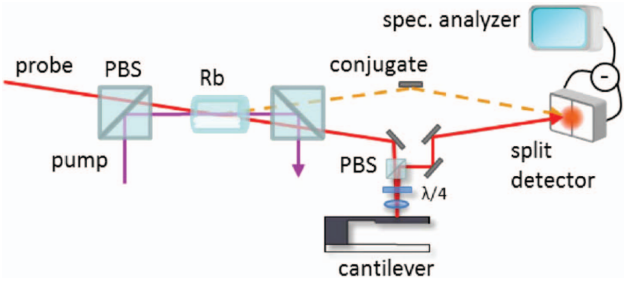

Fig. 56 Setup for ultrasensitive measurement of microcantilever displacement. Adapted from [40].

coherently coupled through subwavelength hole arrays[287,288]. In plasmonic systems, the wave vector independence of localized surface plasmon (LSP) decay makes LSPs a workbench for quantum information and quantum nanoimaging[288]. Based on LSPs, Lawrie *et al.* demonstrated the transduction of a squeezed state through EOT media[121].

The experimental layout is shown in Fig. 60(a). The probe beam passes through an SLM and injected into a Rb vapor cell. Then, the squeezed light source is generated by the FWM process. The probe beam passes through the EOT heterostructure, and the conjugate beam passes through an ND filter. The existence of squeezing after EOT is shown in Fig. 60(c), demonstrating that quantum information can be transduced by LSPs.

For surface plasmon resonance (SPR) sensors[289,290], although such sensors have high sensitivity because of nanoscale electric-field confinement, the sensitivity of SPR sensors is still limited by SNL. As introduced above, it has been demonstrated that LSPs can coherently transduce squeezed states[121], which shows the potential of quantum plasmonic sensors for beating the SNL. In this work, Fan *et al.* implemented 5 dB sensitivity improvement of SPR sensors utilizing squeezed light sources[118].

As shown in Fig. 61(a), after the squeezed light source is generated by the FWM process, the probe beam is sent to the prism coupling system and used as the optical transducer. The conjugate beam is sent to the balanced photodetector directly. The measured squeezing level as a function of the reflectivity (incident angle) of the SPR sensor is shown in Fig. 61(b) [Fig. 61(c)]. The noise floor at higher reflectivity is suppressed because of quantum squeezing. The noise at lower reflectivity is increased because of the uncorrelated quantum noise between the two quantum correlated beams caused by attenuation of the probe beam. Compared with 6.4 dB absorption depth obtained by using a single coherent light source, 11.4 dB absorption depth is obtained by using squeezed light, which shows a 5 dB enhancement in the sensitivity of the SPR sensor.

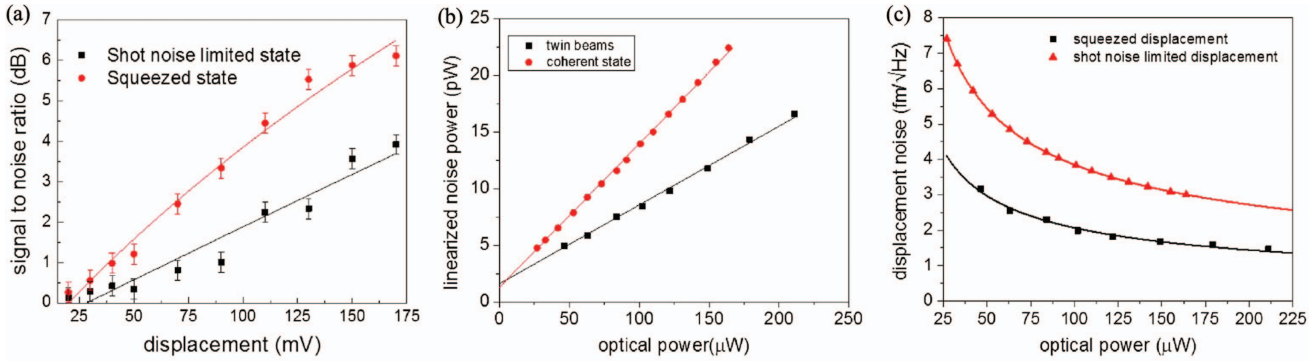

Fig. 57 Measurement results for sub-shot-noise microcantilever deflection detection. Adapted from [40].

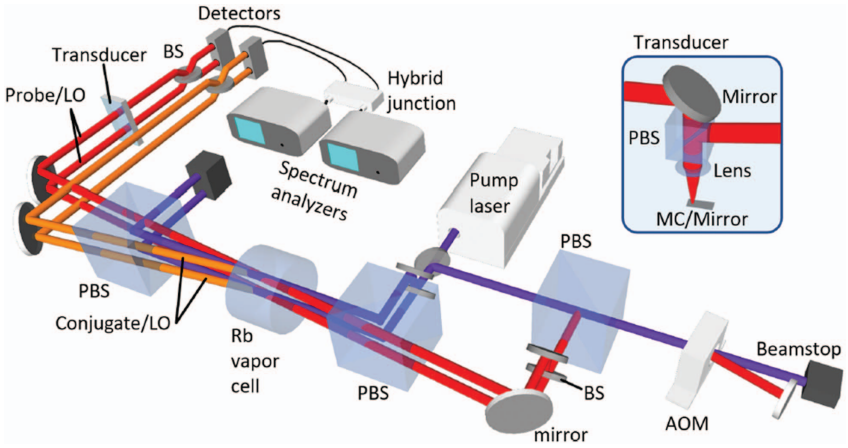

Fig. 58 Experimental setup. MC, microcantilever. Adapted from [128].

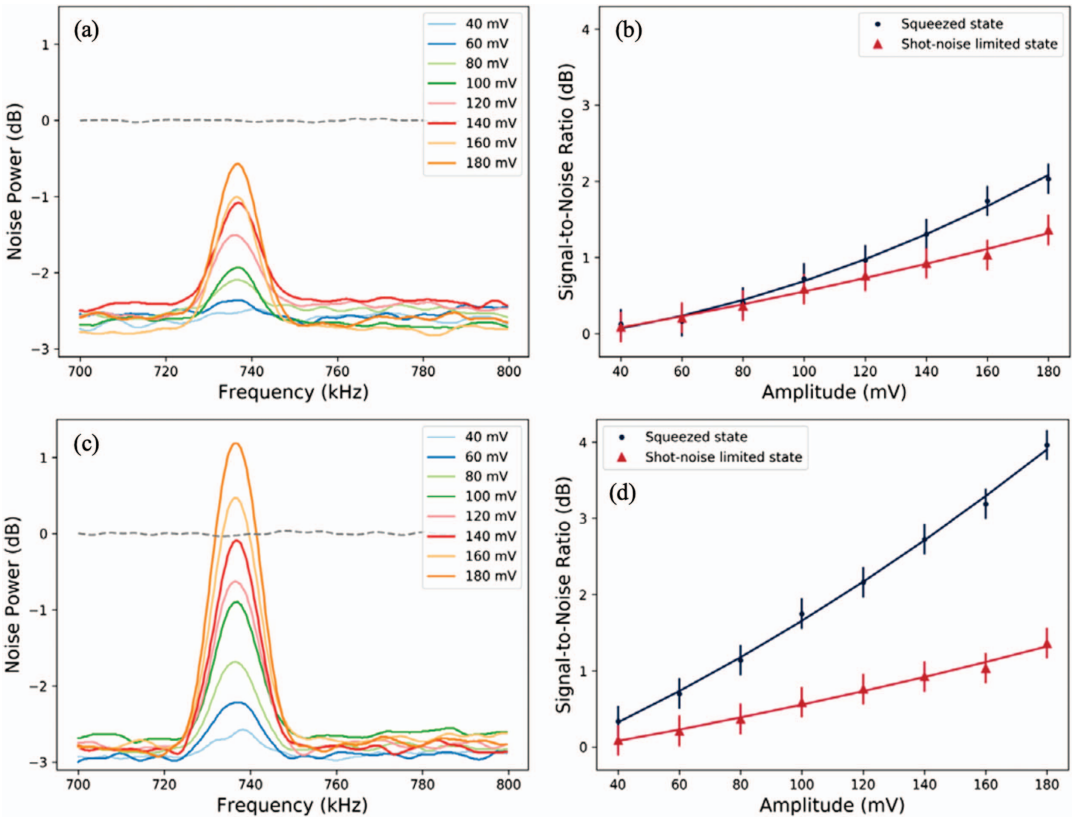

Fig. 59 (a) Traces of microcantilever displacement when a weak probe is reflected from the microcantilever. Different lines correspond to different voltages of PZT on the AFM microcantilever. (b) SNR of the corresponding scheme. (c) Traces of microcantilever displacement when high-power LO beam is reflected from the microcantilever. (d) SNR of the corresponding scheme. Adapted from [128].

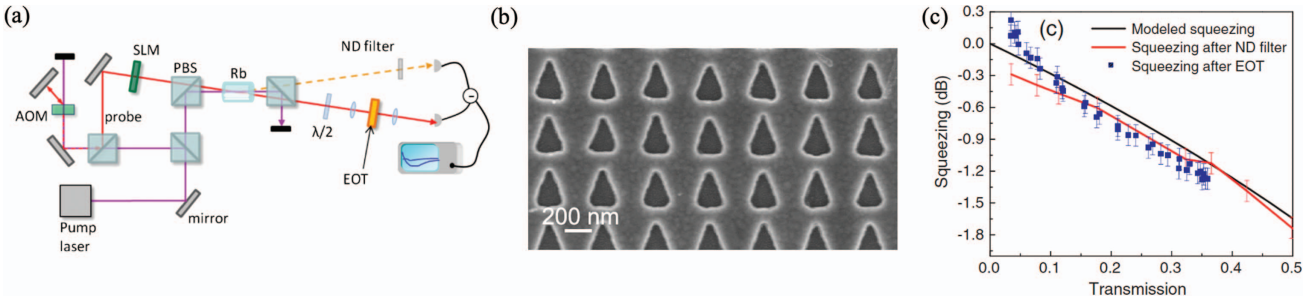

Fig. 60 (a) Experimental setup for the transduction of a squeezed state through an EOT medium. ND is a neutral density filter used to balance the classical intensity noise. (b) Scanning electron microscope image of triangle hole array of LSPs. (c) Measured squeezing levels versus transmissions. Adapted from [121].

Their work experimentally demonstrates the sensitivity enhancement of SPR sensors.

Based on the above work, using two-mode squeezed light as the optical readout for a plasmonic sensor, Pooser *et al.* increased the sensitivity compared with the corresponding sensor using coherent light[119]. The experimental layout for sub-SNL plasmonic sensing is shown in Fig. 62(a). A two-mode squeezed light source is generated by the FWM process. The probe beam goes through an AOM, which is used to modulate the probe field. Then, the modulated probe beam is sent to the prism and the refracted beam is sent to the detector. If there is a change in the concentration of the analyte, the change of the index of refraction will cause a resonance shift. Such measurement precision of the angular shift can be enhanced by using a squeezed light source. Figure 62(b) shows the height of the modulation peaks. Figure 62(c) shows the quantum noise reduction for each point. The lower noise floor of squeezed light leads to a better SNR and better sensitivity. The index shift of 0.001 can be measured in their work, showing the ability of a squeezed light source based on the FWM process to enhance the sensitivity of plasmonic sensors.

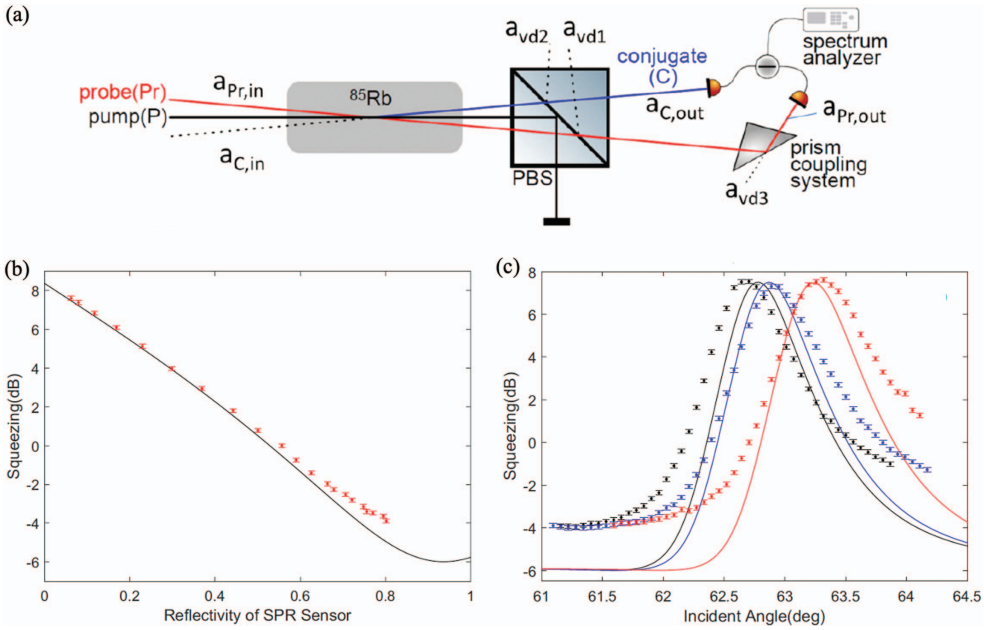

Fig. 61 (a) Experimental setup. (b) Measured squeezing versus the reflectivity of the SPR sensor. (c) Measured squeezing versus the incident angle of the SPR sensor. Black, blue, and red lines represent squeezing with a refractive index of 1.3, 1.301, and 1.305, respectively. Adapted from [118].

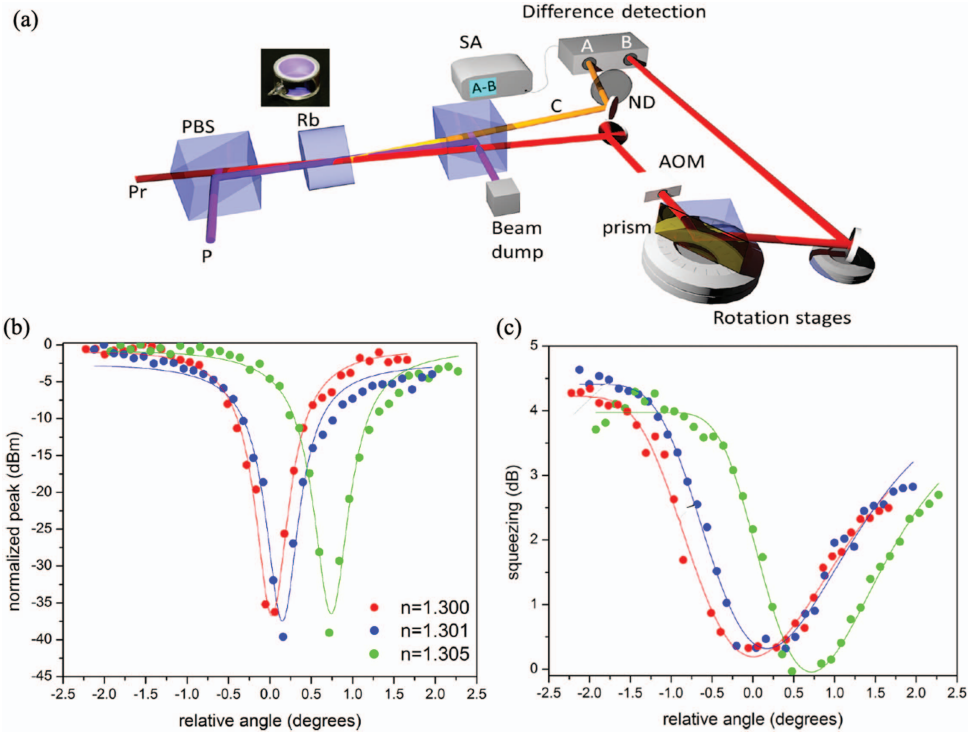

Fig. 62 (a) Experimental setup. (b) Plasmonic resonance versus relative incidence angle and refractive index. (c) Quantum noise reduction versus incidence angle and refractive index. Adapted from [119].

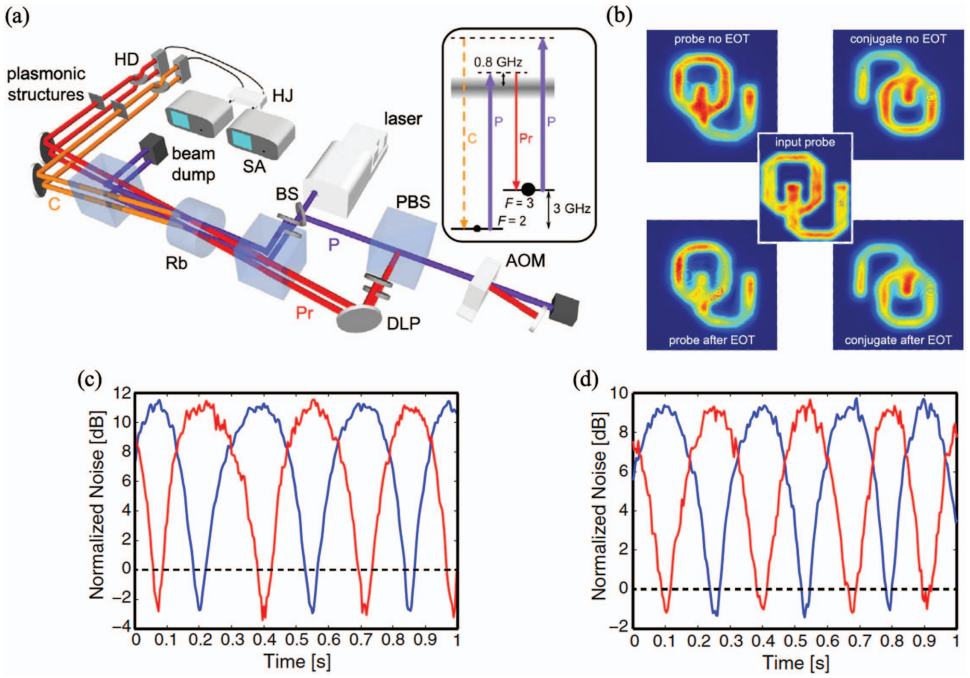

Fig. 63 (a) Experimental setup. DLP, digital light processor; HJ, hybrid junction for simultaneously adding and subtracting the two signals. (b) Effect of EOT on spatial images coded on the correlated beams. Normalized noise of the amplitude-quadrature sum (blue trace) and phase-quadrature difference (red trace) of the entangled beams (c) before and (d) after the plasmonic films. Adapted from [122].

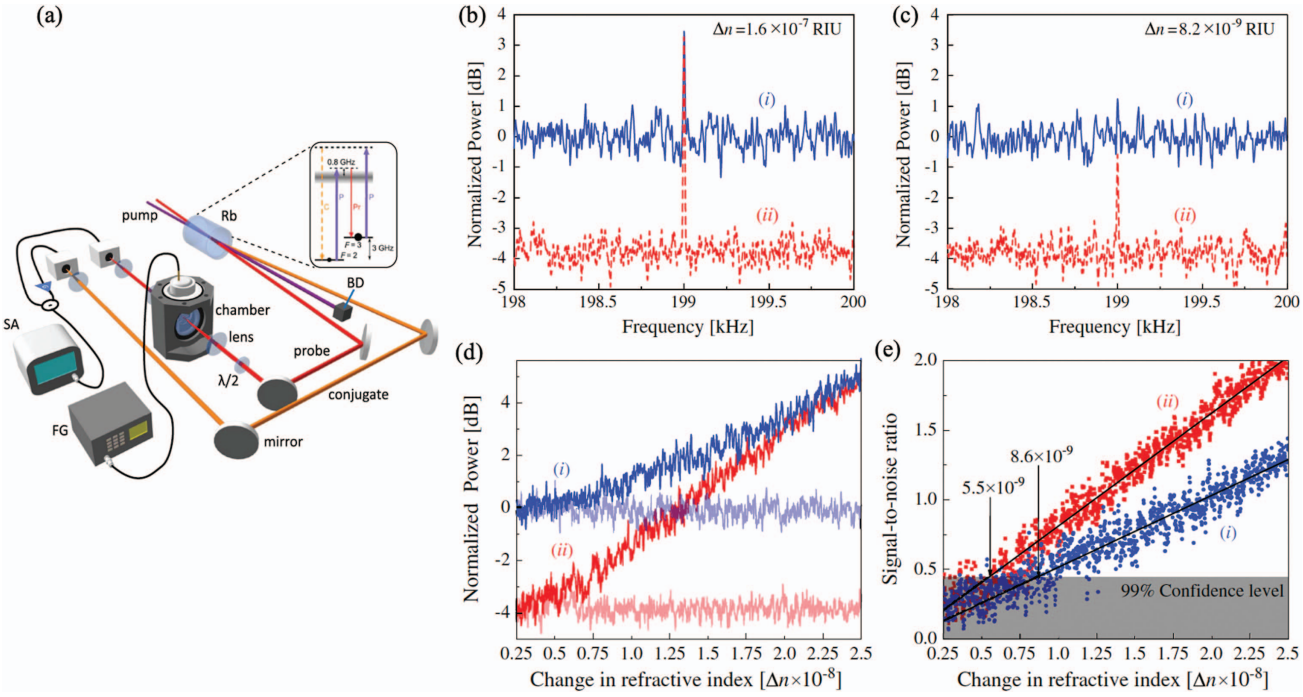

Fig. 64 (a) Experimental setup. (b) Measured power spectra for probing the sensor with coherent states and twin beams with $\Delta n = 1.6 \times 10^{-7}$ refractive index unit (RIU). (c) Measured power spectra with $\Delta n = 8.2 \times 10^{-9}$ RIU. (d) Normalized power versus the change in refractive index. (e) SNRs measured by probing the plasmonic sensor with coherent states (i) and with twin beams (ii). Adapted from [120].

After research on the interaction between quantum states of light and LSPs or SPR sensors[117–119,121,291–295], Holtfrerich *et al.* demonstrated multi-spatial-mode CV entanglement transduction through independent plasmonic media[122]. Such an implementation that transfers entanglement from light to separate plasmons and back to light is a crucial step towards a CV quantum plasmonic network.

As shown in Fig. 63(a), the probe beam is sent to a digital light processor (DLP), which can encode the spatial profile of a probe beam. Then, the probe beam is sent to the vapor cell, where entangled images are generated by the FWM process. After that, the images go through two independent plasmonic structures. The effect of plasmonic structures on the spatial distribution of entangled images is shown in Fig. 63(b). The bottom row in Fig. 63(b) shows that the nanostructure does not degrade images obviously and the spatial information is preserved. Figure 63(c) [Fig. 63(d)] is the noise power of the joint quadrature of entangled beams before (after) the EOT process. The −1.1 dB squeezing shown in Fig. 63(d) demonstrates that quantum entanglement is preserved by the transfer from photons to plasmons and back to photons. Their work first demonstrated the transduction of CV entangled images through plasmonic structures.

The sensitivity of plasmonic sensors was further enhanced by ulilizing the quantum state of light by Dowran *et al.*[120]. Sensitive detection of the air refractive index variation caused by ultrasonic waves can be extended to practical applications. As shown in Fig. 64(a), entangled twin beams are generated by the FWM process. The probe beam is sent to the SPR sensor. When there is a small change in the local refractive index, the SPR sensor will exhibit a frequency shift and a change in optical transmission. The plasmonic sensor is placed in a hermetically sealed chamber to study the response of the sensor. Modulation of the air refractive index is introduced by an ultrasonic transducer. The noise reduction properties of the squeezed light readout lead to a better SNR and better sensitivity.

The measured noise power of the modulation signal is shown in Figs. 64(b) and 64(c). For modulation of $\Delta n = 1.6\times 10^{-7}$ RIU [shown in Fig. 64(b)], a 4 dB enhancement of SNR can be obtained by using entangled twin beams, providing the ability to resolve smaller modulations. As shown in Fig. 64(c), modulation of $\Delta n = 8.2 \times 10^{-9}$ RIU can be observed only with entangled twin beams. The measured noise power versus the change in refractive index is shown in Fig. 64(d). Figure 64(e) shows the calculated SNR based on the results of Fig. 64(d). A 56% quantum enhancement is obtained in their results. This quantum-enhanced plasmonic sensing may have potential applications in biomedical and chemical detection.

So far, these works are limited to using two-beam quantum correlation to enhance measurement precision. A future direction is utilizing multiple-beam and multiplexed quantum correlation generated by the FWM process in hot atomic ensembles to realize distributed[130,131], multi-parameter[296], and multi-channel quantum sensing[297].

5 Conclusion

We have reviewed the recent progress on the generation of optical quantum states based on the FWM process in hot atomic ensembles, including the generation of two-beam quantum correlation, multi-beam quantum correlation, and OAM multiplexed quantum correlation. These results clearly show that the FWM process is a promising way to generate high-capacity and high-squeezing-degree optical quantum states. More importantly, we have reviewed the applications of such optical quantum states in the quantum information protocol and quantum metrology.

In the quantum information protocol, we discussed the implementation of OAM multiplexed AOQT, AOES, low-noise amplification of quantum states, all-optical optimal N-to-M quantum cloning, all-optical quantum state transfer machine, and OAM MQDC. These results demonstrate that the FWM process in hot atomic ensembles is very useful for implementing all-optical quantum information protocols, and paves the way for the construction of multifunctional all-optical quantum information systems and all-optical broadband quantum networks.

In quantum metrology, we reviewed the applications and properties of SU(1,1) interferometers and quantum sensing based on FWM processes, including quantum enhancement of phase sensitivity, enhancement of entanglement, the effect of losses on QNC, and quantum plasmonic sensing. These works show that the SU(1,1) interferometer can achieve more precise measurement, and may have applications in improving the sensitivity of various measurement systems. Moreover, these results show that optical quantum states generated from FWM processes can be widely used in various quantum sensing tasks.

The FWM process in hot atomic ensembles is still developing and finding new applications. For instance, the optical quantum state generated by the FWM process in hot atomic ensembles will have a larger scale by involving different DOFs, such as time and frequency. With the increase of the scale of the generated optical quantum state, the FWM process in hot atomic ensembles can be used to build complex quantum networks and implement multi-parameter quantum metrology.

Acknowledgments

This work was supported by the Innovation Program of Shanghai Municipal Education Commission (2021-01-07-00-08-E00100), National Natural Science Foundation of China (11874155, 91436211, 11374104, 12174110), Basic Research Project of Shanghai Science and Technology Commission (20JC1416100), Natural Science Foundation of Shanghai (17ZR1442900), Minhang Leading Talents (201971), Program of Scientific and Technological Innovation of Shanghai (17JC1400401), Shanghai Sailing Program (21YF1410800), China Post-doctoral Science Foundation (2020M681224), National Basic Research Program of China (2016YFA0302103), Shanghai Municipal Science and Technology Major Project (2019SHZDZX01), and 111 Project (B12024).

References

1. J. -W. Pan *et al.*, "Multiphoton entanglement and interferometry," *Rev. Mod. Phys.* **84**, 777 (2012).
2. S. L. Braunstein and P. van Loock, "Quantum information with continuous variables," *Rev. Mod. Phys.* **77**, 513 (2005).
3. P. G. Kwiat *et al.*, "New high-intensity source of polarization-entangled photon pairs," *Phys. Rev. Lett.* **75**, 4337 (1995).
4. A. MacRae *et al.*, "Tomography of a high-purity narrowband photon from a transient atomic collective excitation," *Phys. Rev. Lett.* **109**, 033601 (2012).
5. Z. Qin *et al.*, "Complete temporal characterization of a single photon," *Light Sci. Appl.* **4**, e298 (2015).
6. M. H. Devoret and R. J. Schoelkopf, "Superconducting circuits for quantum information: an outlook," *Science* **339**, 1169 (2013).

7. M. Kjaergaard *et al.*, "Superconducting qubits: current state of play," *Annu. Rev. Condens. Matter Phys.* **11**, 369 (2020).
8. C. Silberhorn *et al.*, "Generation of continuous variable Einstein-Podolsky-Rosen entanglement via the Kerr nonlinearity in an optical fiber," *Phys. Rev. Lett.* **86**, 4267 (2001).
9. J. Jing *et al.*, "Experimental demonstration of tripartite entanglement and controlled dense coding for continuous variables," *Phys. Rev. Lett.* **90**, 167903 (2003).
10. C. Fabre and N. Treps, "Modes and states in quantum optics," *Rev. Mod. Phys.* **92**, 035005 (2020).
11. C. Eichler *et al.*, "Observation of two-mode squeezing in the microwave frequency domain," *Phys. Rev. Lett.* **107**, 113601 (2011).
12. H. Zhong *et al.*, "12-Photon entanglement and scalable scattershot boson sampling with optimal entangled-photon pairs from parametric down-conversion," *Phys. Rev. Lett.* **121**, 250505 (2018).
13. Y. Huang *et al.*, "Experimental generation of an eight-photon Greenberger-Horne-Zeilinger state," *Nat. Commun.* **2**, 546 (2011).
14. C. Reimer *et al.*, "Generation of multiphoton entangled quantum states by means of integrated frequency combs," *Science* **351**, 1176 (2016).
15. A. Mair *et al.*, "Entanglement of the orbital angular momentum states of photons," *Nature* **412**, 313 (2001).
16. A. C. Data *et al.*, "Experimental high-dimensional two-photon entanglement and violations of generalized Bell inequalities," *Nat. Phys.* **7**, 677 (2011).
17. M. Malik *et al.*, "Multi-photon entanglement in high dimensions," *Nat. Photon.* **10**, 248 (2016).
18. D. Ding *et al.*, "High-dimensional entanglement between distant atomic-ensemble memories," *Light Sci. Appl.* **5**, e16157 (2016).
19. M. Kues *et al.*, "On-chip generation of high-dimensional entangled quantum states and their coherent control," *Nature* **546**, 622 (2017).
20. Y. Zhang *et al.*, "Engineering two-photon high-dimensional states through quantum interference," *Sci. Adv.* **2**, e1501165 (2016).
21. X. Wang *et al.*, "18-Qubit entanglement with six photons' three degrees of freedom," *Phys. Rev. Lett.* **120**, 260502 (2018).
22. W. Zhang *et al.*, "Experimental realization of entanglement in multiple degrees of freedom between two quantum memories," *Nat. Commun.* **7**, 13514 (2016).
23. C. Reimer *et al.*, "High-dimensional one-way quantum processing implemented on *d*-level cluster states," *Nat. Phys.* **15**, 148 (2019).
24. S. Liao *et al.*, "Satellite-to-ground quantum key distribution," *Nature* **549**, 43 (2017).
25. J. Yin *et al.*, "Satellite-based entanglement distribution over 1200 kilometers," *Science* **356**, 1140 (2017).
26. J. Yin *et al.*, "Entanglement-based secure quantum cryptography over 1,120 kilometers," *Nature* **582**, 501 (2020).
27. W. Asavanant *et al.*, "Generation of time-domain-multiplexed two-dimensional cluster state," *Science* **366**, 373 (2019).
28. M. V. Larsen *et al.*, "Deterministic generation of a two-dimensional cluster state," *Science* **366**, 369 (2019).
29. X. Pan *et al.*, "Orbital-angular-momentum multiplexed continuous-variable entanglement from four-wave mixing in hot atomic vapor," *Phys. Rev. Lett.* **123**, 070506 (2019).
30. U. L. Andersen *et al.*, "Hybrid discrete- and continuous-variable quantum information," *Nat. Phys.* **11**, 713 (2015).
31. R. E. Slusher *et al.*, "Observation of squeezed states generated by four-wave mixing in an optical cavity," *Phys. Rev. Lett.* **55**, 2409 (1985).
32. L. A. Wu *et al.*, "Generation of squeezed states by parametric down conversion," *Phys. Rev. Lett.* **57**, 2520 (1986).
33. R. M. Shelby *et al.*, "Broad-band parametric deamplification of quantum noise in an optical fiber," *Phys. Rev. Lett.* **57**, 691 (1986).
34. H. Vahlbruch *et al.*, "Detection of 15 dB squeezed states of light and their application for the absolute calibration of photoelectric quantum efficiency," *Phys. Rev. Lett.* **117**, 110801 (2016).
35. S. Shi *et al.*, "Detection and perfect fitting of 13.2 dB squeezed vacuum states by considering green-light-induced infrared absorption," *Opt. Lett.* **43**, 5411 (2018).
36. The LIGO Scientific Collaboration, "A gravitational wave observatory operating beyond the quantum shot-noise limit," *Nat. Phys.* **7**, 962 (2011).
37. The LIGO Scientific Collaboration, "Enhanced sensitivity of the LIGO gravitational wave detector by using squeezed states of light," *Nat. Photon.* **7**, 613 (2013).
38. H. Grote *et al.*, "First long-term application of squeezed states of light in a gravitational-wave observatory," *Phys. Rev. Lett.* **110**, 181101 (2013).
39. N. Treps *et al.*, "A quantum laser pointer," *Science* **301**, 940 (2003).
40. R. C. Pooser and B. Lawie, "Ultrasensitive measurement of microcantilever displacement below the shot-noise limit," *Optica* **2**, 393 (2015).
41. K. Liu *et al.*, "Squeezing-enhanced rotating-angle measurement beyond the quantum limit," *Appl. Phys. Lett.* **113**, 261103 (2018).
42. B. Lamine, C. Fabre, and N. Treps, "Quantum improvement of time transfer between remote clocks," *Phys. Rev. Lett.* **101**, 123601 (2008).
43. A. Einstein, B. Podolsky, and N. Rosen, "Can quantum mechanical description of physical reality be considered complete," *Phys. Rev.* **47**, 777 (1935).
44. Z. Y. Ou *et al.*, "Realization of the Einstein-Podolsky-Rosen paradox for continuous-variables," *Phys. Rev. Lett.* **68**, 3663 (1992).
45. M. D. Reid, "Demonstration of the Einstein-Podolsky-Rosen paradox using nondegenerate parametric amplification," *Phys. Rev. A* **40**, 913 (1989).
46. L. M. Duan *et al.*, "Inseparability criterion for continuous variable systems," *Phys. Rev. Lett.* **84**, 2722 (2000).
47. R. Simon, "Peres-horodecki separability criterion for continuous variable systems," *Phys. Rev. Lett.* **84**, 2726 (2000).
48. Y. Zhang *et al.*, "Experimental generation of bright two-mode quadrature squeezed light from a narrow-band nondegenerate optical parametric amplifier," *Phys. Rev. A* **62**, 023813 (2000).
49. P. van Loock and S. L. Braunstein, "Multipartite entanglement for continuous variables: a quantum teleportation network," *Phys. Rev. Lett.* **84**, 3482 (2000).
50. P. van Loock and S. L. Braunstein, "Telecloning of continuous quantum variables," *Phys. Rev. Lett.* **87**, 247901 (2001).
51. T. Aoki *et al.*, "Experimental creation of a fully inseparable tripartite continuous-variable state," *Phys. Rev. Lett.* **91**, 080404 (2003).
52. H. Yonezawa, T. Aoki, and A. Furusawa, "Demonstration of a quantum teleportation network for continuous variables," *Nature* **431**, 430 (2004).
53. S. Koike *et al.*, "Demonstration of quantum telecloning of optical coherent states," *Phys. Rev. Lett.* **96**, 060504 (2006).
54. X. Su *et al.*, "Experimental preparation of quadripartite cluster and Greenberger-Horne-Zeilinger entangled states for continuous variables," *Phys. Rev. Lett.* **98**, 070502 (2007).
55. X. Su *et al.*, "Experimental preparation of eight-partite cluster state for photonic qumodes," *Opt. Lett.* **37**, 5178 (2012).
56. F. A. S. Barbosa *et al.*, "Robustness of bipartite Gaussian entangled beams propagating in lossy channels," *Nat. Photon.* **4**, 858 (2010).
57. A. S. Villar *et al.*, "Generation of bright two-color continuous variable entanglement," *Phys. Rev. Lett.* **95**, 243603 (2005).
58. F. A. S. Barbosa *et al.*, "Hexapartite entanglement in an above-threshold optical parametric oscillator," *Phys. Rev. Lett.* **121**, 073601 (2018).
59. L. F. Muñoz-Martínez *et al.*, "Exploring six modes of an optical parametric oscillator," *Phys. Rev. A* **98**, 023823 (2018).

60. S. Yokoyama *et al.*, "Ultra-large-scale continuous-variable cluster states multiplexed in the time domain," *Nat. Photon.* **7**, 982 (2013).
61. S. Armstrong *et al.*, "Programmable multimode quantum networks," *Nat. Commun.* **3**, 1026 (2012).
62. M. Chen, N. C. Menicucci, and O. Pfister, "Experimental realization of multipartite entanglement of 60 modes of a quantum optical frequency comb," *Phys. Rev. Lett.* **112**, 120505 (2014).
63. Z. Yang *et al.*, "A squeezed quantum microcomb on a chip," *Nat. Commun.* **12**, 4781 (2021).
64. J. Roslund *et al.*, "Wavelength-multiplexed quantum networks with ultrafast frequency combs," *Nat. Photon.* **8**, 109 (2014).
65. Y. Cai *et al.*, "Multimode entanglement in reconfigurable graph states using optical frequency combs," *Nat. Commun.* **8**, 15645 (2017).
66. S. L. Braunstein and H. J. Kimble, "Teleportation of continuous quantum variables," *Phys. Rev. Lett.* **80**, 869 (1998).
67. A. Furusawa *et al.*, "Unconditional quantum teleportation," *Science* **282**, 706 (1998).
68. N. Lee *et al.*, "Teleportation of nonclassical wave packets of light," *Science* **332**, 330 (2011).
69. M. Huo *et al.*, "Deterministic quantum teleportation through fiber channels," *Sci. Adv.* **4**, eaas9401 (2018).
70. X. Li *et al.*, "Quantum dense coding exploiting a bright Einstein-Podolsky-Rosen beam," *Phys. Rev. Lett.* **88**, 047904 (2002).
71. X. Jia *et al.*, "Experimental demonstration of unconditional entanglement swapping for continuous variables," *Phys. Rev. Lett.* **93**, 250503 (2004).
72. C. F. McCormick *et al.*, "Strong relative intensity squeezing by four-wave mixing in rubidium vapor," *Opt. Lett.* **32**, 178 (2007).
73. R. C. Pooser *et al.*, "Quantum correlated light beams from non-degenerate four-wave mixing in an atomic vapor: the D1 and D2 lines of ^{85}Rb and ^{87}Rb," *Opt. Express* **17**, 16722 (2009).
74. J. D. Swaim and R. T. Glasser, "Squeezed-twin-beam generation in strongly absorbing media," *Phys. Rev. A* **96**, 033818 (2017).
75. M. Guo *et al.*, "Experimental investigation of high-frequency-difference twin beams in hot cesium atoms," *Phys. Rev. A* **89**, 033813 (2014).
76. R. Ma *et al.*, "Generating quantum correlated twin beams by four-wave mixing in hot cesium vapor," *Phys. Rev. A* **96**, 043843 (2017).
77. A. M. Marino, V. Boyer, and P. D. Lett, "Violation of the Cauchy-Schwarz inequality in the macroscopic regime," *Phys. Rev. Lett.* **100**, 233601 (2008).
78. H. Vahlbruch *et al.*, "Observation of squeezed light with 10-dB quantum-noise reduction," *Phys. Rev. Lett.* **100**, 033602 (2008).
79. D. Zhang *et al.*, "Enhanced intensity-difference squeezing via energy-level modulations in hot atomic media," *Phys. Rev. A* **96**, 043847 (2017).
80. Q. Glorieux *et al.*, "Generation of pulsed bipartite entanglement using four-wave mixing," *New J. Phys.* **14**, 123024 (2012).
81. D. Budker and M. Romalis, "Optical magnetometry," *Nat. Phys.* **3**, 227 (2007).
82. A. M. Marino and P. D. Lett, "Absolute calibration of photodiodes with bright twin beams," *J. Mod. Opt.* **58**, 328 (2011).
83. C. F. McCormick *et al.*, "Strong low-frequency quantum correlations from a four-wave-mixing amplifier," *Phys. Rev. A* **78**, 043816 (2008).
84. M. C. Wu *et al.*, "Twin-beam intensity-difference squeezing below 10 Hz," *Opt. Express* **27**, 4769 (2019).
85. M. I. Kolobov, *Quantum Imaging* (Springer, 2006).
86. V. Boyer, A. M. Marino, and P. D. Lett, "Generation of spatially broadband twin beams for quantum imaging," *Phys. Rev. Lett.* **100**, 143601 (2008).
87. M. W. Holtfrerich and A. M. Marino, "Control of the size of the coherence area in entangled twin besms" *Phys. Rev. A* **93**, 063821 (2016).
88. C. S. Embrey *et al.*, "Observation of localized multi-spatial-mode quadrature squeezing," *Phys. Rev. X* **5**, 031004 (2015).
89. Q. Glorieux *et al.*, "Temporally multiplexed storage of images in a gradient echo memory," *Opt. Express* **20**, 12350 (2012).
90. D.-S. Ding *et al.*, "Image transfer through two sequential four-wave mixing processes in hot atomic vapor," *Phys. Rev. A* **85**, 053815 (2012).
91. J. B. Clark *et al.*, "Imaging using quantum noise properties of light," *Opt. Express* **20**, 17050 (2012).
92. E. Brambilla *et al.*, "High-sensitivity imaging with multi-mode twin beams," *Phys. Rev. A* **77**, 053807 (2008).
93. V. Boyer *et al.*, "Entangled images from four-wave mixing," *Science* **321**, 544 (2008).
94. B. J. Lawrie and R. C. Pooser, "Toward real-time quantum imaging with a single pixel camera," *Opt. Express* **21**, 7549 (2013).
95. A. M. Marino *et al.*, "Tunable delay of Einstein–Podolsky–Rosen entanglement," *Nature* **457**, 859 (2009).
96. V. Boyer *et al.*, "Ultraslow propagation of matched pulses by four-wave mixing in an atomic vapor," *Phys. Rev. Lett.* **99**, 143601 (2007).
97. R. T. Glasser, U. Vogl, and P. D. Lett, "Stimulated generation of superluminal light pulses via four-wave mixing," *Phys. Rev. Lett.* **108**, 173902 (2012).
98. U. Vogl *et al.*, "Advanced quantum noise correlations," *New J. Phys.* **16**, 013011 (2014).
99. J. B. Clark *et al.*, "Quantum mutual information of an entangled state propagating through a fast-light medium," *Nat. Photon.* **8**, 515 (2014).
100. N. V. Corzo *et al.*, "Noiseless optical amplifier operating on hundreds of spatial modes," *Phys. Rev. Lett.* **109**, 043602 (2012).
101. N. Corzo *et al.*, "Multi-spatial-mode single-beam quadrature squeezed states of light from four-wave mixing in hot rubidium vapor," *Opt. Express* **19**, 21358 (2011).
102. S. Liu, Y. Lou, and J. Jing, "Interference-induced quantum squeezing enhancement in a two-beam phase-sensitive amplifier," *Phys. Rev. Lett.* **123**, 113602 (2019).
103. S. Liu, Y. Lou, and J. Jing, "Phase manipulated two-mode entangled state from a phase-sensitive amplifier," *Opt. Express* **29**, 38971 (2021).
104. O. Danaci, C. Rios, and R. T. Glasser, "All-optical mode conversion via spatially multimode four-wave mixing," *New J. Phys.* **18**, 073032 (2016).
105. S. Kim and A. M. Marino, "Atomic resonant single-mode squeezed light from four-wave mixing through feedforward," *Opt. Lett.* **44**, 4630 (2019).
106. S. Kim and A. M. Marino, "Generation of ^{87}Rb resonant bright two-mode squeezed light with four-wave mixing," *Opt. Express* **26**, 33366 (2018).
107. P. Gupta *et al.*, "Effect of imperfect homodyne visibility on multi-spatial-mode two-mode squeezing measurements," *Opt. Express* **28**, 652 (2020).
108. U. Vogl *et al.*, "Experimental characterization of Gaussian quantum discord generated by four-wave mixing," *Phys. Rev. A* **87**, 010101(R) (2013).
109. A. Kumar and A. M. Marino, "Spatial squeezing in bright twin beams generated with four-wave mixing: constraints on characterization with an electron-multiplying charge-coupled-device camera," *Phys. Rev. A* **100**, 063828 (2019).
110. A. Kumar, G. Nirala, and A. M. Marino, "Einstein–Podolsky–Rosen paradox with position–momentum entangled macroscopic twin beams," *Quantum Sci. Technol.* **6**, 045016 (2021).
111. A. Kumar, H. Nunley, and A. M. Marino, "Comparison of coherence-area measurement techniques for bright entangled twin beams," *Phys. Rev. A* **98**, 043853 (2018).
112. B. J. Lawrie *et al.*, "Robust and compact entanglement generation from diode-laser-pumped four-wave mixing," *Appl. Phys. Lett.* **108**, 151107 (2016).

113. A. M. Guerrero *et al.*, "Quantum noise correlations of an optical parametric oscillator based on a nondegenerate four wave mixing process in hot alkali atoms," *Phys. Rev. Lett.* **125**, 083601 (2020).
114. C. M. Caves, "Quantum-mechanical noise in an interferometer," *Phys. Rev. D* **23**, 1693 (1981).
115. F. Wolfgramm *et al.*, "Squeezed-light optical magnetometry," *Phys. Rev. Lett.* **105**, 053601 (2010).
116. B. Li *et al.*, "Quantum enhanced optomechanical magnetometry," *Optica* **5**, 850 (2018).
117. B. J. Lawrie *et al.*, "Quantum sensing with squeezed light," *ACS Photonics* **6**, 1307 (2019).
118. W. Fan, B. J. Lawrie, and R. C. Pooser, "Quantum plasmonic sensing," *Phys. Rev. A* **92**, 053812 (2015).
119. R. C. Pooser and B. J. Lawrie, "Plasmonic trace sensing below the photon shot noise limit," *ACS Photonics* **3**, 8 (2016).
120. M. Dowran *et al.*, "Quantum-enhanced plasmonic sensing," *Optica* **5**, 628 (2018).
121. B. J. Lawrie, P. G. Evans, and R. C. Pooser, "Extraordinary optical transmission of multimode quantum correlations via localized surface plasmons," *Phys. Rev. Lett.* **110**, 156802 (2013).
122. M. W. Holtfreric *et al.*, "Toward quantum plasmonic networks," *Optica* **3**, 985 (2016).
123. M. C. Wu *et al.*, "Two-beam coupling in the production of quantum correlated images by four-wave mixing," *Opt. Express* **29**, 16665 (2021).
124. J. Jing *et al.*, "Realization of a nonlinear interferometer with parametric amplifiers," *Appl. Phys. Lett.* **99**, 011110 (2011).
125. A. M. Marino, N. V. Corzo Trejo, and P. D. Lett, "Effect of losses on the performance of an SU(1,1) interferometer," *Phys. Rev. A* **86**, 023844 (2012).
126. F. Hudelist *et al.*, "Quantum metrology with parametric amplifier-based photon correlation interferometers," *Nat. Commun.* **5**, 3049 (2014).
127. B. E. Anderson *et al.*, "Phase sensing beyond the standard quantum limit with a variation on the SU(1,1) interferometer," *Optica* **4**, 752 (2017).
128. R. C. Pooser *et al.*, "Truncated nonlinear interferometry for quantum-enhanced atomic force microscopy," *Phys. Rev. Lett.* **124**, 230504 (2020).
129. J. M. Lukens, N. A. Peters, and R. C. Pooser, "Naturally stable Sagnac–Michelson nonlinear interferometer," *Opt. Lett.* **41**, 5438 (2016).
130. X. Guo *et al.*, "Distributed quantum sensing in a continuous-variable entangled network," *Nat. Phys.* **16**, 281 (2020).
131. Y. Xia *et al.*, "Demonstration of a reconfigurable entangled radio-frequency photonic sensor network," *Phys. Rev. Lett.* **124**, 150502 (2020).
132. Y. Zhou *et al.*, "Quantum secret sharing among four players using multipartite bound entanglement of an optical field," *Phys. Rev. Lett.* **121**, 150502 (2018).
133. A. S. Coelho *et al.*, "Three-color entanglement," *Science* **326**, 823 (2009).
134. X. Jia *et al.*, "Experimental realization of three-color entanglement at optical fiber communication and atomic storage wavelengths," *Phys. Rev. Lett.* **109**, 253604 (2012).
135. Z. Qin *et al.*, "Experimental generation of multiple quantum correlated beams from hot rubidium vapor," *Phys. Rev. Lett.* **113**, 023602 (2014).
136. L. Cao *et al.*, "Experimental generation of quadruple quantum-correlated beams from hot rubidium vapor by cascaded four-wave mixing using spatial multiplexing," *Phys. Rev. A* **95**, 023803 (2017).
137. H. Wang, C. Fabre, and J. Jing, "Single-step fabrication of scalable multimode quantum resources using four-wave mixing with a spatially structured pump," *Phys. Rev. A* **95**, 051802 (2017).
138. K. Zhang *et al.*, "Reconfigurable hexapartite entanglement by spatially multiplexed four-wave mixing processes," *Phys. Rev. Lett.* **124**, 090501(2020).
139. S. Liu, H. Wang, and J. Jing, "Two-beam pumped cascaded four-wave-mixing process for producing multiple-beam quantum correlation," *Phys. Rev. A* **97**, 043846 (2018).
140. S. Liu, Y. Lou, and J. Jing, "Experimental characterization of multiple quantum correlated beams in two-beam pumped cascaded four-wave mixing process," *Opt. Express* **27**, 37999 (2019).
141. J. D. Swaim *et al.*, "Multimode four-wave mixing with a spatially structured pump," *Opt. Lett.* **43**, 2716 (2018).
142. E. M. Knutson *et al.*, "Phase-sensitive amplification via multi-phase-matched four-wave mixing," *Opt. Express* **28**, 22748 (2020).
143. E. M. Knutson *et al.*, "Optimal mode configuration for multiple phase-matched four-wave-mixing processes," *Phys. Rev. A* **98**, 013828 (2018).
144. M. E. J. Friese *et al.*, "Optical angular-momentum transfer to trapped absorbing particles," *Phys. Rev. A* **54**, 1593 (1996).
145. G. Gibson *et al.*, "Free-space information transfer using light beams carrying orbital angular momentum," *Opt. Express* **12**, 5448 (2004).
146. M. F. Andersen *et al.*, "Quantized rotation of atoms from photons with orbital angular momentum," *Phys. Rev. Lett.* **97**, 170406 (2006).
147. L. Allen *et al.*, "Orbital angular momentum of light and the transformation of Laguerre-Gaussian laser modes," *Phys. Rev. A* **45**, 8185 (1992).
148. R. Fickler *et al.*, "Quantum entanglement of high angular momenta," *Science* **338**, 640 (2012).
149. A. M. Marino *et al.*, "Delocalized correlations in twin light beams with orbital angular momentum," *Phys. Rev. Lett.* **101**, 093602 (2008).
150. J. Wang *et al.*, "Terabit free-space data transmission employing orbital angular momentum multiplexing," *Nat. Photon.* **6**, 488 (2012).
151. N. Bozinovic *et al.*, "Terabit-scale orbital angular momentum mode division multiplexing in fibers," *Science* **340**, 1545 (2013).
152. A. Trichili *et al.*, "Encoding information using Laguerre Gaussian modes over free space turbulence media," *Opt. Lett.* **41**, 3086 (2016).
153. R. C. Devlin *et al.*, "Arbitrary spin-to–orbital angular momentum conversion of light," *Science* **358**, 896 (2017).
154. X. Wang *et al.*, "Quantum teleportation of multiple degrees of freedom of a single photon," *Nature* **518**, 516 (2015).
155. T.-M. Zhao, Y. S. Ihn, and Y.-H. Kim, "Direct generation of narrow-band hyperentangled photons," *Phys. Rev. Lett.* **122**, 123607 (2019).
156. Y. Zhang *et al.*, "Simultaneous entanglement swapping of multiple orbital angular momentum states of light," *Nat. Commun.* **8**, 632 (2017).
157. A. Vaziri, G. Weihs, and A. Zeilinger, "Experimental two-photon, three-dimensional entanglement for quantum communication," *Phys. Rev. Lett.* **89**, 240401 (2002).
158. S. Franke-Arnold *et al.*, "Uncertainty principle for angular position and angular momentum," *New J. Phys.* **6**, 103 (2004).
159. S. S. R. Oemrawsingh *et al.*, "Experimental demonstration of fractional orbital angular momentum entanglement of two photons," *Phys. Rev. Lett.* **95**, 240501 (2005).
160. G. Molina-Terriza, J. P. Torres, and L. Torner, "Twisted photons," *Nat. Phys.* **3**, 305 (2007).
161. J. Leach *et al.*, "Quantum correlations in optical angle–orbital angular momentum variables," *Science* **329**, 662 (2010).
162. A. M. Yao, "Angular momentum decomposition of entangled photons with an arbitrary pump," *New J. Phys.* **13**, 053048 (2011).
163. D. S. Ding *et al.*, "Quantum storage of orbital angular momentum entanglement in an atomic ensemble," *Phys. Rev. Lett.* **114**, 050502 (2015).

164. Z. Q. Zhou *et al.*, "Quantum storage of three-dimensional orbital-angular-momentum entanglement in a crystal," *Phys. Rev. Lett.* **115**, 070502 (2015).
165. Z. Y. Zhou *et al.*, "Orbital angular momentum-entanglement frequency transducer," *Phys. Rev. Lett.* **117**, 103601 (2016).
166. B. C. Hiesmayr, M. J. A. de Dood, and W. Löffler, "Observation of four-photon orbital angular momentum entanglement," *Phys. Rev. Lett.* **116**, 073601 (2016).
167. M. Mafu *et al.*, "Higher-dimensional orbital-angular-momentum-based quantum key distribution with mutually unbiased bases," *Phys. Rev. A* **88**, 032305 (2013).
168. A. HamadouIbrahim *et al.*, "Orbital-angular-momentum entanglement in turbulence," *Phys. Rev. A* **88**, 012312 (2013).
169. A. Sit *et al.*, "High-dimensional intracity quantum cryptography with structured photons," *Optica* **4**, 1006 (2017).
170. F. Bouchard, R. Fickler, and E. Karimi, "High-dimensional quantum cloning and applications to quantum hacking," *Sci. Adv.* **3**, e1601915 (2017).
171. M. Krenn *et al.*, "Generation and confirmation of a (100 × 100)-dimensional entangled quantum system," *Proc. Natl. Acad. Sci. U.S.A.* **111**, 6243 (2014).
172. S. P. Walborn *et al.*, "Entanglement and conservation of orbital angular momentum in spontaneous parametric down-conversion," *Phys. Rev. A* **69**, 023811 (2004).
173. C. K. Law and J. H. Eberly, "Analysis and interpretation of high transverse entanglement in optical parametric down conversion," *Phys. Rev. Lett.* **92**, 127903 (2004).
174. L. K. Shalm *et al.*, "Three-photon energy–time entanglement," *Nat. Phys.* **9**, 19 (2013).
175. C. Weedbrook *et al.*, "Gaussian quantum information," *Rev. Mod. Phys.* **84**, 621 (2012).
176. S. Li *et al.*, "Deterministic generation of orbital-angular-momentum multiplexed tripartite entanglement," *Phys. Rev. Lett.* **124**, 083605 (2020).
177. W. Wang, K. Zhang, and J. Jing, "Large-scale quantum network over 66 orbital angular momentum optical modes," *Phys. Rev. Lett.* **125**, 140501 (2020).
178. S. Tanzilli *et al.*, "On the genesis and evolution of integrated quantum optics," *Laser Photonics Rev.* **6**, 115 (2012).
179. L. Caspani *et al.*, "Integrated sources of photon quantum states based on nonlinear optics," *Light Sci. Appl.* **6**, e17100 (2017).
180. M. Kues *et al.*, "Quantum optical microcombs," *Nat. Photon.* **13**, 170 (2019).
181. F. Lenzini *et al.*, "Integrated photonic platform for quantum information with continuous variables," *Sci. Adv.* **4**, eaat9331 (2018).
182. C. H. Bennett *et al.*, "Teleporting an unknown quantum state via dual classical and Einstein-Podolsky-Rosen channels," *Phys. Rev. Lett.* **70**, 1895 (1993).
183. D. Bouwmeester *et al.*, "Experimental quantum teleportation," *Nature* **390**, 575 (1997).
184. M. A. Nielsen, E. Knill, and R. Laflamme, "Complete quantum teleportation using nuclear magnetic resonance," *Nature* **396**, 52 (1998).
185. I. Marcikic *et al.*, "Long-distance teleportation of qubits at telecommunication wavelengths," *Nature* **421**, 509 (2003).
186. M. Riebe *et al.*, "Deterministic quantum teleportation with atoms," *Nature* **429**, 734 (2004).
187. M. D. Barrett *et al.*, "Deterministic quantum teleportation of atomic qubits," *Nature* **429**, 737 (2004).
188. J. F. Sherson *et al.*, "Quantum teleportation between light and matter," *Nature* **443**, 557 (2006).
189. S. Olmschenk *et al.*, "Quantum teleportation between distant matter qubits," *Science* **323**, 486 (2009).
190. L. Steffen *et al.*, "Deterministic quantum teleportation with feed-forward in a solid state system," *Nature* **500**, 319 (2013).
191. J. Yin *et al.*, "Quantum teleportation and entanglement distribution over 100-kilometre free-space channels," *Nature* **488**, 185 (2012).
192. X. -S. Ma *et al.*, "Quantum teleportation over 143 kilometres using active feed-forward," *Nature* **489**, 269 (2012).
193. J.-G. Ren *et al.*, "Ground-to-satellite quantum teleportation," *Nature* **549**, 70 (2017).
194. W. Pfaff *et al.*, "Unconditional quantum teleportation between distant solid-state quantum bits," *Science* **345**, 532 (2014).
195. Y.-H. Luo *et al.*, "Quantum teleportation in high dimensions," *Phys. Rev. Lett.* **123**, 070505 (2019).
196. M. Yukawa, H. Benichi, and A. Furusawa, "High-fidelity continuous-variable quantum teleportation toward multistep quantum operations," *Phys. Rev. A* **77**, 022314 (2008).
197. L. Vaidman, "Teleportation of quantum states," *Phys. Rev. A* **49**, 1473 (1994).
198. T. C. Ralph, "All-optical quantum teleportation," *Opt. Lett.* **24**, 348 (1999).
199. S. Liu, Y. Lou, and J. Jing, "Orbital angular momentum multiplexed deterministic all-optical quantum teleportation," *Nat. Commun.* **11**, 3875 (2020).
200. S. Pirandola *et al.*, "Fundamental limits of repeaterless quantum communications," *Nat. Commun.* **8**, 15043 (2017).
201. Z.-S. Yuan *et al.*, "Experimental demonstration of a BDCZ quantum repeater node," *Nature* **454**, 1098 (2008).
202. M. Żukowski *et al.*, ""Event-ready-detectors" Bell experiment via entanglement swapping," *Phys. Rev. Lett.* **71**, 4287 (1993).
203. J.-W. Pan *et al.*, "Experimental entanglement swapping: entangling photons that never interacted," *Phys. Rev. Lett.* **80**, 3891 (1998).
204. T. Jennewein *et al.*, "Experimental nonlocality proof of quantum teleportation and entanglement swapping," *Phys. Rev. Lett.* **88**, 017903 (2001).
205. X.-S. Ma *et al.*, "Experimental delayed-choice entanglement swapping," *Nat. Phys.* **8**, 479 (2012).
206. M. Halder *et al.*, "Entangling independent photons by time measurement," *Nat. Phys.* **3**, 692 (2007).
207. W. Ning *et al.*, "Deterministic entanglement swapping in a superconducting circuit," *Phys. Rev. Lett.* **123**, 060502 (2019).
208. R. E. S. Polkinghorne and T. C. Ralph, "Continuous variable entanglement swapping," *Phys. Rev. Lett.* **83**, 2095 (1999).
209. S. M. Tan, "Confirming entanglement in continuous variable quantum teleportation," *Phys. Rev. A* **60**, 2752 (1999).
210. P. van Loock and S. L. Braunstein, "Unconditional teleportation of continuous-variable entanglement," *Phys. Rev. A* **61**, 010302 (R) (1999).
211. N. Takei *et al.*, "High-fidelity teleportation beyond the no-cloning limit and entanglement swapping for continuous variables," *Phys. Rev. Lett.* **94**, 220502 (2005).
212. S. Liu *et al.*, "All-optical entanglement swapping," *Phys. Rev. Lett.* **128**, 060503 (2022).
213. R. C. Pooser *et al.*, "Low-noise amplification of a continuous-variable quantum state," *Phys. Rev. Lett.* **103**, 010501 (2009).
214. W. K. Wooters and W. H. Zurek, "A single quantum cannot be cloned," *Nature* **299**, 802 (1982).
215. D. Dieks, "Communication by EPR devices," *Phys. Lett. A* **92**, 271 (1982).
216. V. Bužek and M. Hillery, "Quantum copying: beyond the no-cloning theorem," *Phys. Rev. A* **54**, 1844 (1996).
217. A. Lamas-Linares *et al.*, "Experimental quantum cloning of single photons," *Science* **296**, 712 (2002).
218. W. T. M. Irvine *et al.*, "Optimal quantum cloning on a beam splitter," *Phys. Rev. Lett.* **92**, 047902 (2004).
219. S. Fasel *et al.*, "Quantum cloning with an optical fiber amplifier," *Phys. Rev. Lett.* **89**, 107901 (2002).
220. E. Nagali *et al.*, "Experimental optimal cloning of four-dimensional quantum states of photons," *Phys. Rev. Lett.* **105**, 073602 (2010).

221. E. Nagali *et al.*, "Optimal quantum cloning of orbital angular momentum photon qubits through Hong–Ou–Mandel coalescence," *Nat. Photon.* **3**, 720 (2009).
222. U. L. Andersen, V. Josse, and G. Leuchs, "Unconditional quantum cloning of coherent states with linear optics," *Phys. Rev. Lett.* **94**, 240503 (2005).
223. J. Y. Haw *et al.*, "Surpassing the no-cloning limit with a heralded hybrid linear amplifier for coherent states," *Nat. Commun.* **7**, 13222 (2016).
224. M. Sabuncu, U. L. Andersen, and G. Leuchs, "Experimental demonstration of continuous variable cloning with phase-conjugate inputs," *Phys. Rev. Lett.* **98**, 170503 (2007).
225. J. Fiurášek, "Optical implementation of continuous-variable quantum cloning machines," *Phys. Rev. Lett.* **86**, 4942 (2001).
226. S. L. Braunstein *et al.*, "Optimal cloning of coherent states with a linear amplifier and beam splitters," *Phys. Rev. Lett.* **86**, 4938 (2001).
227. S. Liu *et al.*, "All-optical optimal *N*-to-*M* quantum cloning of coherent states," *Phys. Rev. Lett.* **126**, 060503 (2021).
228. H. J. Kimble, "The quantum internet," *Nature* **453**, 1023 (2008).
229. F. Bussières *et al.*, "Quantum teleportation from a telecom-wavelength photon to a solid-state quantum memory," *Nat. Photon.* **8**, 775 (2014).
230. S. Takeda and A. Furusawa, "Toward large-scale fault-tolerant universal photonic quantum computing," *APL Photonics* **4**, 060902 (2019).
231. K. Mattle *et al.*, "Dense coding in experimental quantum communication," *Phys. Rev. Lett.* **76**, 4656 (1996).
232. M. Hillery, V. Bužek, and A. Berthiaume, "Quantum secret sharing," *Phys. Rev. A* **59**, 1829 (1999).
233. Y. Lou, S. Liu, and J. Jing, "Experimental demonstration of a multifunctional all-optical quantum state transfer machine," *Phys. Rev. Lett.* **126**, 210507 (2021).
234. S. L. Braunstein and H. J. Kimble, "Dense coding for continuous variables," *Phys. Rev. A* **61**, 042302 (2000).
235. J. Zhang and K. Peng, "Quantum teleportation and dense coding by means of bright amplitude-squeezed light and direct measurement of a Bell state," *Phys. Rev. A* **62**, 064302 (2000).
236. M. Ban, "Quantum dense coding via a two-mode squeezed-vacuum state," *J. Opt. B* **1**, L9 (1999).
237. T. C. Ralph and E. H. Huntington, "Unconditional continuous-variable dense coding," *Phys. Rev. A* **66**, 042321 (2002).
238. J. Mizuno *et al.*, "Experimental demonstration of entanglement-assisted coding using a two-mode squeezed vacuum state," *Phys. Rev. A* **71**, 012304 (2005).
239. X. Hu *et al.*, "Beating the channel capacity limit for superdense coding with entangled ququarts," *Sci. Adv.* **4**, eaat9304 (2018).
240. S. Shi *et al.*, "Demonstration of channel multiplexing quantum communication exploiting entangled sideband modes," *Phys. Rev. Lett.* **125**, 070502 (2020).
241. Y. Chen *et al.*, "Orbital angular momentum multiplexed quantum dense coding," *Phys. Rev. Lett.* **127**, 093601 (2021).
242. V. Giovannetti, S. Lloyd, and L. Maccone, "Quantum metrology," *Phys. Rev. Lett.* **96**, 010401 (2006).
243. B. Yurke, S. L. McCall, and J. R. Klauder, "SU(2) and SU(1,1) interferometers," *Phys. Rev. A* **33**, 4033 (1986).
244. G. Frascella *et al.*, "Wide-field SU(1,1) interferometer," *Optica* **6**, 1233 (2019).
245. S. Lemieux *et al.*, "Engineering the frequency spectrum of bright squeezed vacuum via group velocity dispersion in an SU(1,1) interferometer," *Phys. Rev. Lett.* **117**, 183601 (2016).
246. P. R. Sharapova *et al.*, "Bright squeezed vacuum in a nonlinear interferometer: Frequency and temporal Schmidt-mode description," *Phys. Rev. A* **97**, 053827 (2018).
247. A. A. Michelson and E. W. Morley, "On the relative motion of the earth and the luminiferous ether," *Am. J. Sci.* **s3-34**, 333 (1887).
248. S. L. Braunstein, "Quantum limits on precision measurements of phase," *Phys. Rev. Lett.* **69**, 3598 (1992).
249. K. Goda *et al.*, "A quantum-enhanced prototype gravitational-wave detector," *Nat. Phys.* **4**, 472 (2008).
250. G. M. Harry (for the LIGO Scientific Collaboration), "Advanced LIGO: the next generation of gravitational wave detectors," *Class. Quantum Grav.* **27**, 084006 (2010).
251. M. Xiao, L. A. Wu, and H. J. Kimble, "Precision measurement beyond the shot-noise limit," *Phys. Rev. Lett.* **59**, 278 (1987).
252. K. McKenzie *et al.*, "Experimental demonstration of a squeezing-enhanced power-recycled michelson interferometer for gravitational wave detection," *Phys. Rev. Lett.* **88**, 231102 (2002).
253. H. Vahlbruch *et al.*, "Demonstration of a squeezed-light-enhanced power- and signal-recycled michelson interferometer," *Phys. Rev. Lett.* **95**, 211102 (2005).
254. A. Kolkiran and G. S. Agarwal, "Quantum interferometry using coherent beam stimulated parametric down-conversion," *Opt. Express* **16**, 6479 (2008).
255. M. W. Mitchell, J. S. Lundeen, and A. M. Steinberg, "Super-resolving phase measurements with a multiphoton entangled state," *Nature* **429**, 161 (2004).
256. J. P. Dowling, "Quantum optical metrology—the lowdown on high-N00N states," *Contemp. Phys.* **49**, 125 (2008).
257. G. Y. Xiang *et al.*, "Entanglement-enhanced measurement of a completely unknown optical phase," *Nat. Photon.* **5**, 43 (2010).
258. A. Kuzmich and L. Mandel, "Sub-shot-noise interferometric measurements with two-photon states," *Quantum Semiclass. Opt.* **10**, 493 (1998).
259. A. N. Boto *et al.*, "Quantum interferometric optical lithography: exploiting entanglement to beat the diffraction limit," *Phys. Rev. Lett.* **85**, 2733 (2000).
260. P. M. Anisimov *et al.*, "Quantum metrology with two-mode squeezed vacuum: parity detection beats the Heisenberg limit," *Phys. Rev. Lett.* **104**, 103602 (2010).
261. A. Rivas and A. Luis, "Precision quantum metrology and nonclassicality in linear and nonlinear detection schemes," *Phys. Rev. Lett.* **105**, 010403 (2010).
262. D. Li *et al.*, "Phase sensitivity at the Heisenberg limit in an SU (1,1) interferometer via parity detection," *Phys. Rev. A* **94**, 063840 (2016).
263. B. E. Anderson *et al.*, "Optimal phase measurements with bright- and vacuum-seeded SU(1,1) interferometers," *Phys. Rev. A* **95**, 063843 (2017).
264. S. S. Szigeti, R. J. Lewis-Swan, and S. A. Haine, "Pumped-up SU(1,1) interferometry," *Phys. Rev. Lett.* **118**, 150401 (2017).
265. M. Manceau *et al.*, "Detection loss tolerant supersensitive phase measurement with an SU(1,1) interferometer," *Phys. Rev. Lett.* **119**, 223604 (2017).
266. S. Liu *et al.*, "Quantum enhancement of phase sensitivity for the bright-seeded SU(1,1) interference with direct intensity detection," *Phys. Rev. Appl.* **10**, 064046 (2018).
267. Y. Shang *et al.*, "Continuous variable entanglement enhancement and manipulation by a subthreshold type II optical parametric amplifier," *Opt. Lett.* **35**, 853 (2010).
268. Z. Yan *et al.*, "Cascaded entanglement enhancement," *Phys. Rev. A* **85**, 040305 (2012).
269. J. Xin, J. Qi, and J. Jing, "Enhancement of entanglement using cascaded four-wave mixing processes," *Opt. Lett.* **42**, 366 (2017).
270. S. S. Szigeti *et al.*, "Squeezed-light-enhanced atom interferometry below the standard quantum limit," *Phys. Rev. A* **90**, 063630 (2014).
271. Z. Y. Ou, "Enhancement of the phase-measurement sensitivity beyond the standard quantum limit by a nonlinear interferometer," *Phys. Rev. A* **85**, 023815 (2012).
272. R. Schnabel *et al.*, "Quantum metrology for gravitational wave astronomy," *Nat. Commun.* **1**, 121 (2010).
273. J. Kong *et al.*, "Experimental investigation of the visibility dependence in a nonlinear interferometer using parametric amplifiers," *Appl. Phys. Lett.* **102**, 011130 (2013).

274. J. Kong *et al.*, "Cancellation of internal quantum noise of an amplifier by quantum correlation," *Phys. Rev. Lett.* **111**, 033608 (2013).
275. J. Xin, H. Wang, and J. Jing, "The effect of losses on the quantum-noise cancellation in the SU(1,1) interferometer," *Appl. Phys. Lett.* **109**, 051107 (2016).
276. T. Kim *et al.*, "Precision measurement scheme using a quantum interferometer," *Phys. Rev. A* **72**, 055801 (2005).
277. J. Dunningham and T. Kim, "Using quantum interferometers to make measurements at the Heisenberg limit," *J. Mod. Opt.* **53**, 557 (2006).
278. P. Gupta *et al.*, "Optimized phase sensing in a truncated SU(1,1) interferometer," *Opt. Express* **26**, 391 (2018).
279. D. Rugar *et al.*, "Single spin detection by magnetic resonance force microscopy," *Nature* **430**, 329 (2004).
280. J. Arlett, E. Myers, and M. Roukes, "Comparative advantages of mechanical biosensors," *Nat. Nanotechnol.* **6**, 203 (2011).
281. C. LeMieux *et al.*, "Polymeric nanolayers as actuators for ultrasensitive thermal bimorphs," *Nano Lett.* **6**, 730 (2006).
282. U. B. Hoff *et al.*, "Quantum-enhanced micromechanical displacement sensitivity," *Opt. Lett.* **38**, 1413 (2013).
283. C. A. Putman *et al.*, "A detailed analysis of the optical beam deflection technique for use in atomic force microscopy," *Appl. Phys.* **72**, 6 (1992).
284. D. Smith, "Limits of force microscopy," *Rev. Sci. Instrum.* **66**, 3191 (1995).
285. S. Kawata, Y. Inouye, and P. Verma, "Plasmonics for near-field nano-imaging and superlensing," *Nat. Photon.* **3**, 388 (2009).
286. E. Ozbay, "Plasmonics: merging photonics and electronics at nanoscale dimensions," *Science* **311**, 189 (2006).
287. T. Ebbesen *et al.*, "Extraordinary optical transmission through sub-wavelength hole arrays," *Nature* **391**, 667 (1998).
288. A.V. Zayats and I. I. Smolyaninov, "Near-field photonics: surface plasmon polaritons and localized surface plasmons," *J. Opt. A* **5**, S16 (2003).
289. C. Lee *et al.*, "Quantum plasmonics with a metal nanoparticle array," *Phys. Rev. A* **85**, 063823 (2012).
290. D. Ballester *et al.*, "Long-range surface-plasmon-polariton excitation at the quantum level," *Phys. Rev. A* **79**, 053845 (2009).
291. E. Altewischer, M. van Exter, and J. Woerdman, "Plasmon-assisted transmission of entangled photons," *Nature* **418**, 304 (2002).
292. G.-Y. Chen *et al.*, "Surface plasmons in a metal nanowire coupled to colloidal quantum dots: scattering properties and quantum entanglement," *Phys. Rev. B* **84**, 045310 (2011).
293. A. Huck *et al.*, "Demonstration of quadrature-squeezed surface plasmons in a gold waveguide," *Phys. Rev. Lett.* **102**, 246802 (2009).
294. Z. Jacob and V. Shalaev, "Plasmonics goes quantum," *Science* **334**, 463 (2011).
295. D. Wang *et al.*, "Feedback-optimized extraordinary optical transmission of continuous-variable entangled states," *Phys. Rev. B* **91**, 121406 (2015).
296. R. Nichols *et al.*, "Multiparameter Gaussian quantum metrology," *Phys. Rev. A* **98**, 012114 (2018).
297. L. Bao *et al.*, "Multi-channel quantum parameter estimation," *Sci. China Inf. Sci.* **65**, 200505 (2022).